

Exploring New Techniques for Superconducting Kinetic Inductance Parametric Amplifiers

A
Dissertation
Presented to
the faculty of the School of Engineering and Applied Science
University of Virginia

in partial fulfillment
of the requirements for the degree

Doctor of Philosophy

by

Scott Hinton

May 2024

APPROVAL SHEET

This
Dissertation
is submitted in partial fulfillment of the requirements
for the degree of
Doctor of Philosophy

Author: Scott Hinton

This Dissertation has been read and approved by the examining committee:

Advisor: Robert M. Weikle II

Advisor: Arthur W. Lichtenberger

Committee Member: Harry C. Powell Jr.

Committee Member: Michael Cyberey

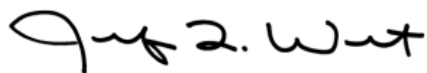
Committee Member: Bradley Johnson

Committee Member: N. Scott Barker

Committee Member:

Committee Member:

Accepted for the School of Engineering and Applied Science:



Jennifer L. West, School of Engineering and Applied Science

May 2024

Abstract

Superconducting parametric amplifiers are able to amplify a signal with zero added noise in theory. They are created from transmission lines with nonlinear properties or elements. But this relatively new area of research still has many opportunities for exploring new avenues. While CPW (Co-Planar Waveguide) is still the most common transmission medium chosen due to its simplicity of fabrication, using a microstrip medium would allow for more flexibility, complexity, and performance in designing these amplifier circuits. Some groups use microstrip circuits already, but with an amorphous dielectric which will contribute more noise, so a fabrication method for using SOI (Silicon On Insulator) is presented. In order to reduce the long transmission line lengths required for sufficient gain and to provide an alternative for creating bandgaps, a model for loading the amplifying transmission line with capacitive stubs is discussed. Since placing these stubs in close proximity causes them to electromagnetically couple, a technique for simplifying the modeling of an arbitrarily long periodic coupled structure is offered. Given that current superconductors require a cryogenic system, the complexity of designing and measuring in these conditions are described. In order to test high frequency devices at cryogenic temperatures, a w-band four-wave mixing parametric amplifier test system in a milliKelvin dilution refrigerator has been prepared.

Contents

Abstract.....	3
Acknowledgements.....	6
Introduction	7
Motivation and context	7
Contributions	8
Chapter 1: Background, Theory, and State-of-the-Art of TKIPs.....	9
Traveling-Wave	9
Kinetic Inductance.....	10
Dispersion Engineering	12
Parametric Amplifier	16
Four Wave Mixing	17
Three Wave Mixing	18
Mathematical Description	20
Challenges of the state-of-the-art	26
Chapter 2: SOI Microstrip	27
Motivation.....	27
Fabrication Process	27
Fabrication Results.....	37
Chapter 3: Circuit Modeling.....	43
Motivation behind the device structure	43
Transmission line theory.....	44
Inaccuracy of the lumped element model.....	45
Model used for the stub-loaded line	46
Stub Coupling.....	48
Coupled line theory.....	48
How to model coupling in an electromagnetic simulator	49
How to model coupling in a circuit model	50
Proposed Designs.....	65
Design 1: A stub-loaded line without coupling	65
Design 2: A line without stubs	66
Chapter 4: Cryogenic Systems	69

Thermal Considerations	69
Noise Considerations	69
Noise in cryogenic systems	71
Measuring Noise	72
Measurement System Development	77
UVA Cryostat	77
BlueFors Millikelvin Dilution Refrigerator	78
Thermal Considerations	79
Noise Measurement.....	80
Chapter 5: Future work.....	83
Bibliography	84

Acknowledgements

Before approaching the end of this journey, one does not fully appreciate the extent to which they depend on the assistance and goodwill of others in order to progress. I feel blessed to have been surrounded by helpful, talented and caring individuals that made this endeavor possible. My advisors, Bobby and Art, have given countless hours guiding and refining my work. To Patricio Mena, Omid Noroozian, and Peter Day who generously shared expertise in the field. I am grateful to the National Radio Astronomy Observatory for their generous support of my research through the Grote Reber doctoral fellowship. I am forever in the debt of Mike Cyberey who was my day-to-day mentor in the cleanroom and enabled every inch of superconductor work that I realized. Dustin, Theo, and Alec were my companions through long hours in the lab. And to Chris Moore whose enduring, potent friendship and tenacious expertise imparted impetus and perspective in all the ups and downs of the path. And of course to my family, without whom I would be nothing.

Introduction

Motivation and context

This document describes an exotic and relatively new type of LNA (Low Noise Amplifier) called a TKIP (Traveling-wave Kinetic Inductance Parametric amplifier). There are many, many types of RF (Radio Frequency) amplifiers in existence; therefore some rationale is appropriate before adding one more acronym to the amplifier alphabet soup. There are two principal use cases in which even the lowest-noise LNAs are still too noisy: radio astronomy and quantum computing. There are other amplifiers which provide greater gain, wider bandwidth, and a superior dynamic range than those of current TKIPs while still contributing relatively “low” levels of noise. But when one seeks to hold many entangled qubits in coherence or observe electromagnetic radiation from millions of light years away, the amplifier’s noise is what sets the upper limit on the performance of today’s systems. This is the motivation behind TKIP development efforts.

The remainder of this section will provide a detailed and quantitative argument for the utility of TKIPs from the perspective of radio astronomy exclusively while neglecting a similar exposition from the perspective of quantum computing. This bias comes from the author being more familiar with the interests and needs of the radio astronomy community due to relationships with and support from the National Radio Astronomy Observatory staff.

98% of photons emitted since the Big Bang possess energy corresponding to the far-infrared (FIR) and submillimeter (subMM) wavelengths [6]. This wealth of physical information is crucial to our understanding of the formation and evolution of stars, galaxies, and the entire universe [7]—and it falls within the domain of radio astronomy. These are frequencies that we still struggle to observe efficiently [6]. Astronomers desire wide bandwidths to be able to detect many spectral lines simultaneously instead of having to perform multiple measurements in a sweep. However as more spectrum is accepted more noise is introduced as well. More noise reduces our power to observe—less power means a radio telescope must stay focused on its target longer for an observation (and with many institutions competing to use a very limited number of telescopes, observation time is valuable). The most critical component in determining the sensitivity of a system is the Low-Noise Amplifier (LNA), as it is placed early in the system cascade where the signal is the weakest. It is necessary to amplify the faint signal while adding the least amount of noise possible in order to set a high Signal-to-Noise Ratio (SNR). The SNR at the LNA output will not improve in the remaining components of the system cascade since any subsequent amplification will also amplify the noise already included with the signal, while adding even more noise. The LNA noise contribution is the limiting factor in the bandwidth of current radio astronomy receivers [8]. The additional noise introduced by an increased bandwidth makes it more efficient to perform multiple band-limited observations. Thus reducing the noise of the LNA is a major goal in enabling the research of this field.

The uncertainty associated with quantum mechanics adds a minimum noise to all RF devices equivalent to the energy of one half of a photon ($hf/2$), where h is Planck’s constant. Current state-of-the-art LNAs use InP-based High-Electron-Mobility Transistors (HEMTs) which offer high gain (25-40 dB) and bandwidth (an octave or more) and are conveniently available commercially [9]; however they also exhibit a noise temperature of 4-5K at 10GHz which is more than 15 times the minimum noise limit dictated by quantum mechanics [8, 10-13]. The fundamental minimum noise temperature of these

devices is expected to be eight times the quantum limit [8]. Another alternative is to use a parametric amplifier based on superconducting Josephson Junctions. These can provide good gain (20-30 dB) with quantum-limited noise performance and can be designed for traveling-waves to avoid the narrow bandwidths of resonant devices, allowing for an octave of bandwidth. However their dynamic range is much poorer, typically around -100dBm [3, 14] (-1dB saturation at -98dBm [13]). Due to the shortcomings of these technologies, a new type of amplifier—superconducting parametric amplifiers based on the intrinsic kinetic inductance of superconductors—is gaining attention in the fields of astronomy and quantum computing. It is known by a variety of acronyms depending on the research group (e.g. KIT, DTWKI, DKITWPA), the author’s group has adopted the title “TKIPs”: Traveling-wave Kinetic Inductance Parametric amplifiers. They offer good gain, wide bandwidth (often an octave or more [15]), high dynamic range (~-50dBm [16], comparable to microwave transistor amplifiers [2]), and theoretically zero added noise. The measured noise of devices to date is typically within a factor of 2 of the quantum limit [3, 17-19].

The potential impact of these devices is such that the Atacama Large Millimeter Array (ALMA), the largest radio telescope in the world, mentions this technology by name in its 2030 roadmap recommending that:

Long-term sustained research in better devices or new technologies (such as TKIP amplifiers) has the potential to yield significant breakthroughs that are equivalent to doubling or tripling the collecting area of the array with its present instrumentation. [20]

For example, in the application of radio astronomy, TKIPs can potentially improve the noise performance of Atacama Large Millimeter Array (ALMA) receivers by a factor of ~5 and improve the bandwidth by a factor of 2.5, resulting in 10 times greater observation efficiency (speed) [16]. However both the design and measurement of these devices are challenging and due to their novelty, sensitivity, and exotic materials. Given that the field is still in its infancy, new techniques need to be explored in their fabrication and circuit architecture to optimize performance. That is the mission of the present work.

Contributions

My work has extended the current body of superconducting parametric amplifier knowledge in four specific ways. First, it offers a novel fabrication recipe to produce superconducting microstrip circuits using thin crystalline SOI (Silicon On Insulator) as a dielectric. Second, it explains a new approach to designing TKIPs using periodic stubs with sinusoidal length variation, including a circuit model and comparisons with the traditional line using stepped impedances for dispersion engineering. Third, it presents a simplification technique for modeling coupling in arbitrarily long periodic structures. Fourth, it has extended the current capabilities of microwave cryogenic metrology with a w-band parametric amplifier test system in a milliKelvin dilution refrigerator.

Chapter 1: Background, Theory, and State-of-the-Art of TKIPs

The title “TKIP” is a very concise expression of the techniques and physics utilized in this technology. Each term holds significance and will be considered serially here.

Traveling-Wave

Traveling-wave refers to the fact that TKIPs do not utilize resonant structures, which are naturally narrowband. Instead a TKIP has, in a sense, “unrolled” that resonant path into a transmission line which inherently has much larger bandwidth. This does result in longer circuits which occupy more space; examples are shown in Figure 1 below.

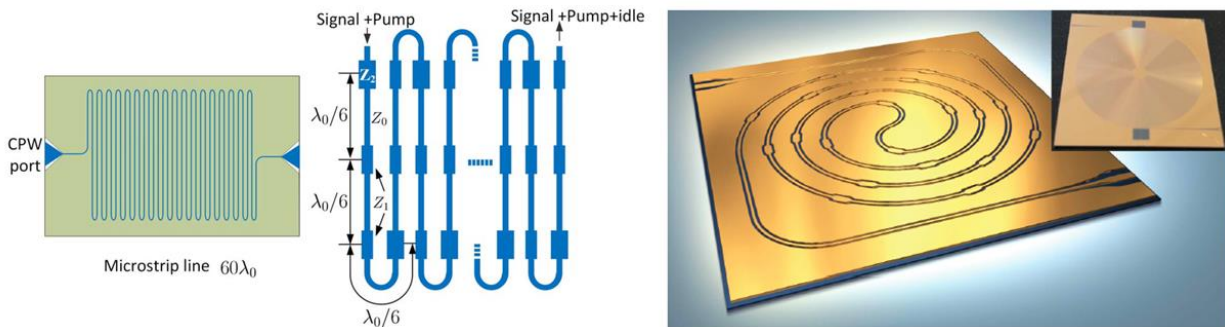


Figure 1: stylized illustrations of long TKIPs. Left: a meandered TKIP from [1], Right: a double-spiral TKIP where a 2.2-meter transmission line is coiled into a 2cm by 2cm area from [3]. Both have tapered impedance transformers at each end.

This high demand of wafer real-estate can be ameliorated by using slow-wave structures as demonstrated in Figure 2. This reduces the phase velocity of a propagating wave, slowing down the signal and causing it to spend more time in the amplifying medium and thus achieving greater gain with shorter transmission lines. For example, [13] achieved 15dB of gain using a transmission line of 2.2 meters while [4] also reached 15dB using a slow-wave line of 0.1 meters. Also since the line is shorter the fabrication yield is greater—a slow-wave structure with its capacitive loading may occupy more wafer area overall, but a defect affecting a capacitive finger is merely a nuisance, whereas a defect along the central propagation path would result in catastrophic device failure.

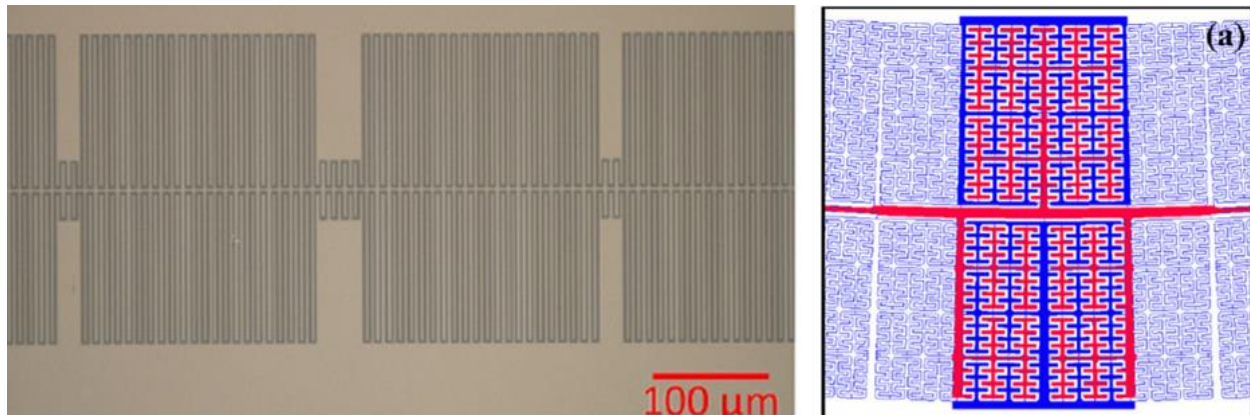


Figure 2: Examples of slow-wave TKIPs. Left: a narrow CPW line with long capacitive fingers and periodic impedance steps for dispersion engineering, copied from [4]. The dark areas are the CPW gaps. Right: A slow-wave structure using quasi-fractal capacitive fingers, copied from [5]. The red is the CPW line and the blue is the CPW ground.

Kinetic Inductance

It is well-known that electrons have mass, and when an electrical current is induced they also have a velocity. However the effects of the electron's momentum are generally ignored. This is warranted since said effects are so small as to be negligible relative to other phenomena, such as electrical resistance. However when the electrical resistance disappears, as is the case in superconductors, new properties become dominant and useful. This claim can be substantiated as follows. With reference to the Drude model, the resistance of a wire is found to be

$$R = \left[\left(\frac{m}{nq^2} \right) \left(\frac{\ell}{A} \right) \right] \left(\frac{1}{\tau} \right) \quad (1)$$

where m is the electron effective mass, n is the density of electrons, q is the electron charge, ℓ is the length of the wire, A is the wire cross section, and τ is the mean time between scattering events. Now consider the kinetic reactance of the same wire:

$$\omega L_k = \left[\left(\frac{m}{nq^2} \right) \left(\frac{\ell}{A} \right) \right] \omega. \quad (2)$$

One can immediately recognize the similarity between these two equations and observe that when $\omega > 1/\tau$ the kinetic reactance will dominate the resistance. In typical metals at room temperature this frequency might be 10^{18} Hz [21], surpassing the material's plasma frequency. However, in superconductors, the DC resistance is zero and the contribution of the electron momentum to the circuit inductance (kinetic inductance L_k) must be more closely considered. And just as the equation for kinetic energy is nonlinear with velocity, the additional circuitual inductance is quadratically proportional to the electrical current (velocity of the electrons), as detailed in [22]:

$$L_k(I) = L_o \left(1 + \frac{I^2}{I_*^2} + \dots \right). \quad (3)$$

where I_* sets the scale of the nonlinearity (discussed shortly), and

$$L_o \approx \frac{\hbar \rho}{\pi \Delta_o t} \quad (4)$$

where ρ is the film resistivity (in its normal, non-superconducting state), t is the film thickness, and Δ_o is the BCS superconducting energy gap at zero Kelvin [23]

$$\Delta_o = 1.764 * k_B * T_c \quad (5)$$

where k_B is Boltzmann's constant and T_c is the superconducting critical (or transition) temperature. Alternatively, if the current is assumed to be uniformly distributed across the conductor cross section then the kinetic energy per unit length can be calculated [24] as

$$L_k = \frac{\mu_o \lambda_L^2}{wt}. \quad (6)$$

and I_* can be estimated [24] by

$$I_* = \frac{wt \kappa_* \Delta}{\lambda_L} \sqrt{\frac{N_o}{\mu_o}} \quad (7)$$

where w is the conductor width, t is the conductor thickness, λ_L is the London penetration depth, N_o is the density of states at the Fermi level, and κ_* is a fitting parameter estimated to be 1.37. Therefore the total inductance of a superconducting transmission line can be expressed as the sum of the magnetic and kinetic inductance contributions, i.e.

$$L_{tot}(I) = L_m + L_k(I) \quad (8)$$

The total gain a device is capable of providing is proportional to the scale of this L_k nonlinearity. As the temperature is reduced below the critical temperature of the superconducting material (T_c), more Cooper Pairs are formed, producing a temperature dependence of the energy gap [25] as seen in Figure 3. Since the gap is created by vacancies of electrons which have formed Cooper Pairs, the size of the gap provides an indication of the number of Cooper Pairs in existence.

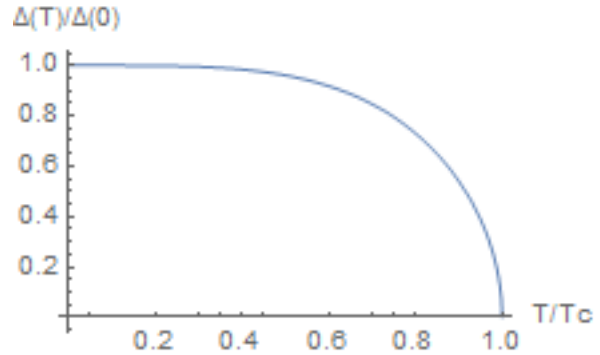


Figure 3: temperature dependence of the superconducting energy gap.

To maximize the gain produced by a TKIP device there are several aspects of the superconducting film properties that should be considered. Several are evident from examining (4) and are straightforward, such as film thickness. Others are functions of the deposition conditions, such as the ratios of atoms in an alloy (e.g. $Nb_xTi_yN_z$). One should adjust these deposition conditions (gas partial pressures, material sputter rate, etc.) to provide a maximum normal resistivity ρ , T_c , I_c (H_c), and Δ_0 . Increasing the critical current of the material would permit the device to be pumped more strongly, increasing the nonlinearity of the device in quadratic fashion. As discussed above, as T is lowered below T_c more Cooper Pairs are formed and thus a greater I_c can be achieved. Therefore given a certain operating temperature and superconducting material (e.g. Nb at 4K), if one can change the material preparation in such a way as to increase the T_c then more Cooper Pairs will exist at the designated operating temperature providing greater critical current. However this is not strictly true when comparing different materials, as one must also take into account the number of valence electrons. Another factor to consider is increasing the superconducting energy gap Δ . While this would reduce L_0 according to (4), it also has two important benefits. First, it increases the number of Cooper Pairs formed with the aforementioned benefits. Secondly it increases the maximum frequency at which a device can operate without significant noise. The energy gap of 2Δ dictates the minimum frequency at which the photons contain enough energy to break a Cooper Pair and excite two quasiparticles—which adds loss and noise to the device’s performance.

Among the superconducting materials compatible with current fabrication processes, Niobium Titanium Nitride (NbTiN) has the highest normal resistivity, highest critical temperature, and also has a high energy bandgap (2.89meV), allowing it to function up to a frequency of 1.4 THz [24], opening the door to the millimeter-wave regime. In comparison, Niobium can operate optimally up to ~ 737 GHz (1.525meV) while Aluminum only reaches ~ 82 GHz (0.17meV) [26]. Also NbTiN can be grown at room temperature, which simplifies the fabrication recipe and equipment requirements.

Some groups ([27-30] are some examples) have investigated traveling-wave parametric amplifiers using the inductance of Josephson Junctions (A.K.A. Superconductor-Insulator-Superconductor or SIS junctions), which have a much larger nonlinearity (9) [30]

$$L_j(I) = \frac{\hbar}{2qI_c} \frac{\sin^{-1}(I/I_c)}{I/I_c}. \quad (9)$$

However the very small cross sections of typical Josephson Junctions lead to a very high current density, which translates to low saturation and dynamic range [15] (-1dB saturation at -98dBm [13]); such structures are also more complicated to fabricate. Thus while the material’s native kinetic inductance offers a weaker nonlinearity it has the potential to be a more effective amplifier.

Dispersion Engineering

While “dispersion engineering” is not explicitly mentioned in the title “TKIP”, it is a feature of fundamental importance for TKIPs, and thus will be mentioned here (and the titles that some other groups use, e.g. DTWIPA, do include the term).

Dispersion refers to the physical phenomenon in which different frequencies propagate with different phase velocities in certain media. This is a major issue in TKIPs because the small-signal amplification depends on the relative phase of the pump and the signal. Therefore dispersion poses a limitation on the device bandwidth [18, 31] if the pump and the signal travel at different velocities. Furthermore, the inherent nonlinearity of the superconductor (the Kinetic Inductance) affects the phase velocity. The phase velocity of a transmission line is expressed as

$$v_p = \frac{1}{\sqrt{LC}} \quad (10)$$

where L and C are the distributed inductance and capacitance, respectively, of the transmission line. As already discussed, a current in a superconductor will induce kinetic inductance (3), which means that a strong pump can generate appreciable dispersion in the line. One approach to compensate for this effect is to design corrective dispersion into the device that will slow the pump wave and propagate in phase with the signal. This dispersion engineering typically takes the form of a periodic structure that has frequency stopbands and passbands around which the propagation constant and phase velocity are altered [32]. Stopbands are sections (bands) of the frequency spectrum which are significantly attenuated or blocked entirely in a network, and passbands are portions of the frequency spectrum which experience little to no attenuation in a network. This phenomenon can be observed in Figure 4, which has engineered

loadings to create minor dispersion with a corresponding shallow stopband at 10.5 GHz, significant dispersion with a more severe stopband at 21 GHz, and major dispersion with a dramatic stopband at 30 GHz. Delta beta refers to the difference between the phase constant of the loaded line to that of an unloaded line. Such

periodic structures are often

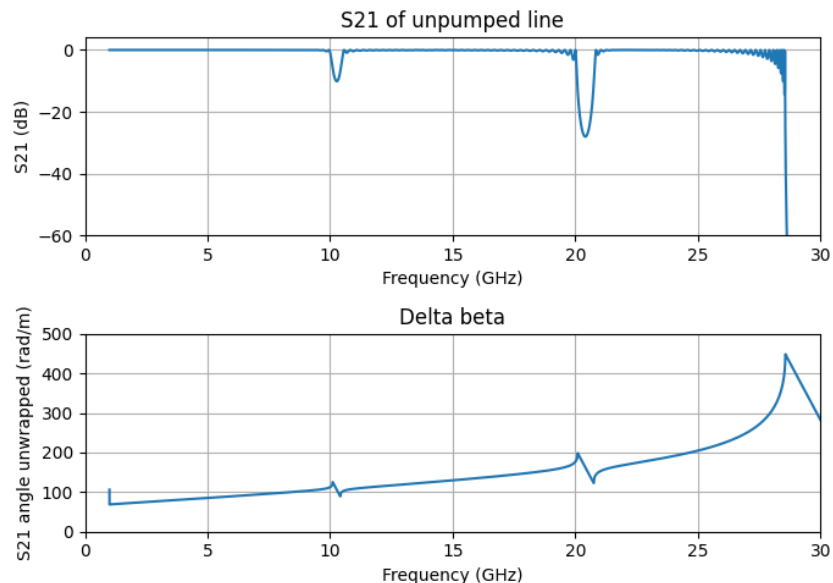


Figure 4: An example of how dispersion engineering can perturb the beta of a transmission line (Delta beta), and the resulting stopbands.

studied in solid state device or crystal applications and are described using Brillouin zones, Floquet-Bloch modes, and k - β diagrams. In practice this dispersion engineering is usually achieved by periodically altering the impedance of the transmission line, as shown in Figure 5.

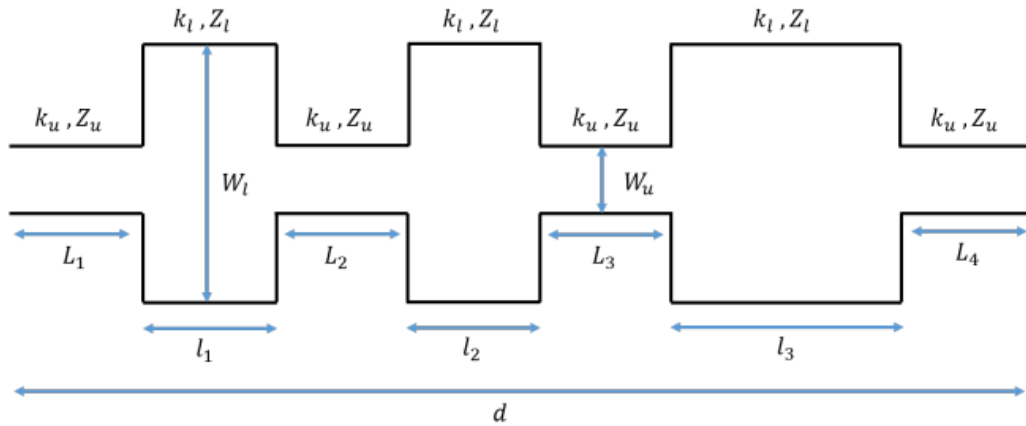


Figure 5: Traditional approach to dispersion engineering.

This feature can be seen in the pictures/illustrations of TKIPs above (Figure 1 and Figure 2). In contrast to those designs with abrupt impedance steps, my approach is to attempt to vary the impedance smoothly over a periodic unit. Furthermore, I employ slow-wave lines as explored in previous work shown in Figure 2, with the benefits mentioned in that same section. This is done by “loading” the line with stubs to adjust the distributed line capacitance. The length of the capacitive stubs will be varied as shown in Figure 6 to create a stopband in the center of the desired operating range. At the edge of the stopband there is a divergence from the natural dispersion of the line in order to compensate for the phase slippage between the pump and signal as visible in Figure 7 and Figure 8. The design of the dispersion engineering is straightforward: a periodic structure will create a stopband at the frequency whose half wavelength matches the periodicity of the structure. Or expressed mathematically,

$$f_{stop} = \frac{v_p}{2l_{period}}. \quad (11)$$

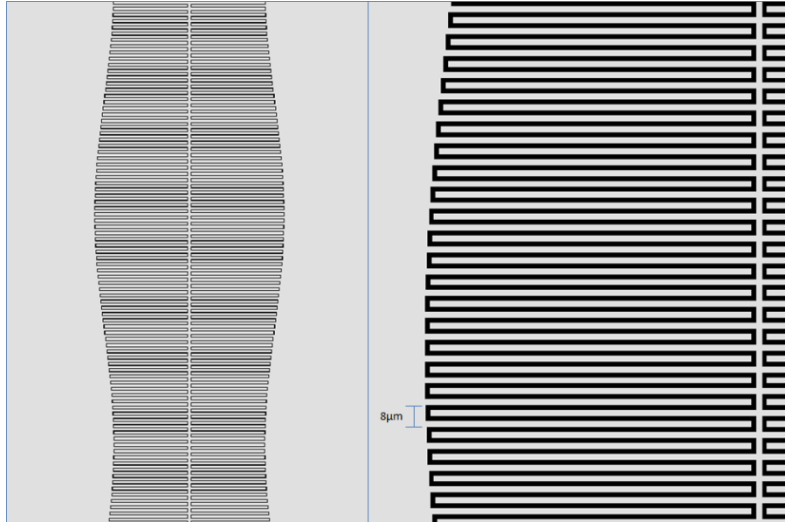


Figure 6: CAD of the mask of a TKIP. Left: a longer portion of the slow-wave transmission line showing the periodic variation in the stub/finger lengths. The apparent variation in the CPW gap around the stubs is merely an artifact, aliasing of the rendering in the CAD software. Right: a closer image showing more details of a unit cell.

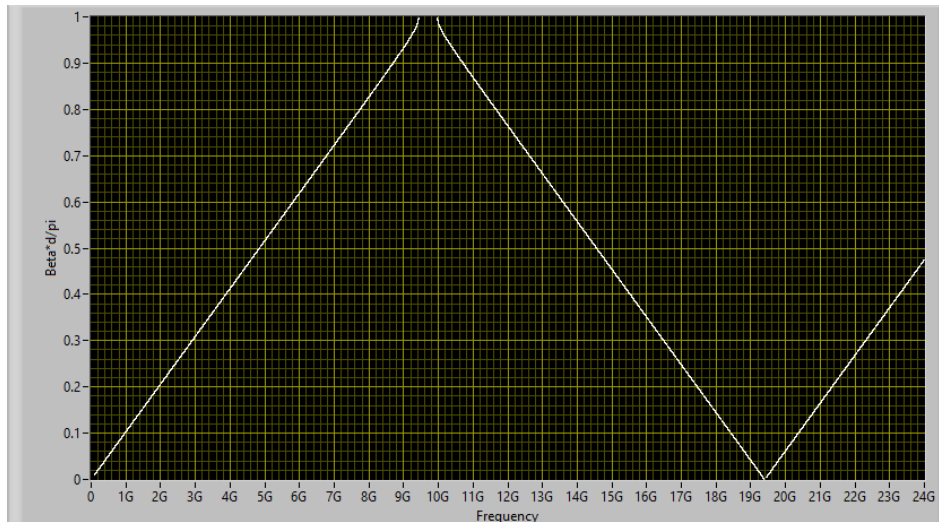


Figure 7: Example graph showing the dispersion created by periodic loading of the transmission line. This line's dispersion was engineered to operate the pump at 9.4 GHz, at the edge of the stopband, where the propagation constant is altered. When the pump is located at the edge of the stopband this alteration compensates for the natural dispersion in the line, allowing the pump and signal to propagate in-phase over a wider bandwidth. A $k-\beta$ version, favored by some other fields of study, is shown in Figure 20; however Beta vs. frequency is more intuitive for the microwave engineer.

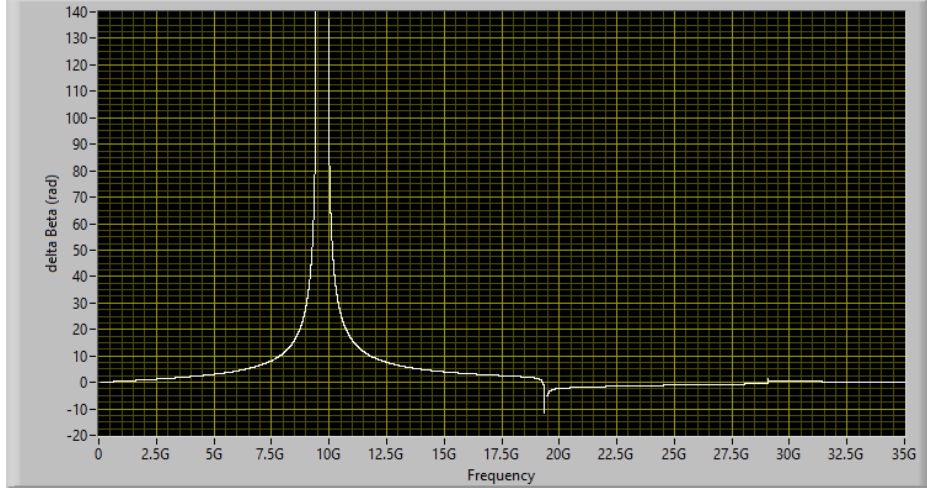


Figure 8: The difference in propagation constant Beta caused by the periodic loading vs. the unloaded transmission line.

Additionally, dispersion engineering can be used to block undesired harmonics. The kinetic inductance of a superconductor presents a third-order nonlinearity. While the kinetic inductance (3) is indeed quadratically related to the current, power is a function of voltage and current, not inductance. The voltage of an inductor is described as

$$V_L = L \frac{dI}{dt} \quad (12)$$

and when the nonlinear inductance of the superconductor (3) is substituted, the squared current term of L_{KI} and the time derivative of the current form a third-order relationship:

$$V_L = \left[L_o \left(1 + \frac{I^2}{I_*^2} \right) \right] \frac{dI}{dt} \quad (13)$$

This third-order nonlinearity enables a phenomenon known as Four-Wave Mixing (4WM), which will be described in more depth in the next section. It is sufficient to note for this discussion of harmonics that 4WM involves combinations of four photons, including the case of three pump photons being annihilated to generate one photon at the third harmonic. Furthermore, when operated in Three-Wave Mixing mode (also discussed in the next section) the second harmonic of the pump can also be produced.

Harmonics are always undesirable in LNAs; however they are even more detrimental in the case of a superconductor. If the harmonics are able to propagate without sufficient attenuation they would continue to be amplified and in turn produce higher and higher harmonics and ultimately result in a shock wave [33]. This phenomenon would exceed the current capacity of the superconductor and break its superconducting state, returning it to a normal state with resistance and loss. Note how typical designs have more than one stopband--the periodicity of the impedance steps is also periodic (every third loading is slightly perturbed) to create a stopband around $3f_p$ to block the third harmonic (for use with 4WM). Note that while the harmonics are usually blocked by the dispersion engineering, it is also possible to attenuate it in other ways, e.g. capacitive fingers which act as quarter-wavelength stubs at a harmonic frequency.

Parametric Amplifier

A parametric amplifier is a device which amplifies a signal by variation of a circuit reactance in time. When the parameter being varied is a pure reactance then the amplification occurs with no noise added. This principle is not new; it found widespread interest the 1950's using the nonlinear capacitance of varactor diodes and promised low noise operation. However its implementations often suffered from instabilities (oscillations) and ultimately were abandoned in favor of transistor technologies in the 1960's. Nevertheless, the need for lower-noise amplifiers for quantum computing and radio astronomy, coupled with the discovery of parametric amplification in a superconducting transmission line 10 years ago, have revived interest in this concept.

As mentioned previously, the inductance of a superconductive material varies with current, where this nonlinearity may be used for mixing and amplification. Energy can be transferred from a signal at one frequency to a signal at a different frequency via the phenomenon of Three-Wave or Four-Wave Mixing (3WM and 4WM, respectively)¹. These concepts will be described shortly. Usually one of those "signals" is a strong CW (Continuous Waveform) tone called a pump whose purpose is to provide the energy for amplification. It can be considered as an "AC bias" as it serves a similar role to the DC bias that conventional transistor amplifiers use. Thus by pumping the transmission line with a strong pump tone, power can be transferred to the signal.

It should be reiterated that the pump and signal must be synchronized in phase for optimal mixing and gain to occur—otherwise the phase-matching constraints of the conservation of momentum dictate that this process's efficiency will be diminished to zero gain at 90 degrees out of phase, or energy will flow to the pump at the expense of the signal if they are in anti-phase.

While there are many combinations of frequencies that can satisfy the conservation of energy and momentum, only two—shown boxed in Figure 9—can provide broadband signal gain[2]. Therefore, we restrict our interest and discussion to those cases. However, while the other mixing processes are not optimal designs, they will still cause mixing to occur when the laws of conservation are satisfied, and must be accounted

for in simulations in order to avoid unexpected behavior. This will perturb the expected gain profile and also manifest itself as added noise [14]

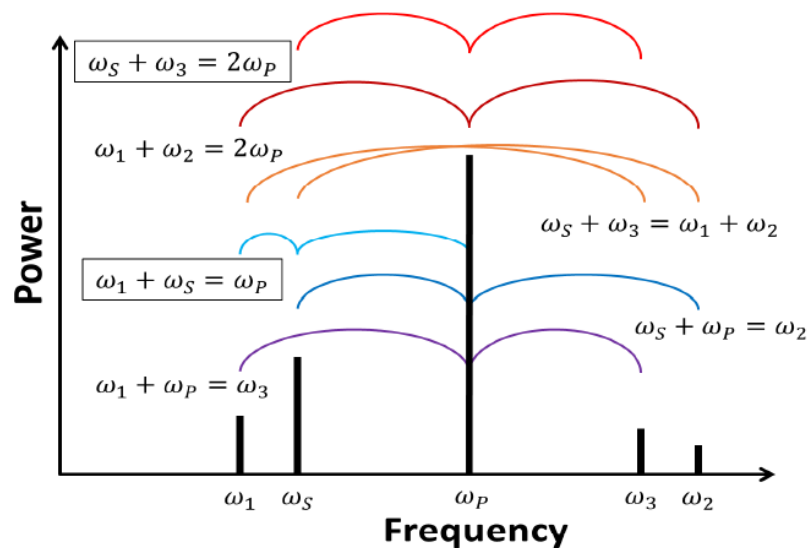


Figure 9: Possible permutations of mixing frequencies within a TKIP. Only the equations enclosed in boxes can provide broadband gain and thus are of interest. Copied from [2].

¹ These concepts are normally studied in courses on nonlinear optics, and indeed the same coupled-mode equations are often used to model TKIPs.

Four Wave Mixing

4WM involves combinations of four photons via a third-order nonlinearity. The photons can be in any arrangement which satisfies the constraints of energy and momentum conservation, e.g. one input photon could be annihilated and three output photons could be created. In the present application we will restrict our attention to the arrangement of two input photons and two output photons. When the two input photons are of the same frequency it is referred to as “degenerate” 4WM, which is our case of interest. The two input photons are supplied by the pump tone. One of the output photons is the signal, and the other is called the “idler” which balances the laws of conservation. The energy and momentum of the output photons sum to equal the energy and momentum of the input photons, as shown in Figure 10 for the general case. This is the common mode of 4WM operation of TKIPs. A key detail is

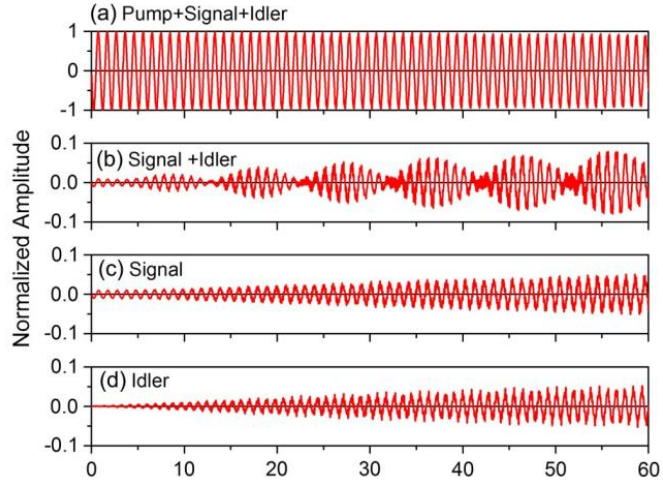


Figure 11: Growth of the signal and idler as they co-propagate down the line. Copied from [1].

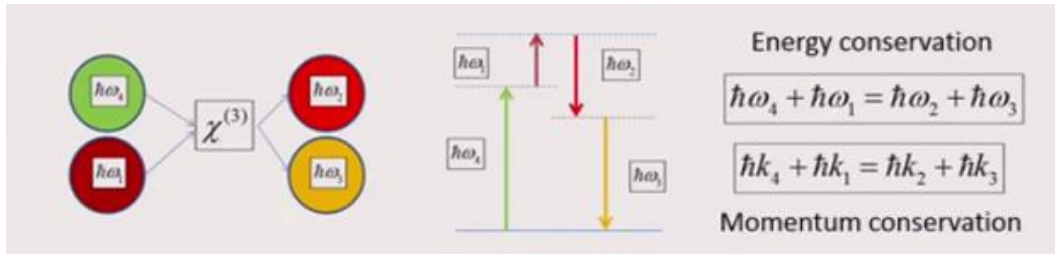


Figure 10: Cartoon depiction of the 2-to-2 Four Wave Mixing process, and its energy and momentum conservation constraints where $\hbar\omega_1$ and $\hbar\omega_4$ are the input pump photons, $\hbar\omega_2$ is the signal photon and $\hbar\omega_3$ is the idler photon.

that these nonlinear processes are not entirely spontaneous in that two pump photons will not be constantly converted into any and all possible output frequencies. The creation of a signal photon from the 4WM process comes as a response to the stimulus of the other three photons (two pump and one idler), and the creation of an idler photon results from the interaction of a signal and two pump photons. Thus only one of the output photons in the nonlinear process can be spontaneously produced. In the case at hand the idler is created (which in turn enables the production of more signal photons) but not without first applying a signal to the system. This dependence is clear upon examination of the mathematics describing the processes as detailed below, particularly equation (25). The change (derivative) of the amplitude of any of the frequencies in the process is dependent on the amplitudes of all the other frequencies in the process. A further demonstration of this principle can be observed in the simulation of the co-amplification of the signal and idler copied in Figure 11. Close examination of the data shows that the signal does not begin to gain power until the idler wave reaches nearly the same amplitude as the signal. It should be clear then that the idler product of the mixing process is not equivalent to the sideband output of a traditional microwave mixer, as the traditional mixer’s conversion matrix has no dependence upon the amplitude of the signal at the image frequency.

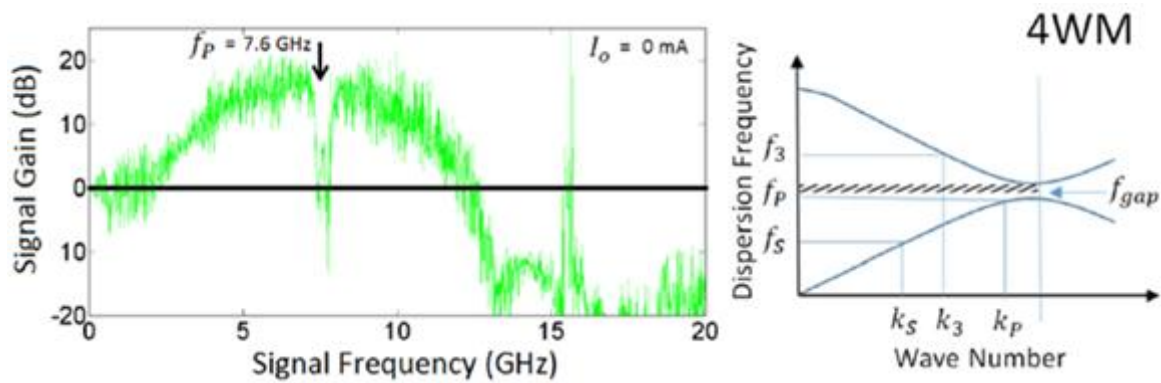


Figure 13: The gain profile and dispersion graph of an actual TKIP operating in 4WM mode. Copied from [3]. k_3 on the image to the right refers to the wavenumber of the idler.

Since the pump must operate at the edge of a stopband to achieve phase matching conditions (see the Dispersion Engineering section), this will cause said stopband to fall in the middle of the gain profile and create a notch (see Figure 13). This is an unfortunate side effect of using 4WM. One will note that if the two input photons are at the same frequency (as is the case in degenerate 4WM), then of two output photons (signal and idler), one must be at a frequency higher than the input and the other at a lower frequency, as demonstrated in Figure 12. This causes the photons to fall into different passbands, which are not perfectly symmetric. Because of this, it is impossible to obtain robust phase

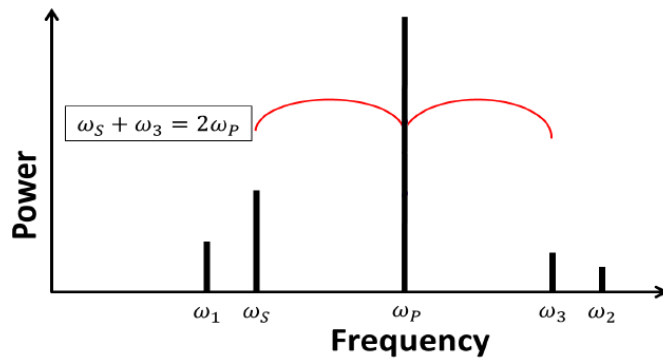


Figure 12: Frequency spectrum created by degenerate Four Wave Mixing. In this diagram ω_3 refers to the idler frequency.

matching, resulting in intrinsic variations (ripples) in the gain profile (which is in addition to any standing waves caused by impedance mismatch reflections) [2]. Aside from that, however, when the phase matching conditions are met, an amplifier operating in 4WM mode can produce exponential gain while in the amplifying medium with no

limitations on total amplifier line length.

This is not the case with 3WM as will soon be shown.

4WM has traditionally been the more popular form of parametric amplification because it simplifies the circuit and test hardware (requiring no ultra-low noise DC source and no bias tees, etc.), and provides for larger gain.

Three Wave Mixing

Much of the discussion of 4WM also applies here, with a few notable differences. 3WM involves combinations of three photons (one pump, one signal, and one idler photon) via a second-order nonlinearity. This nonlinearity, in the case of TKIPs, is manifested with the application of a DC bias. As with 4WM, when the laws of conservation are met, the supplied pump photon may spontaneously split into two photons.

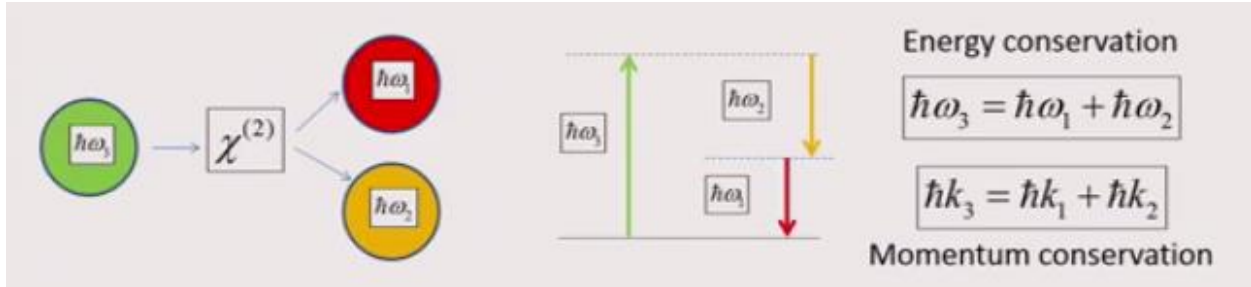


Figure 14: Cartoon depiction of the 1-to-2 Three Wave Mixing process, and its energy and momentum conservation constraints

The frequency spectrum resulting from 3WM is different from that of 4WM in a significant way. While in 4WM the pump frequency lies in between the signal and idler (i.e. the center of the device bandwidth), in 3WM the pump is well separated from the signal and idler frequencies. This has two important consequences. First, the pump can

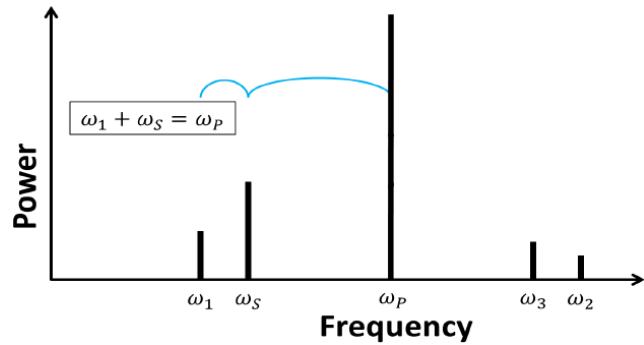


Figure 15: The frequency spectrum resulting from Three Wave Mixing. ω_1 refers to the idler frequency.

be filtered out more easily in 3WM because it is far detuned from the signal frequencies.

Secondly, it means that the stopband does not

need to fall in the middle of the gain profile, avoiding an inconvenient notch. Also, since the signal and the idler will exist within the same passband, their phases can be well-matched over a large bandwidth.

This is diagrammed in the right half of Figure 16 below and, in theory, results in fewer gain ripples [2].

3WM also requires an order of magnitude less RF input power [2] to provide signal gain (requiring only one pump photon instead of two), but with a lower maximum gain than 4WM. 3WM also has

limitations on the maximum input power as well as a maximum device length [2]. These limits arise because with greater input power or a longer device length the gain of the 4WM process can approach or dominate the 3WM gain, thus disrupting the expected operation of the device.

The requirement of less pump power is a significant advantage because many of the challenges that currently hinder TKIP performance are caused or exacerbated by high pump power heating the chip (e.g. reduced gain, gain ripples, and added noise).

These challenges will be explained in more detail later.

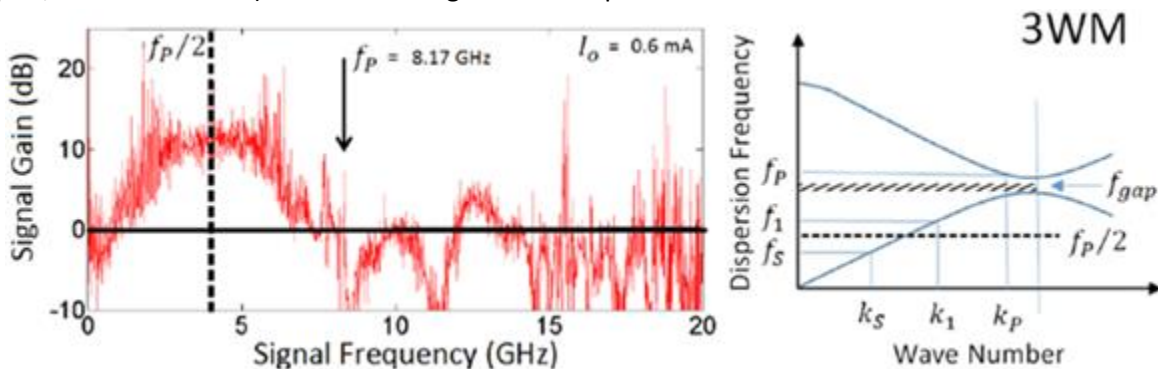


Figure 16: The gain profile and dispersion graph of an actual TKIP operating in 3WM mode. Copied from [3].

Mathematical Description

Coupled-Mode Equations

Now let us consider the mathematical description of parametric amplifiers. The 4WM mode of these devices can be understood by using coupled-mode equations analogous to those from nonlinear optics. To achieve a more complete understanding however, a more sophisticated Floquet-Bloch analysis will be required. Beginning with the Telegrapher's Equations, we will use the lossless form and note the dependence of the inductance on current. Since this analysis is for superconductors, we have

$$\frac{\partial V}{\partial z} = -L(I)\frac{\partial I}{\partial t} \quad (14)$$

$$\frac{\partial I}{\partial z} = -C\frac{\partial V}{\partial t}, \quad (15)$$

Where V is voltage, I is current, and L and C are the distributed inductance and capacitance of the transmission line, respectively. (14) and (15) can be rearranged as two partial differential equations as so:

$$\frac{\partial^2 V}{\partial z^2} - \frac{\partial}{\partial t} [L(I)C\frac{\partial V}{\partial t}] = 0 \quad (16)$$

$$\frac{\partial^2 I}{\partial z^2} - \frac{\partial}{\partial t} [L(I)C\frac{\partial I}{\partial t}] = 0 \quad (17)$$

Constraining our attention to (17), and substituting in (3), we see that we now have

$$\frac{\partial^2 I}{\partial z^2} = \frac{\partial}{\partial t} \left[CL_o \left(1 + \frac{I^2}{I_*^2} \right) \frac{\partial I}{\partial t} \right] \quad (18)$$

where the triple product of current terms (the third-order nonlinearity) is visible. (18) is a wave equation and has solutions of the form:

$$I = \frac{1}{2} \left(\sum_n A_n(z) e^{i(k_n z - \omega_n t)} + c.c. \right). \quad (19)$$

When multiple frequencies are present in the nonlinear medium, mixing will naturally occur. The triple current product causes all combinations of the three current terms to become viable, and those which satisfy the laws of conservation of energy and momentum will result in mixing processes that transfer energy from one frequency to another. After substituting (19) into (18), we make the assumption that the complex amplitudes vary slowly, i.e.

$$\left| \frac{d^2 A_n}{dz^2} \right| \ll \left| k_n \frac{dA_n}{dz} \right|. \quad (20)$$

To express concisely the condition of the conservation of energy we shall use the term δ_ω indicating the state of mathematically commensurate frequencies, i.e.

$$\omega_a + \omega_b + \omega_c - \omega_n = 0. \quad (21)$$

With the application of frequency orthogonality, the generic coupled-mode equation is contained in the following condensed form:

$$\frac{dA_n(z)}{dz} = \left(\frac{iCL_0}{8I_*^2}\right) \sum_{a,b,c=-\infty}^{\infty} \frac{\omega_c}{k_n} (\omega_a + \omega_b + \omega_c) A_a A_b A_c e^{i\Delta kz} \delta_\omega \quad (22)$$

where

$$\Delta k = k_a + k_b + k_c - k_n \quad (23)$$

is the phase matching factor. The convention of negating the “n” subscript terms in the above equations is simply a convenience which allows the differential equation index to refer to positive frequencies instead of negative ones.

In design and simulation one must account for harmonics and other mixing terms, however for the sake of clarity the present treatment will only consider the frequencies which are dominant in the mixing regimes which allow broadband gain, as described in the Parametric Amplifier section. Therefore we limit the summation in (22) from including all frequencies (from negative infinity to positive infinity) to only including four frequencies when considering four-wave mixing, and only three frequencies when limiting one’s interest to the degenerate case of four-wave mixing (in which case $\omega_3 = \omega_4$)—namely ω_p , ω_s , and ω_i for the pump, signal and idler respectively. These frequencies can be positive or negative. Thus we re-express (22) as

$$\frac{dA_n(z)}{dz} = \left(\frac{iCL_0}{8I_*^2}\right) \sum_{a,b,c=-3}^3 \frac{\omega_c}{k_n} (\omega_a + \omega_b + \omega_c) A_a A_b A_c e^{i\Delta kz} \delta_\omega \quad (24)$$

where

$$\omega_{1,2,3} = \omega_{s,i,p} \quad (25)$$

$$k_{1,2,3} = k_{s,i,p} \quad (26)$$

$$\omega_{-1,-2,-3} = -\omega_{s,i,p} \quad (27)$$

$$k_{-1,-2,-3} = -k_{s,i,p} \quad (28)$$

At this point the equation has essentially been reduced to a counting problem with the summation terms, which is admittedly nontrivial. Most TKIP papers and texts on nonlinear optics disagree on the exact coefficients (counting factors) of these equations², but according to my derivation the final form of the coupled-mode equations take the following form:

$$\begin{aligned} \frac{dA_p}{dz} &= \frac{i}{8v_p I_*^2} \left\{ \omega_p (|A_p|^2 + 2|A_s|^2 + 2|A_i|^2) A_p + 2 \left[\frac{(\omega_s + \omega_i)^2}{\omega_p} - 2\omega_s - 2\omega_i + \omega_p \right] A_s A_i A_p^* e^{i\Delta kz} \right\} \\ \frac{dA_s}{dz} &= \frac{i}{8v_p I_*^2} \left\{ \omega_s (|A_s|^2 + 2|A_p|^2 + 2|A_i|^2) A_s + \left[\frac{(\omega_p - \omega_i)^2}{\omega_s} \right] A_p^2 A_i^* e^{-i\Delta kz} \right\} \\ \frac{dA_i}{dz} &= \frac{i}{8v_p I_*^2} \left\{ \omega_i (|A_i|^2 + 2|A_p|^2 + 2|A_s|^2) A_i + \left[\frac{(\omega_p - \omega_s)^2}{\omega_i} \right] A_p^2 A_s^* e^{-i\Delta kz} \right\}. \end{aligned} \quad (29)$$

The differential equation regarding the pump is different from the others due to degenerate 4WM condition.

² The disagreement between authors probably arises from how one handles the degenerate condition in the counting—e.g. does the order of the duplicate degenerate frequencies matter in counting the permutations? Does one apply the degenerate condition and simplify from four terms to three before or after expanding the summation? Etc.

In the use cases of these TKIPs it is reasonable to establish two additional assumptions common to nonlinear optics. First that the pump will always have a much higher power than the signal. Therefore, to simplify further, one can make a “weak signal approximation”, i.e. any term that does not scale as $|A_p|^2$ or $|A_p|^3$ is negligible in comparison. And second, that the pump photons are not depleted as they travel along the line, or in other words, $\frac{dA_p}{dz} = 0$. After applying these assumptions and also utilizing the methods described in [34], one obtains analytical solutions for the above differential equations:

$$A_p(z) = A_p(0) \exp(\Delta\phi) \quad (30)$$

$$A_s(z) = A_s(0) \exp\left(i\left(\frac{2\omega_s}{\omega_p}\Delta\phi - \frac{\kappa}{2}\right)z\right) \left(\cosh(gz) + \frac{i\kappa}{2g} \sinh(gz)\right) \quad (31)$$

$$A_i(z) = A_s(0) \exp\left(i\left(\frac{2\omega_i}{\omega_p}\Delta\phi - \frac{\kappa}{2}\right)z\right) \left(\frac{i\Delta\phi}{g} \left(\frac{\omega_i}{\omega_p}\right) \sinh(gz)\right) \quad (32)$$

where

$$\Delta\phi = \frac{ik_p |A_p|^2 z}{8I_s^2} \quad (33)$$

$$\kappa = \Delta k + 2\Delta\phi \quad (34)$$

and g is the parametric gain coefficient

$$g = \frac{1}{2} \sqrt{\frac{\omega_s \omega_i}{\omega_p^2} (2\Delta\phi)^2 - \kappa^2}$$

At this point, since all nonlinearities and differential equations have been simplified, these equations can be solved for an estimate of the gain of a device. Note that this analysis does not incorporate higher harmonics or sidebands, nor is applicable to modeling 3WM. Nevertheless it provides an overview of the conventional approach to analyzing TKIPs. The inclusion of higher harmonics and sidebands is possible in principle by direct solution of the (differential) coupled-mode equations. A separate set of coupled-mode equations could be developed to describe 3WM, and these two sets of coupled-mode equations should be summed for a complete description of the mixing behavior of the TKIP.

Time-Domain

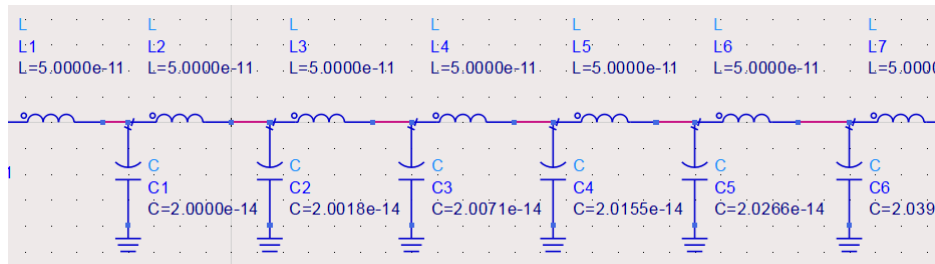


Figure 17: LC ladder circuit used to describe the TKIP, as drawn in a schematic capture application.

Alternatively, to simplify the math at the expense of processing time one could opt to perform a simulation in the time domain. This relies solely on knowledge of equations (14) and (15) above. When

the circuit is modeled as a LC ladder (see Figure 17) then the equations can be adjusted to resolve the positional differential like so:

$$V_{n+1} - V_n = -L_n \left(1 + \frac{I_n^2}{I_n^2} \right) \frac{dI_n}{dt} \quad (35)$$

$$I_n - I_{n-1} = -C_n \frac{dV_n}{dt} \quad (36)$$

where I_n refers to the current through the n th inductor, and V_n is the voltage across the n th capacitor. To avoid solving these differential equations at every frequency in a signal frequency sweep, one can instead take a large signal/small signal approach and solve the differential equations only for the pump, then take the Fourier Transform of the calculated currents that serve as a “bias point”. The time domain representation of the current then takes the following form:

$$I_n(t) = \frac{1}{2} \left(\sum_{m=1}^{\infty} I_n(m\omega_p) e^{im\omega_p t} + \sum_{m=1}^{\infty} I_n(\omega_m) e^{i\omega_m t} + c. c. \right) \quad (37)$$

where the first term is a summation of the pump harmonics and the second term is a summation of the pump sidebands defined as

$$\omega_m = (m - 1)\omega_p + \omega_s \quad (38)$$

Then a linearized version of the equations can be constructed:

$$\frac{I_n(\omega_m) - I_{n-1}(\omega_m)}{C_{n+1}} - \frac{I_{n-1}(\omega_m) - I_n(\omega_m)}{C_n} = \omega_m^2 L_n I_n(\omega_m) + \frac{\omega_m L_n}{4I_n^2} \gamma \quad (39)$$

Where γ is the mixing term, defined as

$$\gamma = \sum_{a,b=-\infty}^{\infty} \sum_{c=1}^{\infty} \omega_c I_n(a\omega_p) I_n(b\omega_p) I_n(\omega_c) \delta_{m,a+b+c} \quad (40)$$

The delta function is due to the fact that we have applied orthogonality, and are only concerned with the frequency ω_n . In this way the signal amplitude can be solved for in a perturbative fashion using matrix methods instead of slower differential equation solvers. Note that this approach is general—we have made only one assumption in order to linearize the equations—and it will serve for both 3WM and 4WM.

This approach was implemented, but proved too slow for design. Simulations would take hours to days. Since my design (utilizing a slow-wave structure) is composed of many very small unit cells the dimensions of the matrices become too cumbersome for my computing resources, but this description may still be useful to others with a different design. It can also still serve as a consistency check for a design produced using an alternative description. Output data of the FDTD large-signal analysis can be seen in Figure 18 and Figure 19.

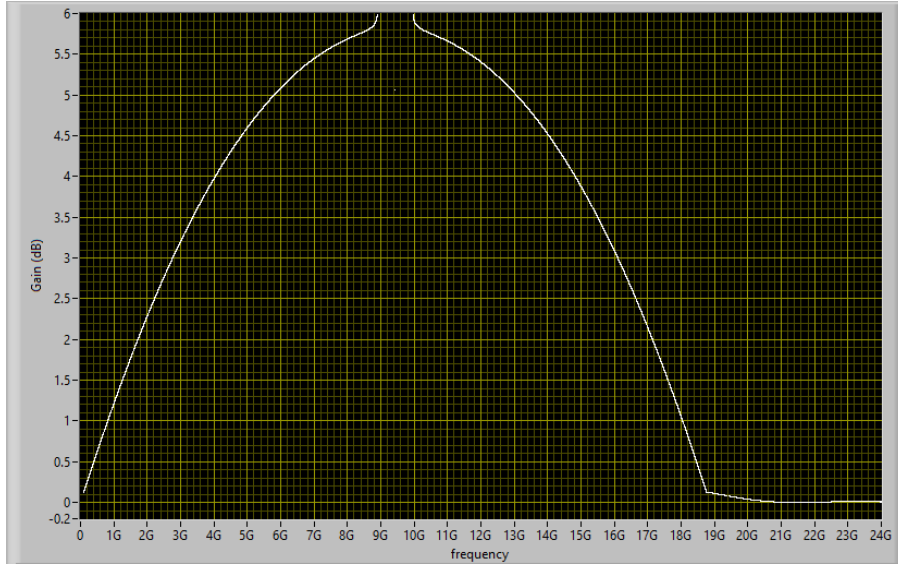


Figure 18: Example gain curve for a TKIP. The low gain is due to a shorter length for accommodating the smaller enclosure available.

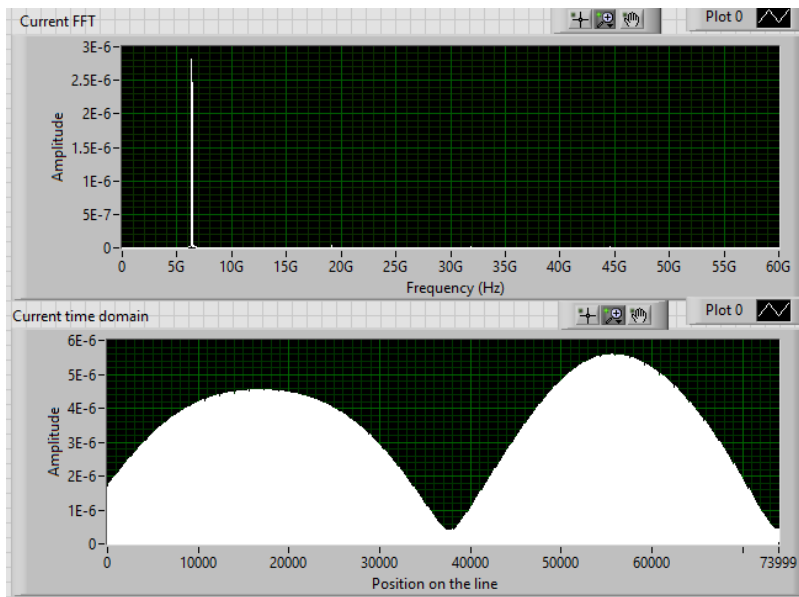


Figure 19: Large-signal FDTD output of a previous design.

Floquet-Bloch Analysis

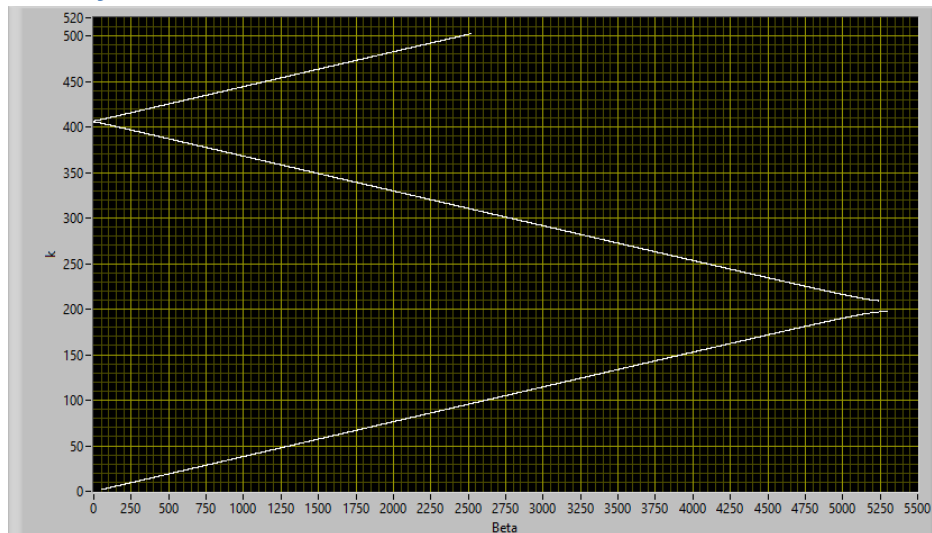


Figure 20: k - β diagram of a TKIP design

For greater simulation fidelity, one must take into account that due to the dispersion engineering and broken translational symmetry, the power flowing in the TKIP cannot be accurately described as a plane wave. This necessitates characterizing the RF waveforms using Floquet-Bloch analysis, which will introduce various subtle details:

- The phase velocity is not symmetric between passbands (across bandgaps), which causes any mixing processes which exist across bandgaps (all except the dominant 3WM process) to not be perfectly matched across a broad band. This is visible in the k - β diagram above (Figure 20). This is the inherent cause of the ripple in the gain profile, which is in addition to other causes such as impedance mismatches at the ends of the device.
- As can be seen in the k - β diagram above (Figure 20), due to the wrapping of the bands there are an infinite number of k 's that match each β (i.e. there are an infinite number of frequencies that match each wavenumber). In addition, the nonlinearity of the device causes self-phase modulation as well as mixing, causing e.g. the pump to exist in superposition in multiple passbands at matching wavenumbers. Noting that conservation of momentum depends on the wavenumber k , this phenomenon allows for a much broader range of phase matching in the device.

Readers interested in the mathematical derivation are referred to [2]. Similar to the time-domain description, the implementation of this approach is too slow for use in design, but could prove useful as sanity check for a design produced using an alternative description.

Challenges of the state-of-the-art

In the past 13 years since the inception of the TKIP, these devices have been studied in a limited fashion: how to reduce noise, reduce gain ripple, and increase in frequency. The noise has been reduced to levels approaching the quantum limit. The major contributors to noise are:

- a. Two-Level Systems (TLS), which are losses in the dielectric due to trapped states commonly encountered in amorphous materials [22]. I address this by using single-crystal SOI Silicon as the microstrip medium dielectric [35] as will be discussed later.
- b. Quasiparticles, due to the fact that the device is not at absolute zero and not all of the electrons have paired up into lossless Cooper Pairs. This can be reduced in two ways: lowering the operating temperature (not always possible, e.g. the ALMA radio telescopes are currently equipped with 4 Kelvin cryocoolers, therefore this is likely a fixed constraint from the perspective of the microwave engineer), or by increasing the T_c of the material as discussed earlier (e.g. my plan to use NbTiN).
- c. Heating of the chip due to high pump power [4] or fabrication defects [5]. As mentioned previously, my slow-wave structure design will reduce the severity of fabrication defects. Heating could be addressed by a 3WM design which requires less pump power.
- d. Imperfect test setups. Though designers do their best to prepare ideal test setups, there are realities that will not allow a measurement of the TKIP in isolation. For example there is usually a circulator placed after the TKIP to prevent reflections from subsequent components from entering into the other end of the TKIP and propagating backwards. This circulator has some loss and will add some noise. Also, at higher frequencies, it is not possible to switch between different loads or switch to a path that doesn't include the TKIP, so every noise measurement will include almost every component inside the cryostat.
- e. Additional, undesired sidebands due to the wideband nature of TKIPs [14].

The gain ripple has been studied extensively and is better understood but still challenges designers. We presume it is caused by a few contribution mechanisms:

- a. Impedance mismatches at the input and output of the device. This is reinforced by the fact that the ripples in the gain profile possess a periodic frequency corresponding to the length of the device [15]. My design with loading stubs allows the choice of characteristic impedance, which should aid in the reduction of impedance mismatches. I also hope to find new insights into this problem by performing on-wafer probing of these devices, where I can set the calibration plane at the start of the device the device instead of at the walls of the cryostat.
- b. Phase matching across passbands, as mentioned in the Four Wave Mixing section [2]. This could be addressed by a 3WM design.
- c. Heating of the chip due to high pump power [36]. This could be also be addressed by a 3WM design.

Chapter 2: SOI Microstrip

Motivation

Many superconducting parametric amplifiers are fabricated using CPW, which has the advantage of a simpler fabrication process and allows the realization of a wider range of characteristic impedances given typical fabrication constraints. I have examined the microstrip architecture to investigate the advantages that it offers. A CPW design with bends suffers from an unwanted slot-line mode and also increased radiation [24]. In general, microstrip also provides a greater kinetic inductance fraction (nonlinearity) [22], and when the substrate is thin then the distributed capacitance is greatly increased, allowing for a slower phase velocity yielding greater gains in a smaller footprint [1]. Additionally, using microstrip will allow for greater flexibility in designing unique structures aside from a transmission line, e.g. couplers and a balanced amplifier topology.

I have leveraged our group's established SOI (Silicon on Insulator) process to realize the microstrip circuit. This allows one to use only the thin silicon layer of the SOI chip, allowing for thinner substrates than would be possible to purchase or produce via thinning processes [37]. The typical process for microstrip fabrication involves the deposition of a dielectric, which by nature is amorphous and will contribute Two-Level Systems (TLS) noise [35]. The alternative to depositing a dielectric is to use both sides of a single-crystal Silicon wafer. However, thick substrates limit the maximum operating frequency without additional undesirable substrate modes and thinning processes for a thick substrate have limitations—a wafer cannot be thinned to any arbitrary thickness. Therefore SOI provides a clear path forward with a thin crystalline Silicon device layer.

A CPW device also suffers from TLS noise, but caused by a different source—the oxide which forms on the substrate in the gaps between conductors has the same amorphous nature, and this is where the electric fields of a CPW circuit are the most concentrated [38]. A SOI microstrip device will also produce oxide layers as a CPW device would, which will add some TLS contributions to the fringing fields of the microstrip field pattern.

Fabrication Process

The fabrication process begins with a SOI wafer, where the NbTiN ground plane is deposited on the exposed device layer. Subsequently the SOI wafer is inverted and permanently bonded to a carrier wafer so that the SOI handle and BOX layers can be removed. This will expose the other side of the SOI device Si layer where the circuit NbTiN layer can be deposited, forming the microstrip medium. Then a layer of gold is deposited to serve both as a contact layer for integrating into a test fixture and also to serve as “vias” to connect the ground contacts to the ground plane.

As described in the Kinetic Inductance section, NbTiN provides many advantages as a superconducting material, including its high T_c , high normal resistivity, and high bandgap. A relatively thin ($\sim 30\text{nm}$) film is deposited for the circuit layer to maximize the kinetic inductance nonlinearity, while a thick (multiple λ_L penetration depths) ground plane is deposited to prevent fields from passing through the ground conductor and entering the lossy materials on the other side.

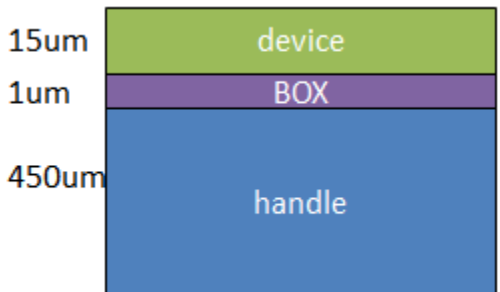
15 μm SOI was selected conservatively, and also because most of our group's SOI work uses this thickness, but it is not ideal for TKIP performance. 15 μm is a thick dielectric relative to the thickness and widths of the circuit traces, and violates the typical geometric assumptions of most microstrip models.

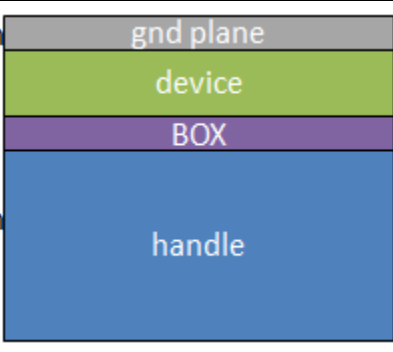
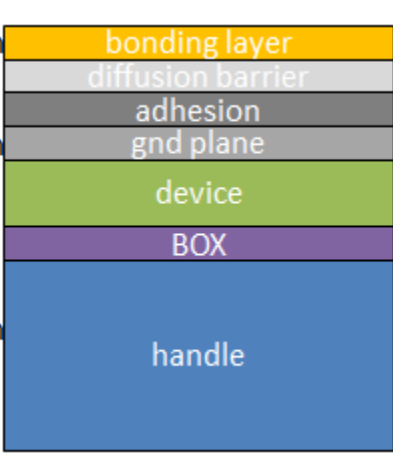
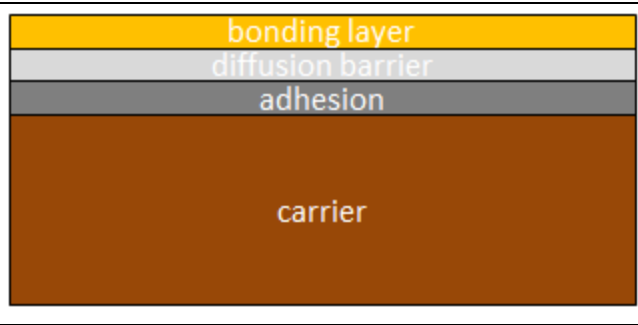
Furthermore, a thinner dielectric would provide more capacitance, bringing the characteristic impedance closer to the standard 50 Ohms, while also slowing down the wave, yielding more signal time in the amplification medium and thus greater gain. The Young Modulus of a material is defined as the ratio of stress to the strain or deformation of a material. Simply said, the higher the Young Modulus, the harder it is to bend or break a given sample. The Young Modulus scales as the square of the thickness of a material such that compared to a 5um SOI wafer, a 15um SOI wafer is 3² or 9 times stronger. This often can spell the difference between a finished device and a broken chip when releasing, handling and mounting chips. While we expect SOI chips could be successfully realized as thin as 3um, we conservatively used 15um SOI for this project to insure a high chip yield.

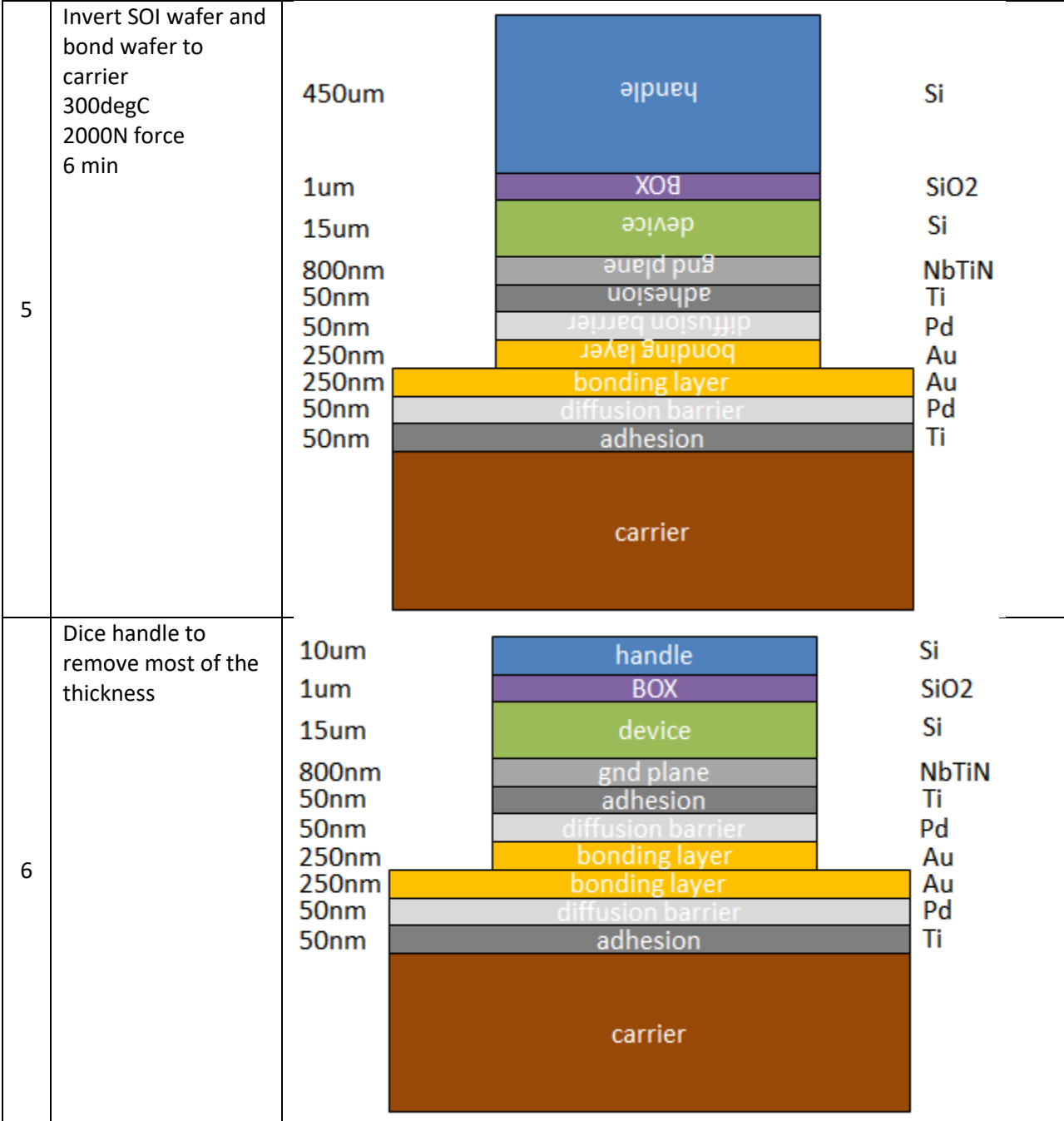
The bonding of the SOI to the Si carrier wafer is a critical, high-risk step in the process. The risks include any air or debris being trapped between the surfaces being bonded, which will cause blisters when the SOI handle is removed. It is not uncommon for imperfections to remain hidden until the wafer has undergone multiple vacuum cycles in subsequent steps, after which they begin to bubble up. Performing an annealing on the films improves the superconducting properties for TKIP use, but also poses a significant risk in exacerbating any imperfection in the bond. The other major risk is that the bond is not strong enough to hold the wafer during the dicing step of the SOI handle thinning (step 6).

For most of the development of this process the bonding used Cyclotene BCB as a bonding agent. This works well and is a valid substitute, but Au-Au bonding was also investigated as a bonding method because it should increase the thermal conductivity of the device stack, which will allow greater power carrying capability in the superconducting metals. Furthermore, Au deposited under the ground plane (step 3) can also act as an etch stop for the “ground expose etch” (step 16), which removes parts of the microstrip dielectric in order to make contact between the ground contacts on the circuit layer and the ground plane. It was discovered that Au-Au bonding with a Ti-Au stack directly on NbTiN caused some diffusion to occur between the layers during the heated bonding process, so a Palladium diffusion barrier was added to the stack. Christopher Moore was instrumental in developing the Au-Au bonding capability.

The etches are sensitive steps. When patterning the circuit layer (step 12), the SF₆ Ar chemistry will etch the Si underlayer quickly, so endpoint detection should be used to stop the etch immediately after the NbTiN layer is removed. When removing parts of the device layer to form vias in step 16, the same SF₆ Ar chemistry is used, but at a lower temperature to slow the rate, with the intent of etching the Si but not significantly etching the relatively thin NbTiN underlayer. Having a gold etch stop as mentioned above will eliminate the risk of accidentally etching all the way through the NbTiN ground plane, since that gold layer would remain to provide an electrical connection to the rest of the NbTiN ground plane not exposed by the etch. Theodore Singletary was the developer of this second SF₆ etch.

1	The process begins with a 15um SOI wafer	
---	--	--

2	Deposit a thick NbTiN ground plane	800nm 15um 1um 450um	 <p>gnd plane device BOX handle</p>	NbTiN Si SiO2 Si
3	Deposit TiPd diffusion barrier and Au bonding layer	250nm 50nm 50nm 800nm 15um 1um 450um	 <p>bonding layer diffusion barrier adhesion gnd plane device BOX handle</p>	Au Pd Ti NbTiN Si SiO2 Si
4	Deposit TiPd diffusion barrier and Au bonding layer on carrier wafer	250nm 50nm 50nm	 <p>bonding layer diffusion barrier adhesion carrier</p>	Au Pd Ti



7	<p>RIE to remove remaining handle Oxford ICP/RIE process SF6: 20 O2: 2 Pressure: 20 um Temperature: 20C He: 5 ICP: 500 First 10 min: RF: 100W For the rest of the etch: RF = 0W</p>	<p>1um 15um 800nm 50nm 50nm 250nm 250nm 50nm 50nm</p>		<p>SiO2 Si NbTiN Ti Pd Au Au Pd Ti</p>
8	<p>Remove BOX BOE 10:1 until hydrophobic, ~30 min</p>	<p>15um 800nm 50nm 50nm 250nm 250nm 50nm 50nm</p>		<p>Si NbTiN Ti Pd Au Au Pd Ti</p>
9	<p>Deposit NbTiN circuit layer</p>	<p>30nm 15um 800nm 50nm 50nm 250nm 250nm 50nm 50nm</p>		<p>NbTiN Si NbTiN Ti Pd Au Au Pd Ti</p>

10	<p>Spin HMDS Spin nLof 2020 6000 RPM 40 s Bake 110 C for 1 min</p>	<p>30nm 15um 800nm 50nm 50nm 250nm 250nm 50nm 50nm</p> <p>PR circuit layer device gnd plane adhesion diffusion barrier bonding layer bonding layer diffusion barrier adhesion</p> <p>carrier</p> <p>NbTiN Si NbTiN Ti Pd Au Au Pd Ti</p>
11	<p>Circuit layer photolithography Expose microwriter ML3 75mJ/cm² Image reversal bake 110 C 1 min Develop with AZ 300 MIF</p>	<p>30nm 15um 800nm 50nm 50nm 250nm 250nm 50nm 50nm</p> <p>PR PR circuit layer device gnd plane adhesion diffusion barrier bonding layer bonding layer diffusion barrier adhesion</p> <p>carrier</p> <p>NbTiN Si NbTiN Ti Pd Au Au Pd Ti</p>

12	<p>Circuit layer etch Oxford SF6 Ar chemistry 30W RIE 1 min</p>	<p>30nm 15um 800nm 50nm 50nm 250nm 250nm 50nm 50nm</p>		<p>NbTiN Si NbTiN Ti Pd Au Au Pd Ti</p>
13	<p>Strip PR NMP 80degC 30min</p>	<p>30nm 15um 800nm 50nm 50nm 250nm 250nm 50nm 50nm</p>		<p>NbTiN Si NbTiN Ti Pd Au Au Pd Ti</p>

14	<p>spin HMDS Spin AZ 10XT 520cP 5000 RPM 40s Bake 100 C for 2 min</p>	<p>30nm PR</p> <p>15um device</p> <p>800nm gnd plane</p> <p>50nm adhesion</p> <p>50nm diffusion barrier</p> <p>250nm bonding layer</p> <p>250nm bonding layer</p> <p>50nm diffusion barrier</p> <p>50nm adhesion</p> <p>carrier</p> <p>NbTiN Si NbTiN Ti Pd Au Au Pd Ti</p>
15	<p>Gnd expose lithography Expose microwriter ML3 small features job 75mJ/cm², large features job 300mJ/cm² Develop with AZ 300 MIF</p>	<p>30nm PR</p> <p>15um device</p> <p>800nm gnd plane</p> <p>50nm adhesion</p> <p>50nm diffusion barrier</p> <p>250nm bonding layer</p> <p>250nm bonding layer</p> <p>50nm diffusion barrier</p> <p>50nm adhesion</p> <p>carrier</p> <p>NbTiN Si NbTiN Ti Pd Au Au Pd Ti</p>

16	<p>Gnd expose etch Oxford RIE SF6 Ar chemistry 20min</p>	<p>30nm PR</p> <p>15um device</p> <p>800nm gnd plane</p> <p>50nm adhesion</p> <p>50nm diffusion barrier</p> <p>250nm bonding layer</p> <p>250nm bonding layer</p> <p>50nm diffusion barrier</p> <p>50nm adhesion</p> <p>carrier</p> <p>NbTiN Si NbTiN Ti Pd Au Au Pd Ti</p>
17	<p>Strip PR Acetone</p>	<p>30nm</p> <p>15um device</p> <p>800nm gnd plane</p> <p>50nm adhesion</p> <p>50nm diffusion barrier</p> <p>250nm bonding layer</p> <p>250nm bonding layer</p> <p>50nm diffusion barrier</p> <p>50nm adhesion</p> <p>carrier</p> <p>NbTiN Si NbTiN Ti Pd Au Au Pd Ti</p>

<p>18</p>	<p>Spin AZ4330 4000 RPM 40s Bake 100 C for 1 min</p>	<p>30nm 15um 800nm 50nm 50nm 250nm 250nm 50nm 50nm</p> <p>PR device gnd plane adhesion diffusion barrier bonding layer bonding layer diffusion barrier adhesion</p> <p>carrier</p> <p>NbTiN Si NbTiN Ti Pd Au Au Pd Ti</p>
<p>19</p>	<p>Contact layer and via lithography Expose microwriter ML3 250mJ/cm² Develop using AZ400K 1:4 with DI</p>	<p>30nm 15um 800nm 50nm 50nm 250nm 250nm 50nm 50nm</p> <p>PR device gnd plane adhesion diffusion barrier bonding layer bonding layer diffusion barrier adhesion</p> <p>carrier</p> <p>NbTiN Si NbTiN Ti Pd Au Au Pd Ti</p>

20	Deposit contact layer and ground connection	<p>30nm 15um 800nm 50nm 50nm 250nm 250nm 50nm 50nm</p> <p>PR device gnd plane adhesion diffusion barrier bonding layer bonding layer diffusion barrier adhesion</p> <p>100nm Au 15nm Ti</p> <p>Au Pd Ti</p> <p>carrier</p>
21	Strip PR and liftoff TiAu Acetone	<p>30nm 15um 800nm 50nm 50nm 250nm 250nm 50nm 50nm</p> <p>NbTiN Si device gnd plane adhesion diffusion barrier bonding layer bonding layer diffusion barrier adhesion</p> <p>100nm Au 15nm Ti</p> <p>Au Pd Ti</p> <p>carrier</p>
22	Device dicing	

Fabrication Results

Devices were fabricated using a recipe very similar to the above, but the bonding process used BCB instead of Au-Au bonding. Another difference is that after deposition of the circuit layer, the film was annealed at 250degC for 10 minutes. Very little work has been done to characterize annealed thin NbTiN films to this point, but previous work has suggested that this anneal step will increase the film resistivity by an expected 3% (from 99.4 to 102.38 $\mu\Omega\cdot\text{cm}$) and the superconducting transition temperature (critical temperature T_c) from approximately 14.8 to an expected 15.1 Kelvin [39]. Δ_0 , the

superconducting bandgap at 0 Kelvin defined in BCS theory and described in equation (5), is a function of T_c , and therefore it will also increase. This will cause the London penetration depth λ_L to shrink from approximately 285nm to an expected 273nm. These are advantageous qualities for a TKIP device as described in the Kinetic Inductance section. Additionally, the devices were designed with radial stubs to create a virtual short to the ground plane instead of fabricating vias as described in [40].

The fabricated devices included a sweep of mismatched transmission line resonators, i.e. a transmission line which is not matched to the characteristic impedance (in this case 50 Ohms), which will cause a standing-wave pattern. This can be explained using the formula for the input impedance of a terminated lossless transmission line:

$$Z_{in} = Z_o \frac{Z_L + jZ_o \tan(\beta\ell)}{Z_o + jZ_L \tan(\beta\ell)} \quad (41)$$

where Z_o is the characteristic impedance of the transmission line (mismatched in this case) and Z_L is the load impedance (which is matched). When the electrical length of the line, $\beta\ell$, is a quarter wavelength then $\beta\ell = \frac{\pi}{2}$, and $\tan\left(\frac{\pi}{2}\right) = \infty$, leaving $Z_{in} = \frac{Z_o^2}{Z_L}$. This is the “quarter wave transformer” effect. This will be a peak in the S_{11} response, or the worst match. At half a wavelength, $\beta\ell = \pi$, $\tan(\pi) = 0$, leaving $Z_{in} = Z_L$, which is a perfect match in this case. This allows one to extract the characteristic impedance and phase constant of the line from the data.

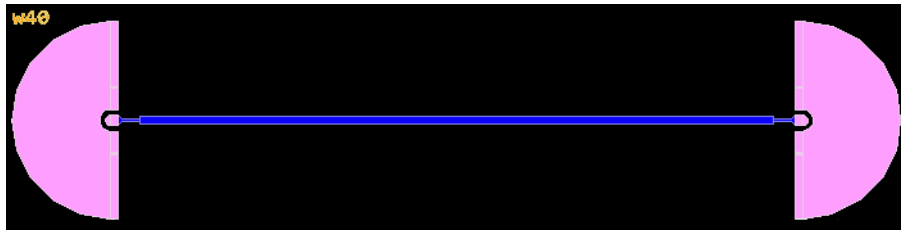


Figure 21: An image of the CAD mask of a mismatched resonator. The pink is the gold contact pad, the blue is NbTiN transmission line. The length of the widened section is 3536um.

For brevity, I will only discuss four of the swept resonator widths. To fit these superconducting lines, one begins with the capacitance and magnetic inductance of a perfect conductor of the same geometry.

line width (um)	PEC Zo (Ω)	PEC ε_eff	Lm (H/m)	C (F/m)
1.1	89.03	9.81	9.30E-07	1.17E-10
9.1	47.91	10.65	5.22E-07	2.27E-10
29.1	26.6	11.9	3.06E-07	4.33E-10
39.1	21.99	12.34	2.58E-07	5.33E-10

Then one adds additional inductance (the contribution from the kinetic inductance) until the model matches the measured data.

line width (um)	L_KI (H/m)	Fractional KI	Measured Zo (Ω)	v_p (m/s)	λ_L (nm)
1.1	5.58E-06	0.86	235.5	3.62E+07	413.47
9.1	5.90E-07	0.53	69.94	6.29E+07	386.70
29.1	1.30E-07	0.41	31.75	7.28E+07	324.60

39.1	1.00E-07	0.30	25.91	7.24E+07	330.00
-------------	----------	------	-------	----------	--------

where v_p is the phase velocity $= \frac{1}{\sqrt{L_{tot}C}}$, fractional KI $= \frac{L_{KI}}{L_{tot}}$, and λ_L has been calculated using equation (5). The penetration depth λ_L does not agree with the expected value of 273nm, but it is known that the Lakeshore CPX-1.5K Cryogenic RF on-wafer probing station used tends to heat the device under test since it is difficult to sufficiently thermalize the probe arms. The probe station is operated with liquid Helium, which provides an operating temperature of approximately 4.2 Kelvin, but past measurements have reported device temperatures of 8 Kelvin or more. Therefore this discrepancy can be used to calculate the actual temperature of the resonators at the time of measurement. The penetration depth varies with frequency as described in the BCS theory [41]

$$\lambda(T) = \sqrt{\frac{\hbar}{\pi\mu_o\Delta(T)\sigma}} \quad (42)$$

What is really varying with temperature is the superconducting gap Δ . Popel proposed a formula for its dependence on temperature [25]:

$$\Delta(T) = \Delta_o \sqrt{\cos\left[\frac{\pi}{2}\left(\frac{T}{T_c}\right)^2\right]} \quad (43)$$

Solving these equations for T the actual temperature suggests that the temperature at the time of measurement was actually not far from T_c :

line width (um)	T [K]
1.1	14.16
9.1	13.85
29.1	12.34
39.1	12.55

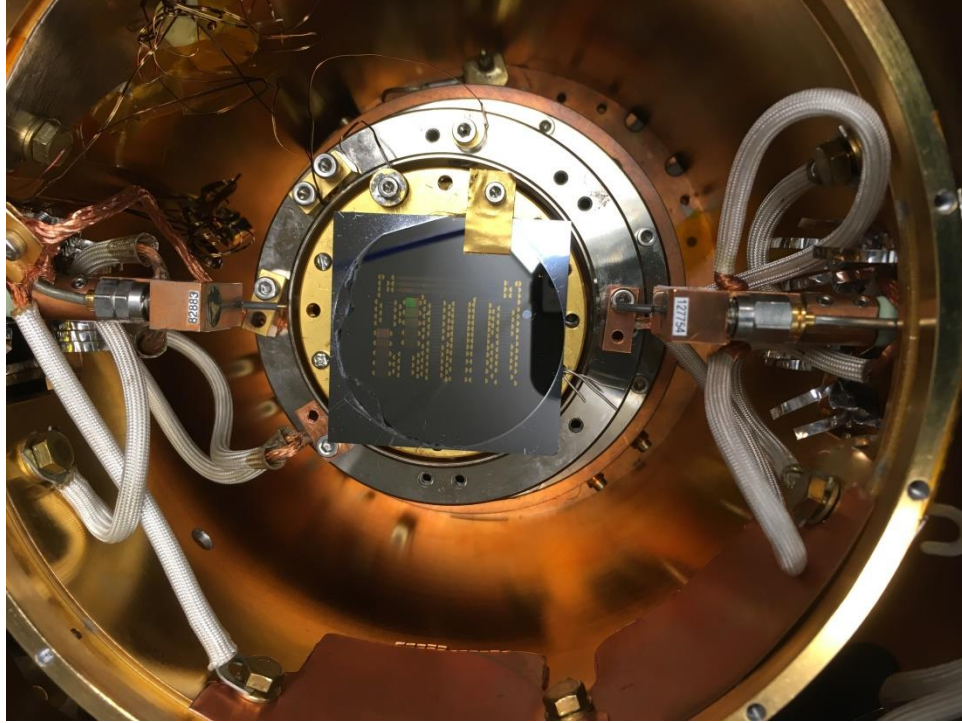
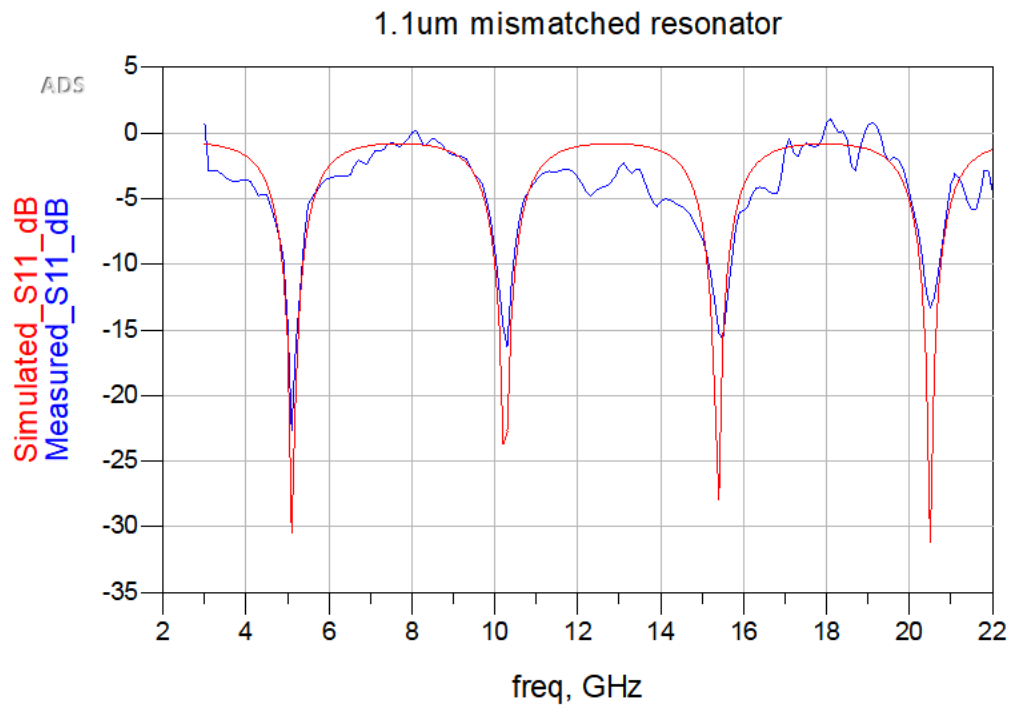
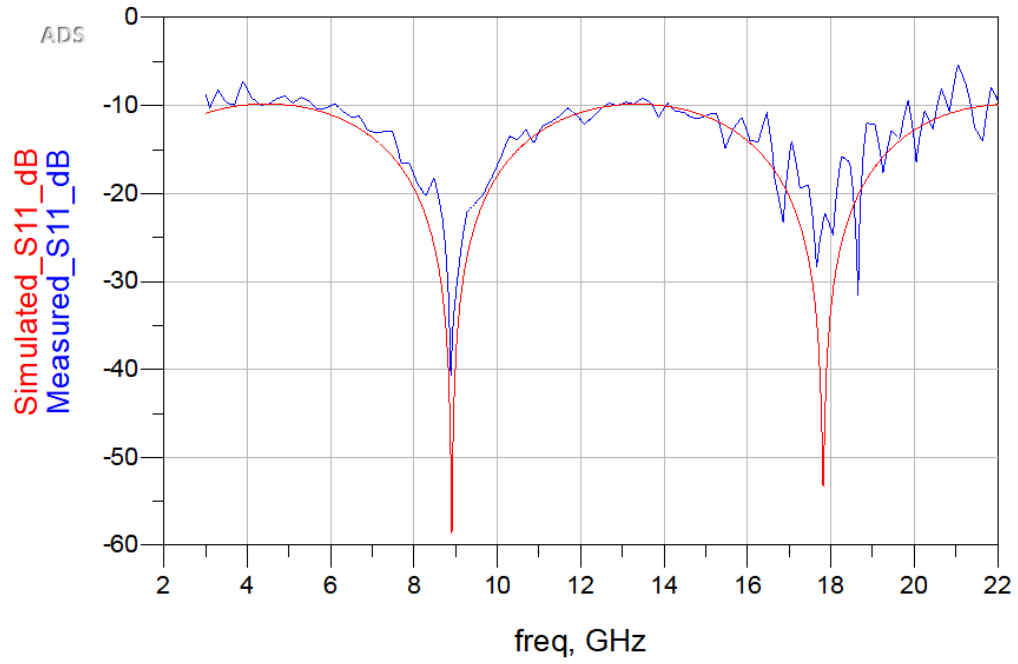


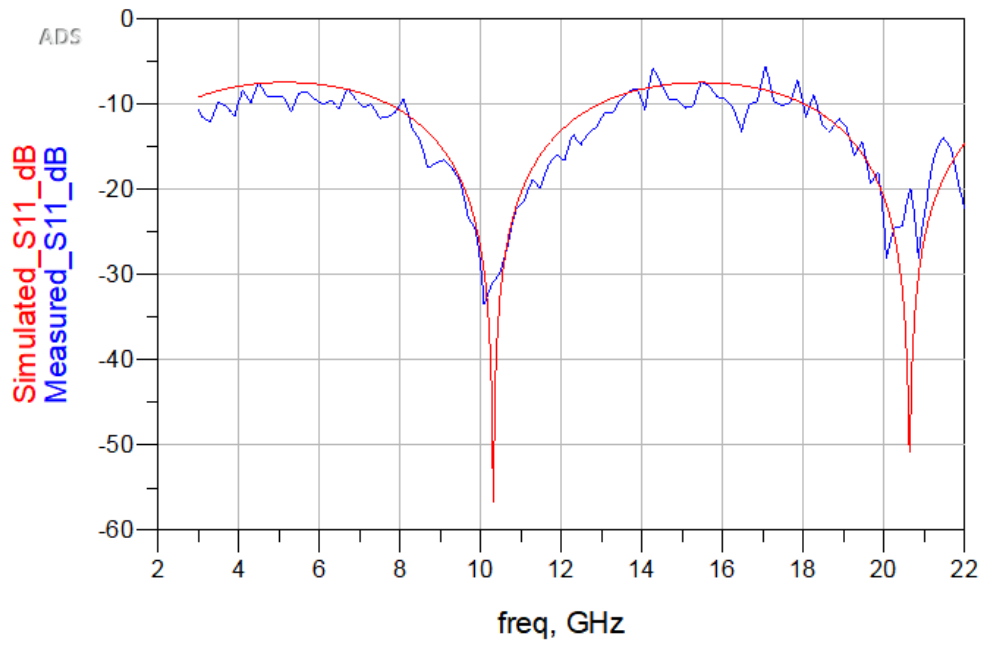
Figure 22: The fabricated wafer in the on-wafer probe station.

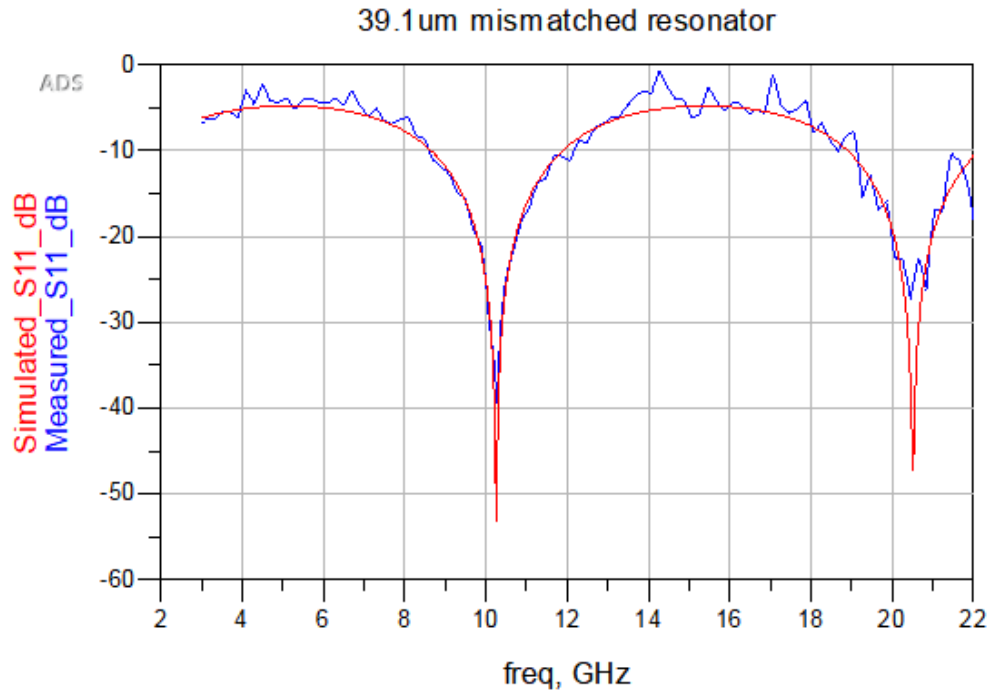


9.1um mismatched resonator



29.1um mismatched resonator





In conclusion, SOI microstrip devices were successfully fabricated using a predecessor of the presented recipe, and were measured in an on-wafer probing station and found to be in reasonable agreement with modeled values.

Chapter 3: Circuit Modeling

Motivation behind the device structure

Given the advantages of implementing a slow-wave structure as mentioned in the Traveling-Wave section above, a design utilizing periodic capacitive-loading stubs was explored. It was expected that each stub would add additional capacitance to each unit length of line proportional to the length of the stub. This expectation arose from considering each loading stub to be acting as a parallel-plate capacitor, which can be calculated with the well-known formula

$$C = \epsilon_r \epsilon_0 \frac{A}{d} \quad (44)$$

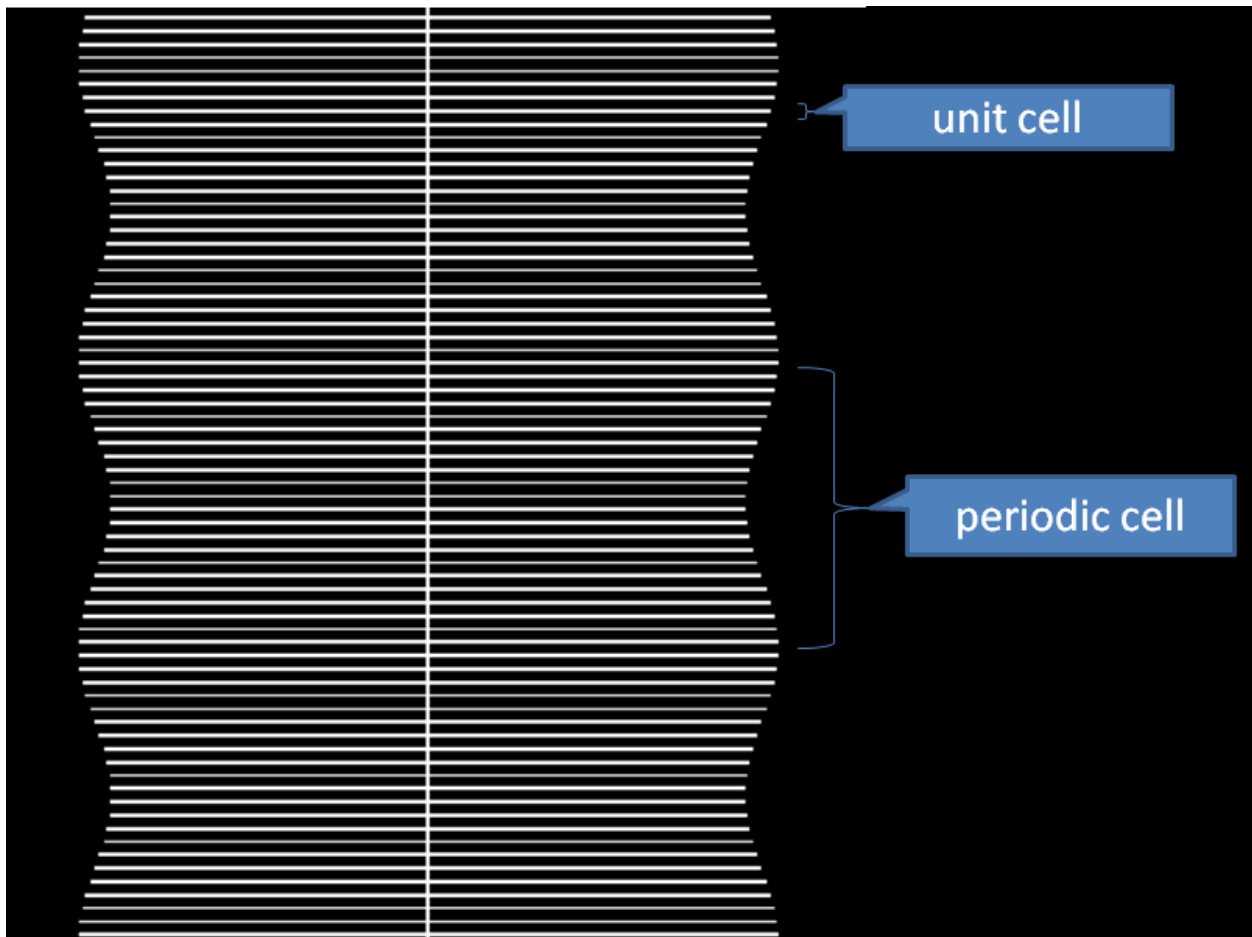


Figure 23: Graphic of the circuit CAD, showing the appearance of the stub-loaded microstrip slow-wave transmission line.

The above equation shows that the capacitance exhibited by a parallel-plate capacitor is linearly proportional to the area of the plates. A longer stub would have greater area and therefore contribute greater capacitance to the transmission line. This is desirable because the phase velocity of a transmission line is inversely related to the capacitance as shown in (10). Furthermore, the addition of loading structures provides additional flexibilities in a design, such as more control over impedances and the ability to add stopbands, e.g. through the quarter-wave length of loading stubs. These stopbands

can be gainfully employed in TKIPs for suppressing the third harmonic propagation, as discussed in the Dispersion Engineering section.

Transmission line theory

At the most basic level, TKIPs are transmission lines. Lossless transmission lines can be modeled using a lumped-element approximation where the characteristic impedance Z_o and phase constant β of the transmission line are expressed as n discrete pairs of inductors and capacitors, as shown in Figure 24. This approximation can be extended to include the effects of loss, however this is not applicable to a superconducting application, and will be left to another author.

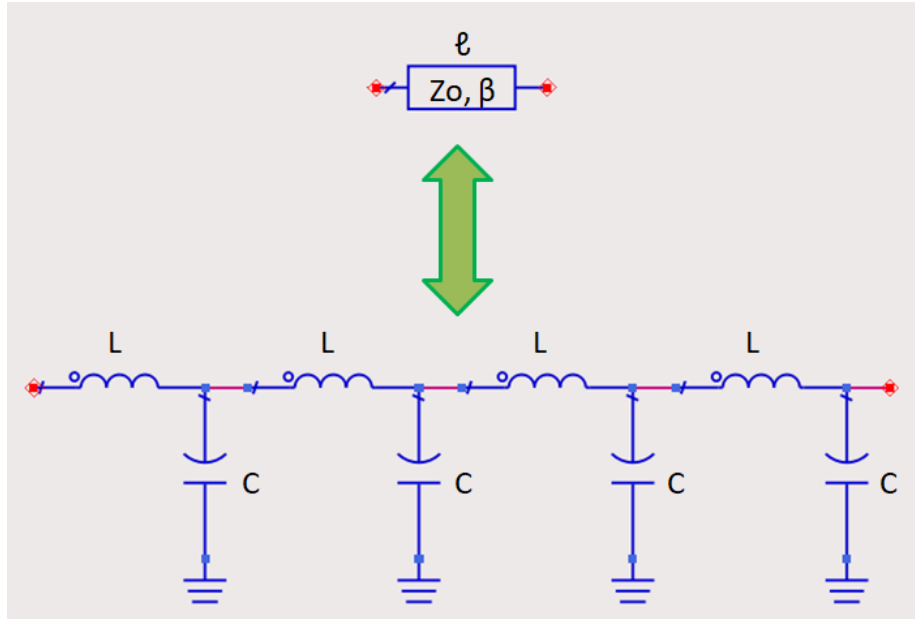


Figure 24: Lumped-element approximation of a transmission line.

In this approximation the lossless transmission line is divided into many small sections (four shown in Figure 24) where each section is electrically short relative to a wavelength at the frequencies of interest, i.e.

$$\Delta \ell \ll \lambda \quad (45)$$

where $\Delta \ell$ is the physical length approximated by each L/C section,

$$\Delta \ell = \frac{\theta}{\beta} \quad (46)$$

$$Z_o = \sqrt{\frac{L}{C}} \quad (47)$$

and

$$\beta = n\omega\sqrt{LC} \quad (48)$$

This lumped element model is an approximation and, as such, has limitations on its accuracy. Yet all the circuit models offered in published work are based on this lumped element approximation [1, 4, 14, 31,

42, 43]. More recent publications do not disclose the circuit model used. What's more, some TKIP devices have resonant structures and these are also modeled with lumped element. In my modeling efforts this approximation was never accurate in capturing the effects of the actual device.

Inaccuracy of the lumped element model

Initial attempts to model my geometries using the published lumped-element models always proved ineffective. For example, to model a 2um wide line loaded with ten 2um wide, 400um long open-circuit stubs with 16um between each stub (18um unit length), Figure 26 shows a comparison between an open-circuit transmission line model for the stubs versus using the lumped element model offered in [42]. Figure 25 shows the circuit model used.

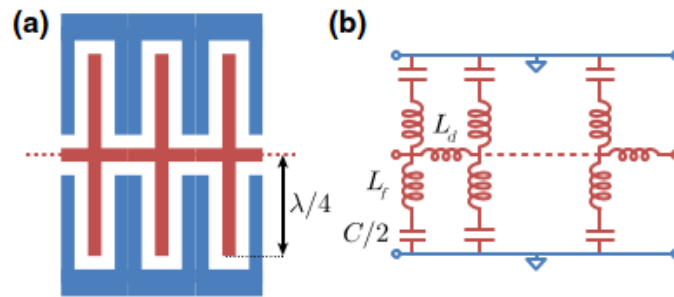


Figure 25: The circuit model used in [42].

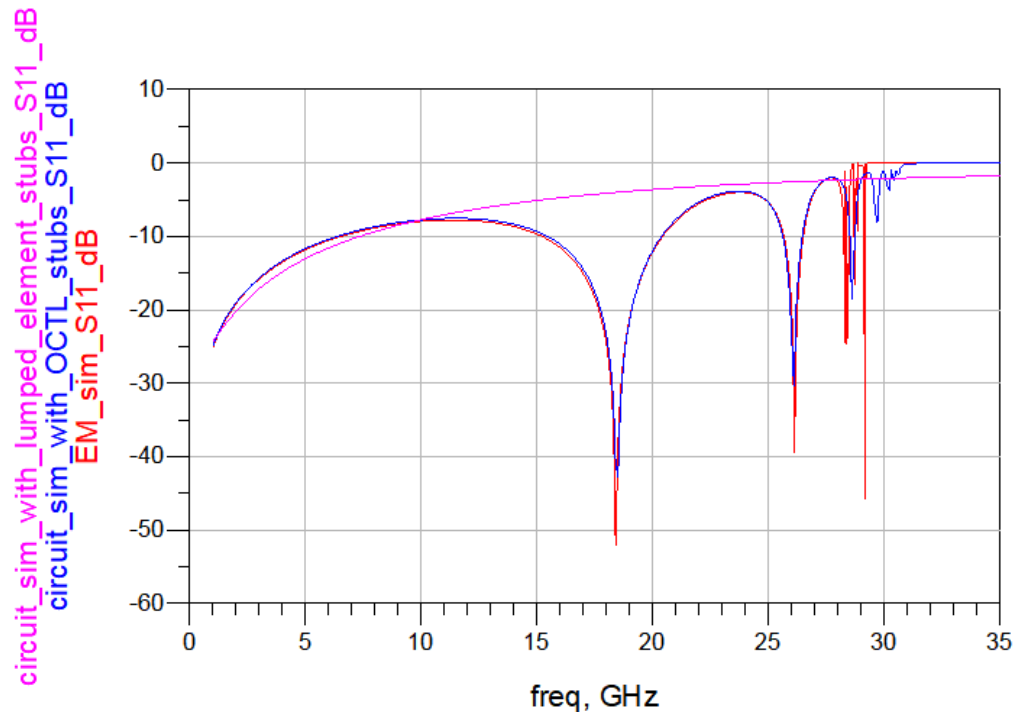


Figure 26: Comparison of an open-circuit transmission line (OCTL) model for stubs along a transmission line vs. using the lumped element model proposed in [42]

It is possible that this model is appropriate for their geometries, but it is obviously not compatible with case. Also, be aware that there are several mistakes in that article's ([42]) Appendix B on ABCD transfer matrices. This is one example of all attempted instances of using lumped element models to simulate

the effect of loading stubs along a transmission line, and all other attempts resulted in similar inaccuracy.

Model used for the stub-loaded line

Given that the lumped element approximation did not prove effective in my work, a different approach was sought. In such cases, it is wise to begin with a simple model and add complexity as needed. The entire structure (shown in Figure 23) was broken down into unit cells as shown in Figure 27.

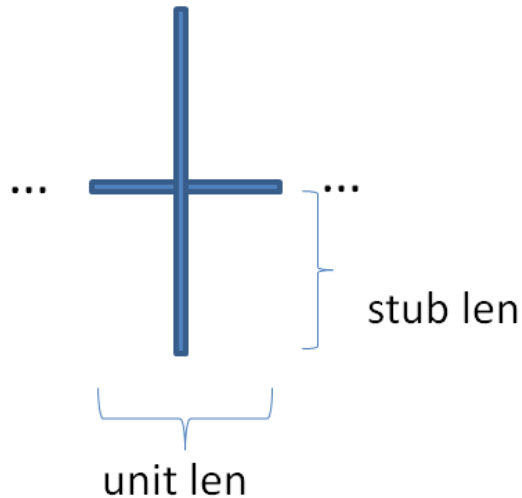


Figure 27: A unit cell consisting of a short length of transmission line and bilateral shunt stubs.

As this structure is essentially composed of only a short length of transmission line with bilateral shunt stubs (assuming no coupling between the stubs, as discussed later), this circuit was implemented and tested as displayed in Figure 28.

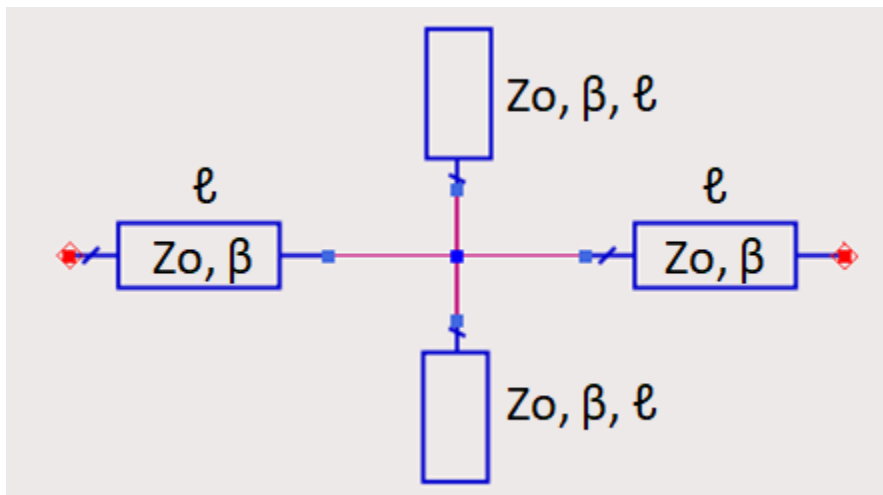


Figure 28: The circuit model for a transmission line bisected by bilateral shunt stubs.

Critics will point out that this model is very basic. I see this as a positive fact. It isn't fancy or novel, but it models the behavior of the circuit more accurately than published models, with fewer assumptions and computing resources.

With a trusted unit cell circuit model one can begin to design more sophisticated structures. Since these devices are long cascades of many unit cells it makes sense to use ABCD matrices instead of S-parameters. The ABCD matrices of these discrete elements are

$$\begin{bmatrix} A & B \\ C & D \end{bmatrix}_{\text{transmission line}} = \begin{bmatrix} \cos(\beta\ell) & jZ_o \sin(\beta\ell) \\ \frac{j}{Z_o} \sin(\beta\ell) & \cos(\beta\ell) \end{bmatrix} \quad (49)$$

$$\begin{bmatrix} A & B \\ C & D \end{bmatrix}_{\text{open circuit shunt stub}} = \begin{bmatrix} 1 & 0 \\ \frac{j}{Z_o} \tan(\beta\ell) & 1 \end{bmatrix} \quad (50)$$

And therefore the matrix for the full unit cell is

$$\begin{bmatrix} A & B \\ C & D \end{bmatrix}_{\text{unit cell}} = \begin{bmatrix} A & B \\ C & D \end{bmatrix}_{\text{transmission line}} \cdot \begin{bmatrix} A & B \\ C & D \end{bmatrix}_{\text{open circuit shunt stub}} \cdot \begin{bmatrix} A & B \\ C & D \end{bmatrix}_{\text{open circuit shunt stub}} \cdot \begin{bmatrix} A & B \\ C & D \end{bmatrix}_{\text{transmission line}} \quad (51)$$

At this point one implements dispersion engineering, creating a periodic variation along the cascade. This composes the "periodic cell" called out in Figure 23. This is done by first determining the device's desired pump frequency. This will indicate the frequency for the first bandgap, which must be immediately above or below the desired pump frequency. This yields the periodic cell length, which must be one half of a wavelength of the first bandgap frequency. Then the periodic cell length is divided into N cells, determined by the minimum stub spacing which will reduce stub coupling to a negligible level, as discussed below. Then N unit cell ABCD matrices are generated, varying one of the parameters ($Z_o, \beta, \text{ or } \ell$) in that unit cell. I chose to vary the length ℓ of the stubs sinusoidally along the periodic cell length, as it produced the deepest, narrowest stopband with the sharpest edges, however this should be investigated further to identify a proven optimal technique. Perhaps one could apply filter theory to implement a binomial (maximally flat) or Chebyshev (equal ripple) variation across a periodic cell. But this periodic variation can be as simple as varying a parameter, e.g. Z_o , of a single unit cell in each periodic cell. Any variation in a periodic cell will produce a reflection at the first bandgap frequency, and the cascade of many periodic cells will reinforce that reflection magnitude to the point that said frequencies will not propagate along the line, creating the desired bandgap.

Once the N unit cells of the periodic cell are generated, they must be cascaded, i.e.

$$\begin{bmatrix} A & B \\ C & D \end{bmatrix}_{\text{periodic cell}} = \prod_{n=1}^N \begin{bmatrix} A & B \\ C & D \end{bmatrix}_{\text{unit cell } n} \quad (52)$$

Then the ABCD matrix of the entire structure can be calculated by cascading the periodic cells:

$$\begin{bmatrix} A & B \\ C & D \end{bmatrix}_{\text{TKIP}} = \begin{bmatrix} A & B \\ C & D \end{bmatrix}_{\text{periodic cell}}^m \quad (53)$$

where m is the number of periodic cells in the full TKIP device, determined by the desired gain or available space on one's wafer.

Note that this design has not addressed the problem of the third harmonic of the pump. The author has chosen to ameliorate this issue by choosing the length of the loading stubs to be a quarter of the wavelength of the pump's third harmonic to effectively create a separate bandgap for that frequency range. However, note that this design approach can be applied in an entirely generic sense. If a designer does not wish to use periodic loading stubs then the unit cell simply becomes the ABCD of a transmission line. Then this forms part of a periodic cell, which will include the dispersion engineering of whatever form is desired by the designer, including the traditional stepped impedances. And then the dispersion engineering for the third harmonic can be incorporated as part of the modulation that occurs in the periodic cell.

To confirm the desired performance, ABCD matrices can be easily converted to S-parameters [44]. The first principal characteristic of a transmission line is the impedance. Since this transmission line has been altered by periodic loadings, the electromagnetic propagation is no longer described by a plane wave [2], but rather by a Bloch wave, and is characterized by a Bloch impedance. This is calculated by [44]

$$Z_B = \pm \frac{-2BZ_o}{A - D \mp \sqrt{(A + D)^2 - 4}} \quad (54)$$

which of course will simplify nicely for a symmetric unit cell where $A = D$.

The other defining parameter of a transmission line is the propagation constant $\gamma = \alpha + j\beta$. This will exhibit the passband and stopband characteristics and is also needed for modeling the gain. This is calculated in a periodic structure as [44]:

$$\gamma = \frac{\cosh^{-1}\left(\frac{A + D}{2}\right)}{d} \quad (55)$$

where d is the physical length of the circuit being analyzed. Due to the mathematical nature of γ , at any given frequency it is either all real or all imaginary. The frequencies at which it is real are the stopbands, and the regions where it is imaginary are the passbands.

This design of using stub-loaded lines is not novel, however the model used for the circuit described in [24] is not revealed. This model, therefore, fills that void and provides TKIP designers a tool for simulating and developing these circuits.

Stub Coupling

Coupled line theory

The discussion in this section requires a familiarity with coupled line theory, which can be studied most textbooks that discuss transmission lines, microwave engineering, or electromagnetic structures. Some examples include [44, 45]. This foundational knowledge usually only considers two circuit conductors coupled together, and explains how any arbitrary signal can be described using a superposition of "even" and "odd" modes. When extending this theory to an arbitrary number of conductors, a system with N signal conductors (i.e. not counting the "return" or "ground" conductor) will produce N distinct propagating modes [46, 47]. Each mode will have its own characteristic impedance and phase constant.

When considering coupled superconducting lines there are some wrinkles that need to be considered. The kinetic inductance of the superconductors adds a nonlinear inductance in the line, but this does not factor in to the mutual inductance between lines. This is because the kinetic inductance does not actually produce a magnetic field, but is called an inductance because its energy storage mechanism follows similar mathematics as that of an inductor. An example consequence of this is that most EM tools will not discriminate between these different types of inductances and will not give accurate results for coupled lines. Some authors are careful about this distinction [48] while others are not. For example, [49] indicates that to determine the contribution of KI in coupled lines that one should integrate the magnetic field inside the conductor. Such an approach would produce nonphysical results.

How to model coupling in an electromagnetic simulator

First, before expending significant effort in developing a theoretical framework, it makes sense to perform an initial simulation to determine if coupling is even present. While this discussion will explain the process using the Sonnet EM software, the principles are universal. Sonnet EM is used because it permits a user to define a surface impedance for a conductor, which is an effective way to model superconductors. The theory and equations to execute this can be found in [50].

To calculate the coupling parameters using Sonnet version 18, one must draw two lines with the desired widths and spacing, connecting to the box walls on either side, as shown in Figure 29.

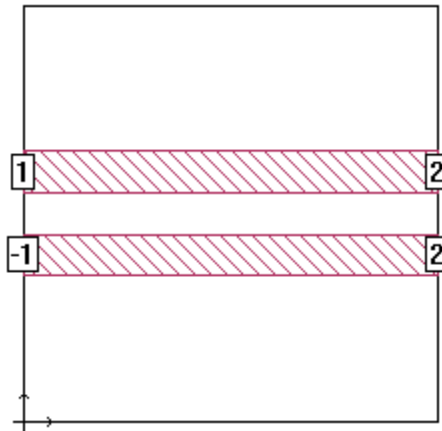


Figure 29: Setup to calculate coupling parameters in Sonnet.

In this way, port 1's stimulus is set up in a "differential" configuration, while port 2 has a "common" stimulus configuration. These are related, but not identical, to the even and odd modes, respectively, that engineers are accustomed to. When processing the circuit, Sonnet will de-embed the ports from the walls and calculate a "port Z_o " and "port ϵ_{eff} " for each port. In this setup port 1's Z_o is the differential mode characteristic impedance, or Z_{diff} (which must be converted to Z_{odd}), and the dielectric constant ϵ_{eff} is ϵ_{odd} directly. Similarly, port 2's Z_o and ϵ_{eff} are Z_{common} (which must be converted to Z_{even}) and ϵ_{even} . These conversions are simple scale factors:

$$Z_{odd} = \frac{Z_{diff}}{2} \quad (56)$$

$$Z_{even} = 2 * Z_{common} \quad (57)$$

Once the even and odd mode parameters are obtained one can calculate the self- and mutual inductances and capacitances, respectively. These are found by:

$$L_s = \frac{Z_e\sqrt{\epsilon_e} + Z_o\sqrt{\epsilon_o}}{2c} \quad (58)$$

$$L_m = \frac{Z_e\sqrt{\epsilon_e} - Z_o\sqrt{\epsilon_o}}{2c} \quad (59)$$

$$C_s = \frac{\sqrt{\epsilon_e}}{2cZ_e} + \frac{\sqrt{\epsilon_o}}{2cZ_o} = \frac{Z_o\sqrt{\epsilon_e} + Z_e\sqrt{\epsilon_o}}{2cZ_eZ_o} \quad (60)$$

$$C_m = \frac{\sqrt{\epsilon_e}}{2cZ_e} - \frac{\sqrt{\epsilon_o}}{2cZ_o} = \frac{Z_o\sqrt{\epsilon_e} - Z_e\sqrt{\epsilon_o}}{2cZ_eZ_o} \quad (61)$$

where $Z_e, Z_o, \epsilon_e, \epsilon_o$ are the even and odd mode impedance and dielectric constants, respectively, and c is the speed of light in a vacuum. If one wishes to avoid coupling between nearby lines they should ensure $L_m \approx 0$ and $C_m \approx 0$. By this approach one can determine at what conductor separation coupling begins to become appreciable.

In simple circuits with a high level of symmetry it is possible to theoretically calculate these values, assuming expressions exist to describe one's transmission medium, but for most cases it is most convenient to extract these parameters from an electromagnetic simulator.

How to model coupling in a circuit model

Since the structures that I would like to model include thousands or tens of thousands of stubs, performing an electromagnetic simulation on the full device is impossible. Even simulating a meaningful portion of the device takes days, even with a powerful computer. Furthermore, drawing a circuit geometry in an electromagnetic simulator and pressing "start simulation" may provide useful information about the behavior of that exact geometry, but it does not provide an understanding about why it behaves that way, and how it can be changed to improve performance. A superior approach is to understand the circuit well enough to be able to describe it using simple elements which can provide an intuition of its behavior, which will guide the design process in a more powerful way—yielding better results in less time. Therefore much effort was made to find an approach to simplify the circuit.

While coupled lines have been extensively investigated and characterized, there are factors in this design that do not align with the extant body of coupled line research. First are the geometries which are well suited to this use case and fabrication process. The design in question uses a very thin film and a thick microstrip dielectric (relative to the line widths), whereas more traditional microstrip fabrication processes use thicker metal layers and a thin layer of deposited dielectric. So any models considered must be tested for accuracy in this unusual geometric regime. Second is the fact that while arbitrarily large arrays of coupled conductors have been studied previously, their particular geometry of interest varies from mine, e.g. an array of interdigitated stubs. Therefore my case requires some adaptation of the general theory. Some references describing this general case include [46, 51] and I will derive a solution specific to my coupling structure.

Just as a system of two coupled conductors can be described using the Telegrapher's equations,

$$\frac{\partial}{\partial x} \begin{bmatrix} V_1 \\ V_2 \end{bmatrix} = - \begin{bmatrix} L_s & L_m \\ L_m & L_s \end{bmatrix} \frac{\partial}{\partial t} \begin{bmatrix} I_1 \\ I_2 \end{bmatrix} \quad (62)$$

$$\frac{\partial}{\partial x} \begin{bmatrix} I_1 \\ I_2 \end{bmatrix} = - \begin{bmatrix} C_s & C_m \\ C_m & C_s \end{bmatrix} \frac{\partial}{\partial t} \begin{bmatrix} V_1 \\ V_2 \end{bmatrix} \quad (63)$$

these vectors and coupling matrices can be easily extended to model a general scenario of N coupled conductors. Let's define an inductance matrix $[L]$ which includes the self- and mutual inductances of all conductors in the system as

$$[L] = \begin{bmatrix} L_{11} & L_{12} & \cdots & L_{1N} \\ L_{12} & L_{22} & \cdots & L_{2N} \\ \vdots & \vdots & \ddots & \vdots \\ L_{1N} & L_{2N} & \cdots & L_{NN} \end{bmatrix} \quad (64)$$

which reflects the fact that there is symmetry between each coupled line, $L_{mn} = L_{nm}$. Note that every L_{mm} is the self-inductance of conductor m and L_{mn} refers to the mutual inductance between conductors m and n . Similarly, we propose a capacitance matrix,

$$[C] = \begin{bmatrix} C_{11} & C_{12} & \cdots & C_{1N} \\ C_{12} & C_{22} & \cdots & C_{2N} \\ \vdots & \vdots & \ddots & \vdots \\ C_{1N} & C_{2N} & \cdots & C_{NN} \end{bmatrix} \quad (65)$$

Now rewriting the Telegraphers equations for a system of N conductors,

$$\frac{\partial}{\partial x} \begin{bmatrix} V_1 \\ \vdots \\ V_N \end{bmatrix} = -[L] \frac{\partial}{\partial t} \begin{bmatrix} I_1 \\ \vdots \\ I_N \end{bmatrix} \quad (66)$$

$$\frac{\partial}{\partial x} \begin{bmatrix} I_1 \\ \vdots \\ I_N \end{bmatrix} = -[C] \frac{\partial}{\partial t} \begin{bmatrix} V_1 \\ \vdots \\ V_N \end{bmatrix} \quad (67)$$

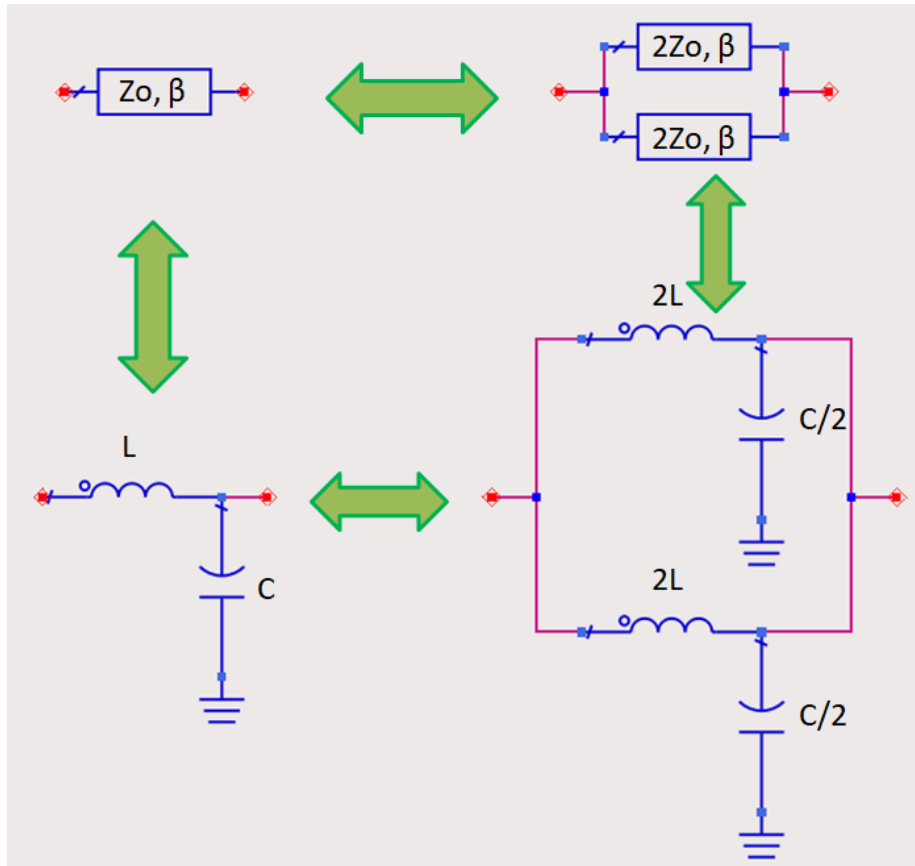
This is the idea behind and the commencement of the analysis of a matrix theory of coupled transmission lines. The full derivation, including direction on calculating $[L]$ and $[C]$, can be found in [46-48, 51-53]. I will now discuss techniques for simplifying the problem of an infinite array of coupling elements.

Note that with N parallel conductors in a planar orientation, the coupling will necessarily be largest with the nearest neighbor, significantly reduced with the next nearest neighbor, and so on until the coupling becomes negligible. This is due not only to the fact that the nonadjacent stubs are further away and the fields are weaker, but the interposing conductors will have a screening effect on the field lines that will reduce the magnitude even further. Therefore these coupling matrices will be effectively sparse, with the magnitudes concentrated in and around the central diagonal.

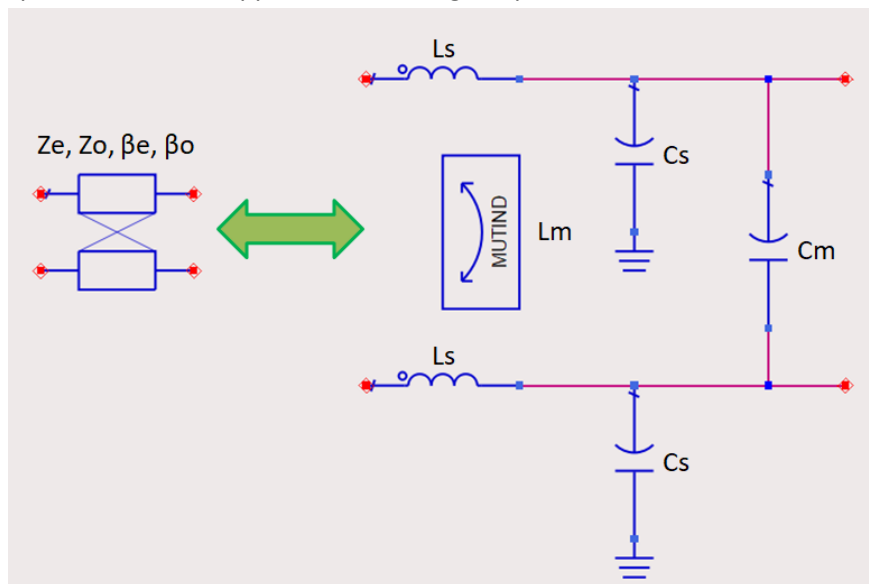
Given a transmission line with periodic bilateral shunt open-circuit stubs, there is a high level of symmetry which can be exploited. If one were to describe the stubs as a network with a coupling matrix, it would be a sparse matrix concentrated in and around the central diagonal.

There are several publications which propose a theory in which a network of N coupled lines could be modeled with using only coupled line pairs [54, 55]. This would be convenient as models for coupled line pairs are available in all major circuit simulators, but this technique makes a significant

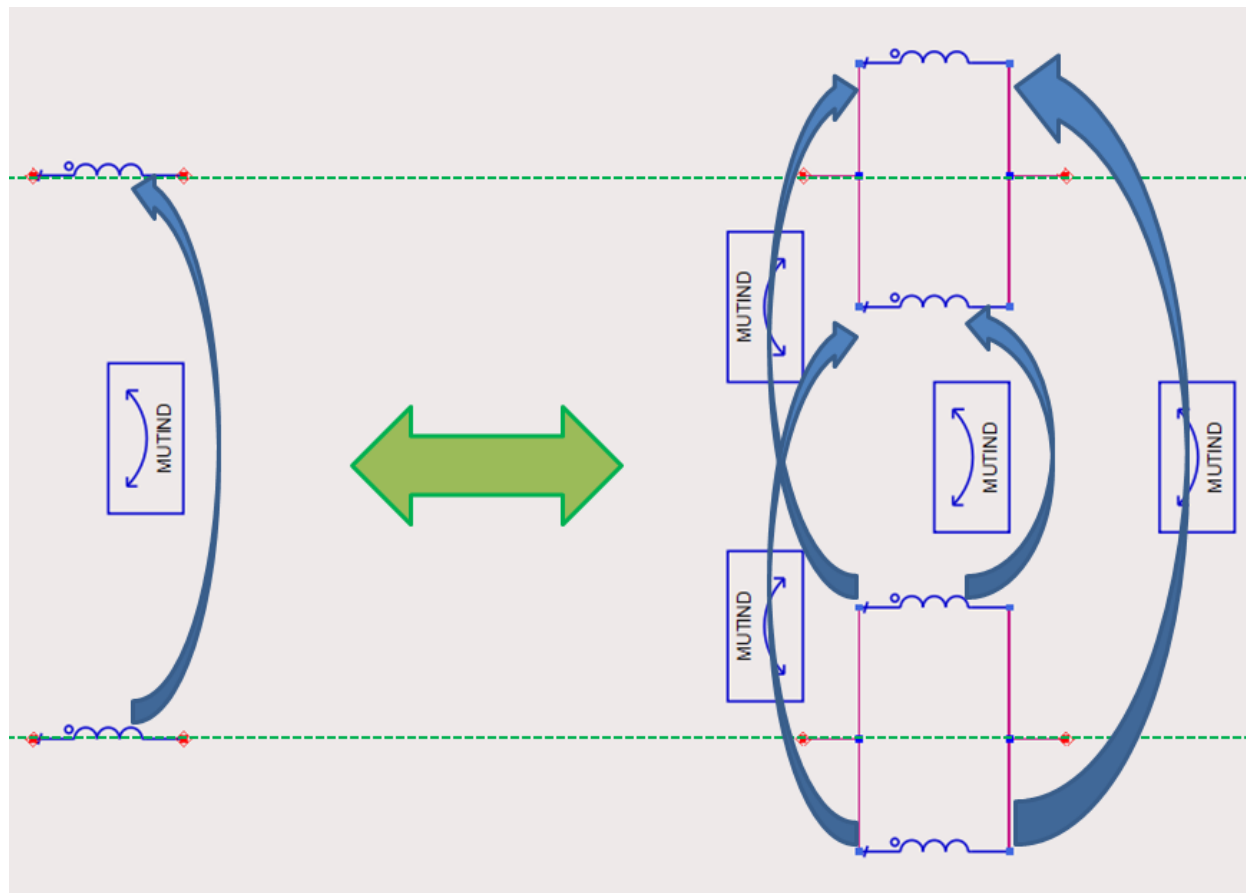
assumption—neglecting the mutual inductance—which reduces its accuracy. This is done by dividing every coupled transmission line in half, coupling each half with the nearest neighbor on either side, and then reconnecting each divided transmission line at either end. It is true that a simple transmission line and its lumped element approximation can be divided in half, as proposed by the authors,



and a pair of coupled lines can be approximated using lumped elements like so:

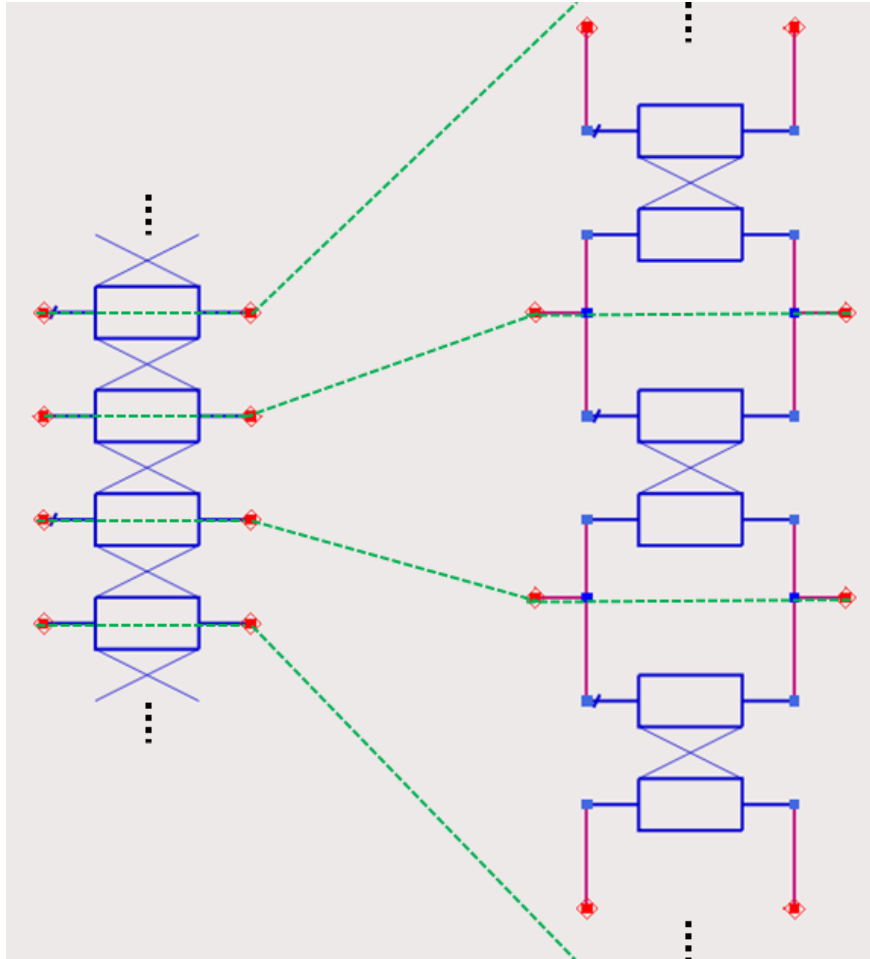


The weakness of this technique is that it does not take into account the mutual inductance between the coupled lines and thus its accuracy is limited. And unfortunately the inclusion of the mutual inductance causes this technique to break down as the coupling distributes to each divided element:

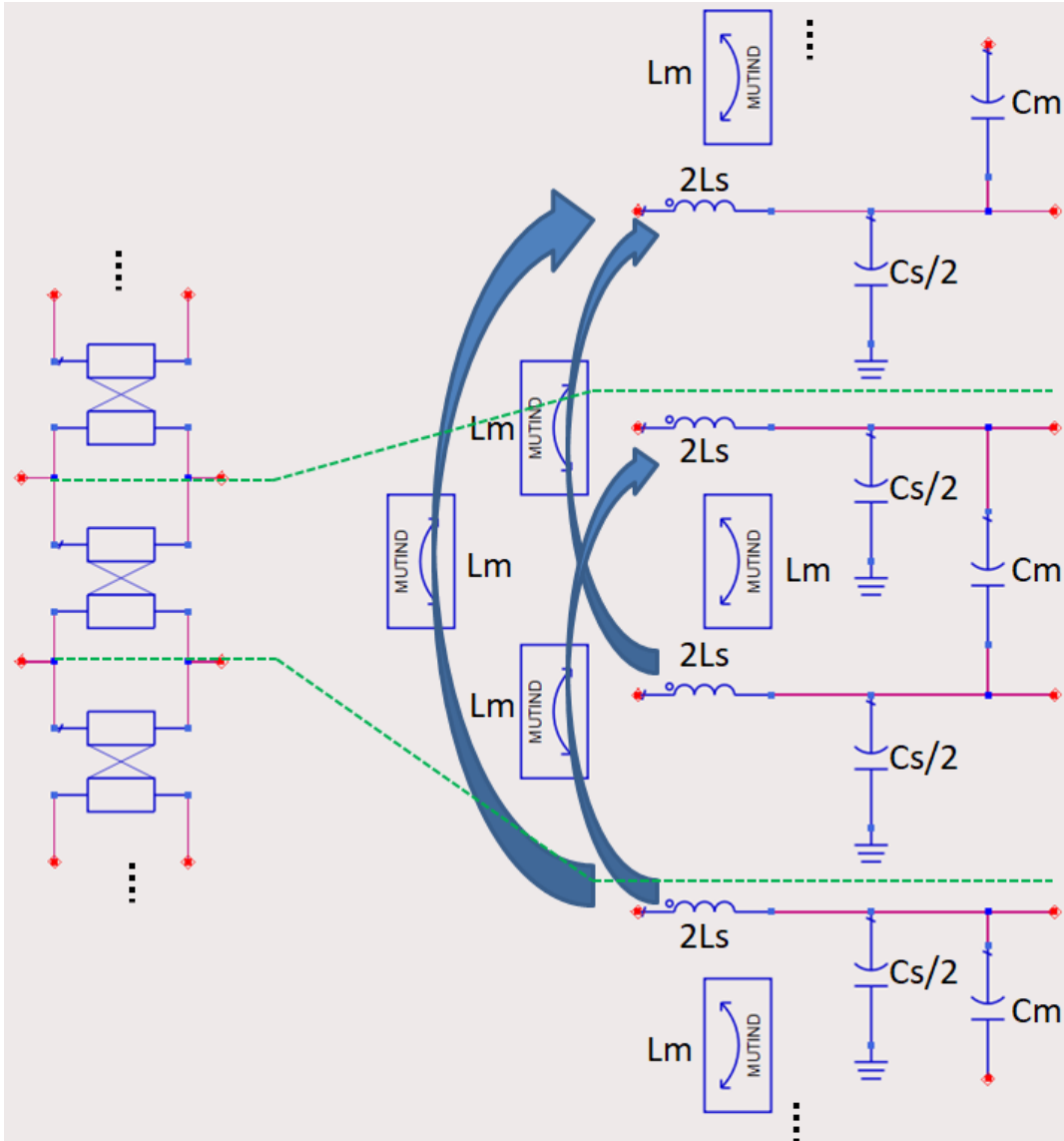


This causes an array of coupled lines to no longer be separable into isolated unit cells as each half of each line maintains a coupling to the other half.

In review, the goal is to be able to model an array of coupled lines (left) with simple pairs of coupled lines (right). This involves attempting to divide each coupled conductor into two, as shown



The self-capacitance, mutual capacitance and self-inductance can be divided cleanly, but the mutual inductance will be bound to the inductors which have been divided into the adjoining cells, making it impossible to separate them into simple pairs of coupled lines.



Therefore this simplification technique has fundamental limitations on its accuracy.

Normally when dealing with periodic structures, one analyzes a single period, where the unit length can then be cascaded to the length desired. However in cases involving coupling this is not so straightforward. As was highlighted in the previous example, separating a periodic unit into simple cells can preserve the coupling within that cell, but will sever coupling between cells. I propose a novel technique which can be satisfactorily used to simplify periodic coupled structures, using as an example a transmission line periodically loaded with bilateral open-circuit stubs, such as shown in Figure 30.

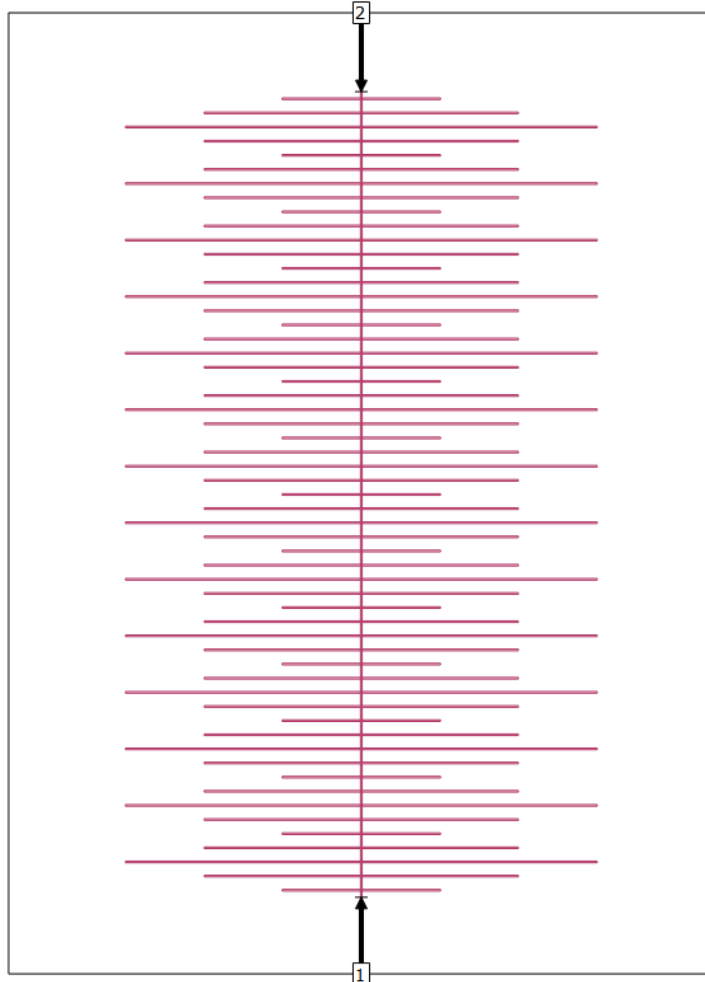


Figure 30: a periodically loaded transmission line

Note how there is a periodicity of four stubs which repeats many times. One could define a “unit cell” to be as shown in Figure 31.

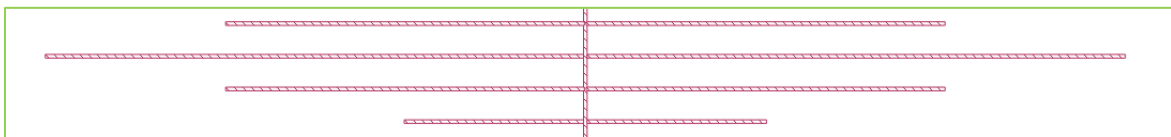


Figure 31: A unit cell of the full line above

However, one must not make the mistake of characterizing this unit cell and cascading it, as shown in Figure 32 with the green lines.

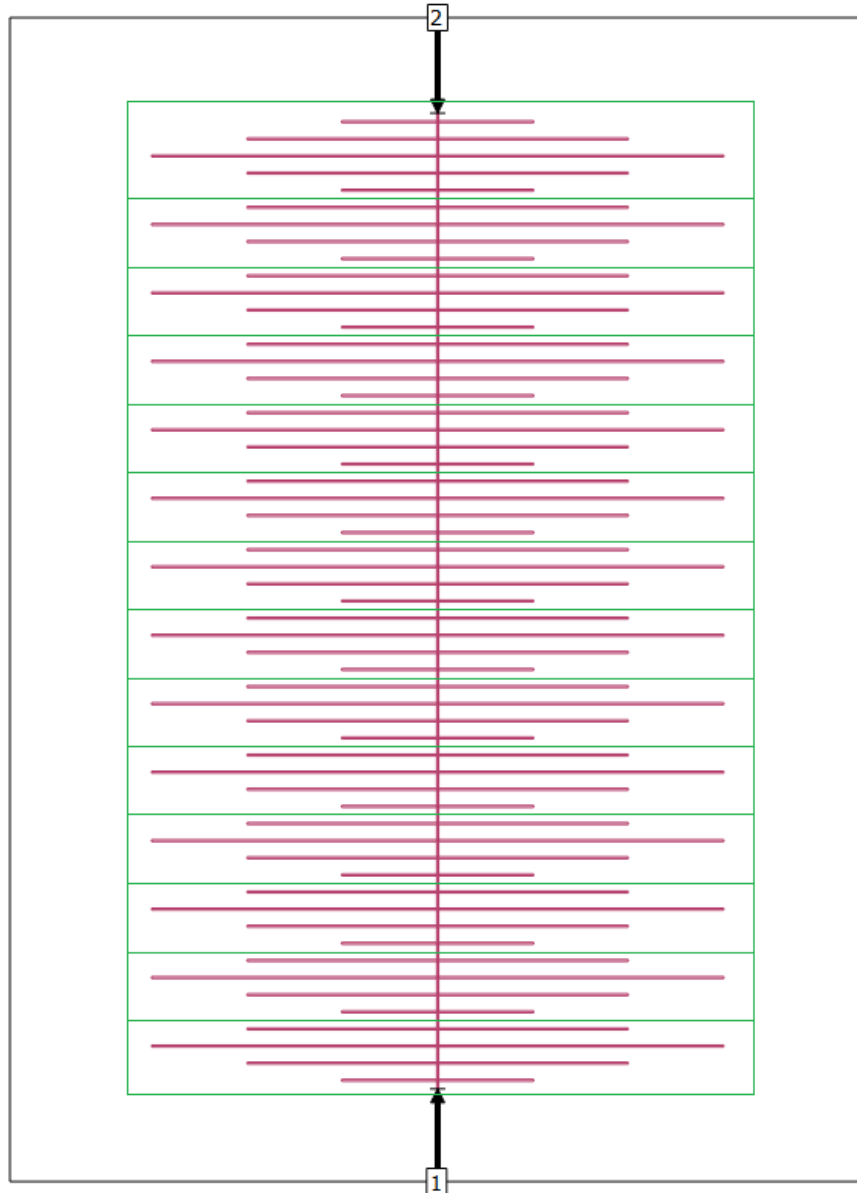


Figure 32: A periodic coupled structure broken into unit cells shown in green outlines

This is invalid because the coupling between the stubs in neighboring cells (across the green lines) will be lost. However it is possible to extract the periodic coupling and replicate it in a faithful way, enabling arbitrarily long coupled structures. One can characterize the stubs and their mutual coupling by simulating them separately, as shown in Figure 33.

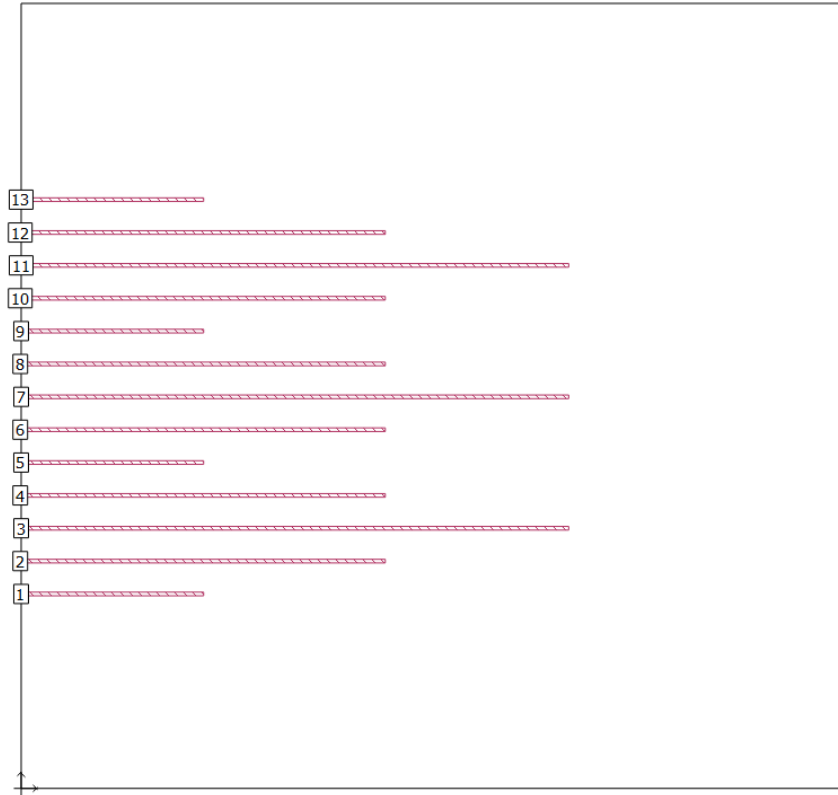


Figure 33: Simulating the stubs alone allows one to extract the coupling matrix and extend it arbitrarily.

One must not simulate a single periodic cell (e.g. stubs 5-8 in Figure 33), as this would lack the influence of the stubs around it. Note that the first and last few stubs in an arbitrarily long series will not have coupling on one side, and without that coupled loading will exhibit a distinct behavior (an “end effect”) from the stubs deep inside the array. This latter behavior can be labeled the “bulk effect”. This can be seen visually in Figure 34.

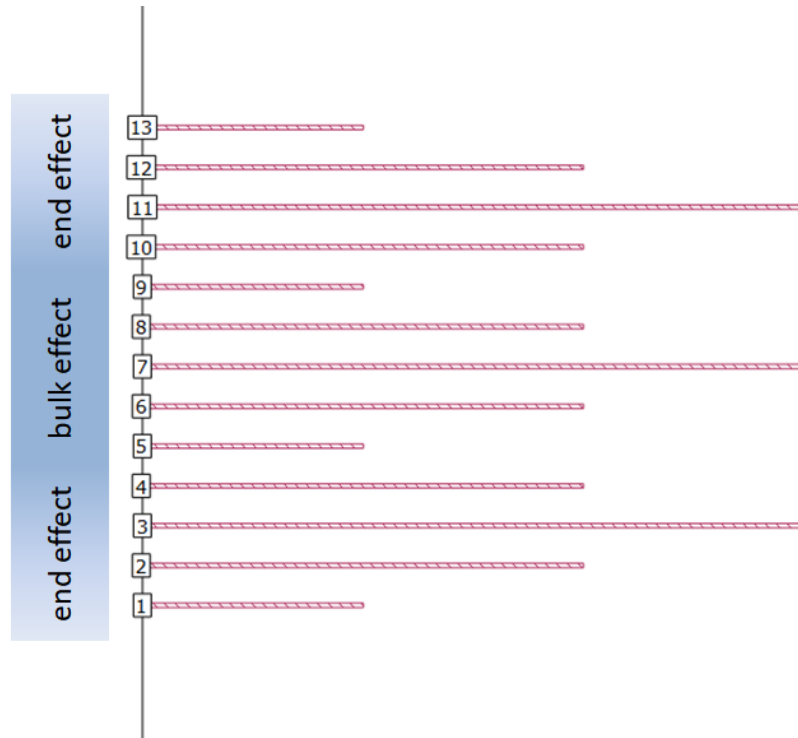


Figure 34: The intensity of coupling portrayed with a color gradient.

The number of stubs on the end which will experience an end effect will vary from one implementation to another, depending on the magnitude of the coupling between stubs. This is primarily a function of stub separation, distance to the ground conductor, and effective dielectric constant. As a rule of thumb, one can consider the end effect to affect the same number of stubs as the number of nearest neighbors' coupling to each stub which are included in a simulation—if a designer is content with only considering the two nearest neighbors in the coupling of each stub, then the end effect will only be relevant in the last two stubs on either end of the series.

After being modeled in this fashion, the stubs can be re-assembled into a stub-loaded line by stitching them together using short crosses, whose length is equal to that of a single stub unit cell. Figure 35 shows an example of such a cross, with feedlines and de-embedding to prevent coupling to other ports or box walls.

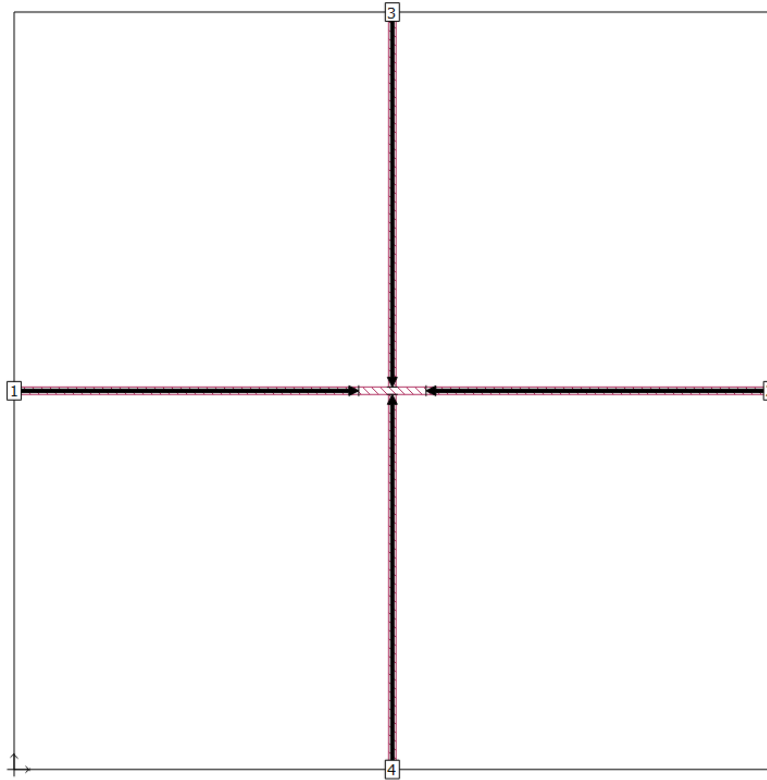


Figure 35: A short cross for stitching stubs together.

Then N crosses are cascaded, where N is the number of stubs in the design, and a copy of the simulated stubs is placed on either side, with each stub port on one side connecting to all the cross port 3's, and each stub port on the other side connecting to all the cross port 4's, as shown in Figure 36.

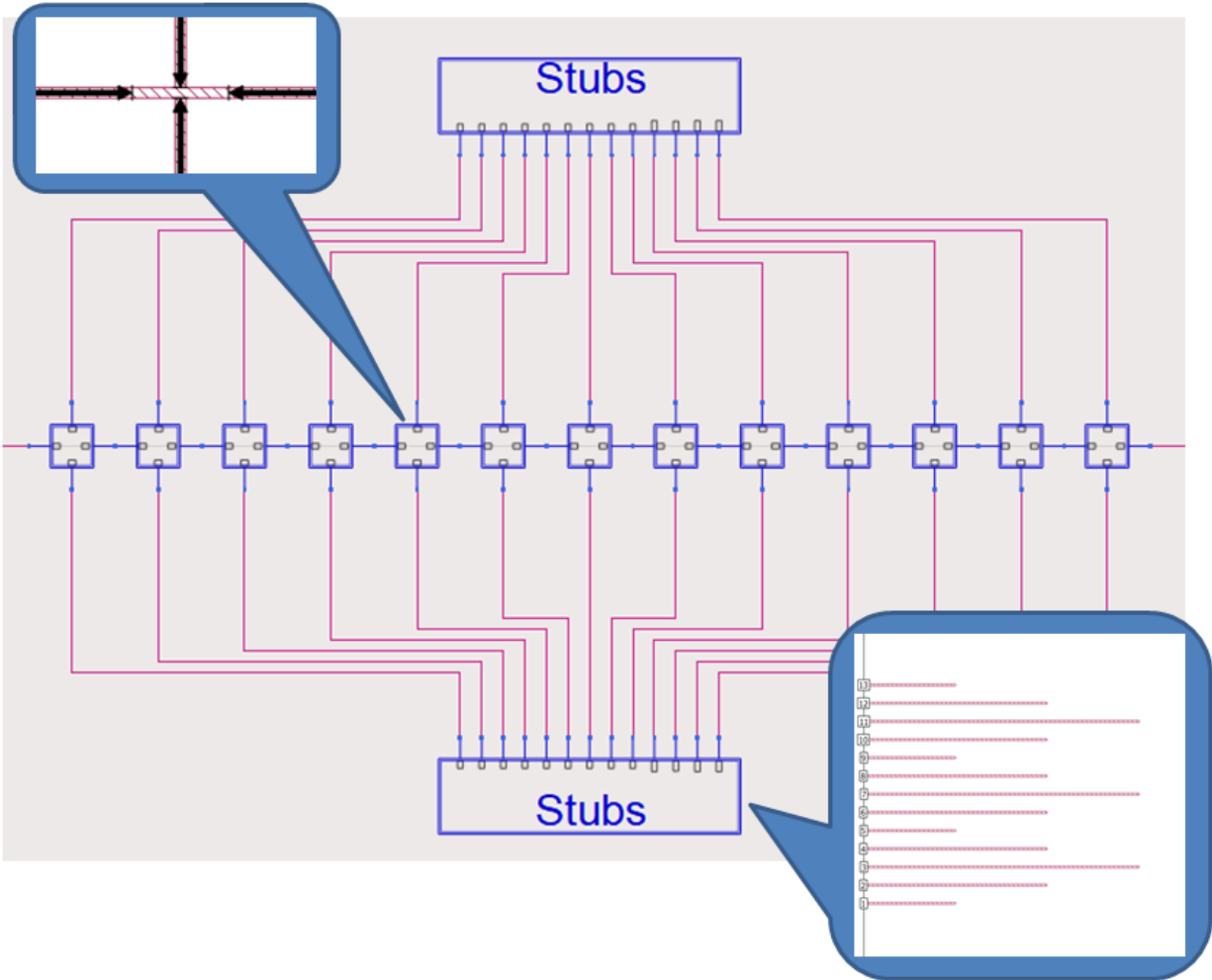


Figure 36: A bilateral stub-loaded line stitched together in a circuit simulator.

This circuit is simply an example to demonstrate the concept—as the number of stubs increases the schematic quickly becomes unwieldy. The next innovation is to take the S-matrix of the coupled stubs and programmatically extend it to the desired number of stubs, limited only by one’s computing resources. This is done by the following steps:

1. Insert additional matrix anti-diagonals in the S-matrix until it reaches the desired number of stubs, N . In other words, one is increasing the size of the S-matrix but adding the extra elements in the center instead of at one end. This is because it is important to keep the “end effect” stubs at the ends.
2. Identify one periodic cell of stubs within the bulk effect section as P stubs beginning at stub M , and choose the desired number of nearest neighbors Q to include in the simulation.
3. Copy $S_{m,m-Q}, S_{m,m-Q+1}, \dots, S_{m,m+Q}$ to $S_{m+P,m+P-Q}, S_{m+P,m+P-Q+1}, \dots, S_{m+P,m+P+Q}$ for $m = M$ to $M+P-1$
4. Repeat the previous step R times, where R is the number of periodic cells needed to complete the N desired stubs.

This produces an $N \times N$ S-matrix of one side of stubs. This is called the extended stub matrix. Then a designer must stitch an extended stub matrix on each side of a cascade of crosses as discussed

previously. This can be done using the subnetwork growth technique [56], for example using Python’s scikit-rf [57].

To consider a more visual approach, the simulation will yield a matrix of S-parameters. For the same of simplicity, consider that the stubs are a constant length, as shown in Figure 37.

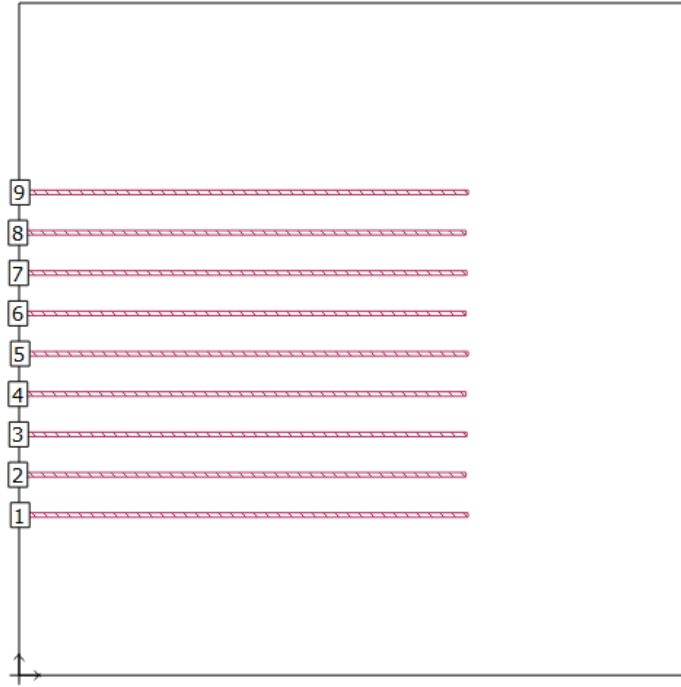


Figure 37: A simpler stub simulation with constant stub lengths

This will yield a 9x9 S-matrix with significant redundancy. S_{44} will be identical to S_{55} , and similar to S_{11} , but S_{11} will have the “end effect”. In the same fashion, S_{45} (which indicates the coupling between stubs 4 and 5) will be identical to S_{54} and S_{56} and similar to S_{12} , which will include the “end effect”. Therefore we could simplify this matrix in a more general form:

$$\begin{pmatrix} S_{11} & S_{12} & \cdots & S_{19} \\ S_{21} & S_{22} & \cdots & S_{29} \\ \vdots & \vdots & \ddots & \vdots \\ S_{91} & S_{92} & \cdots & S_{99} \end{pmatrix}$$

is approximately equal to

$$\begin{pmatrix} a_{e2} & b_{e2} & c_{e2} & 0 & 0 & 0 & 0 & 0 & 0 \\ b_{e2} & a_{e1} & b_{e1} & c_{e1} & 0 & 0 & 0 & 0 & 0 \\ c_{e2} & b_{e1} & a & b & c & 0 & 0 & 0 & 0 \\ 0 & c_{e1} & b & a & b & c & 0 & 0 & 0 \\ 0 & 0 & c & b & a & b & c & 0 & 0 \\ 0 & 0 & 0 & c & b & a & b & c_{e1} & 0 \\ 0 & 0 & 0 & 0 & c & b & a & b_{e1} & c_{e2} \\ 0 & 0 & 0 & 0 & 0 & c_{e1} & b_{e1} & a_{e1} & b_{e2} \\ 0 & 0 & 0 & 0 & 0 & 0 & c_{e2} & b_{e2} & a_{e2} \end{pmatrix} \quad (68)$$

assuming that the coupling is limited to the two nearest neighbors so that S_{14} to $S_{19} = 0$, etc. The e1 and e2 subscripts refer to an outer edge stub (e2) and an inner stub that is still in the “edge effect” area (e1). Now it becomes more obvious that redundancy allows the bottom right triangle to be pushed out, and

the vacancies can be supplied by copying the center row of (69) to the next rows down and shifting it appropriately to create the size of matrix (number of stubs) desired. The concept is the same when the stubs are not the same length and vary periodically, but instead of copying only one middle row, P rows must be copied and shifted at a time.

To provide a concrete example, we can use the stub set shown in Figure 34. Note how stubs 5-8 form a periodic cell of stubs. Say one desired to extend this to have 10 periodic cells total, or 41 stubs total. This means that $N=41$, $M=5$, $P=4$, and $R=7$ to extend the three initial periodic cells to ten. Suppose the designer wished to include the coupling of the two nearest neighbors, or $Q=2$. Then generate a 41×41 complex extended stub matrix and copy the upper left triangle of the 13×13 initial stub S-matrix into the upper left of the extended stub matrix, and the lower right triangle of the initial stub matrix into the lower left of the extended stub matrix. Then copy stub 5's parameters ($S_{5,3}, S_{5,4}, \dots, S_{5,7}$) to stub 9's row ($S_{9,7}, S_{9,8}, \dots, S_{9,11}$). Repeat with stub 6's parameters to stub 10's row, and so forth, until the extended stub matrix is fully populated. Be careful to not overwrite the data of the end-effect stubs.

To demonstrate the validity of this algorithm, first a full structure of 14 periodic cells was simulated in Sonnet, as shown in Figure 32. Then to prove the stitching technique all 57 stubs were simulated in Sonnet as shown in Figure 38, then imported into Keysight Advanced Design System (ADS) where they were connected using many copies of the cross shown in Figure 35. This schematic is shown in Figure 39.

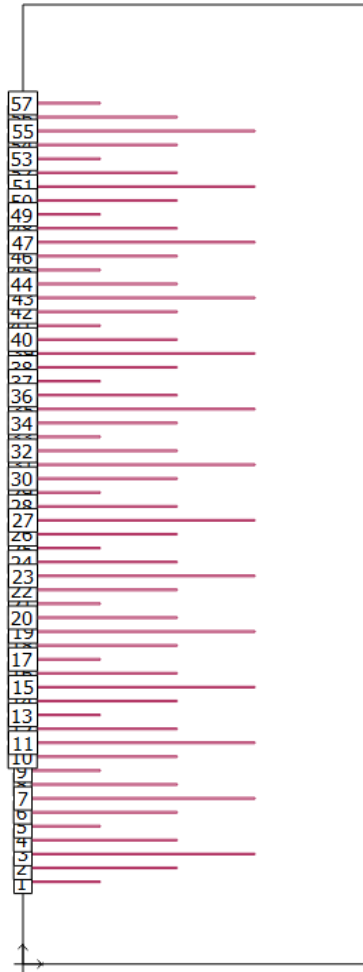


Figure 38: A full set of stubs to prove the stitching technique.

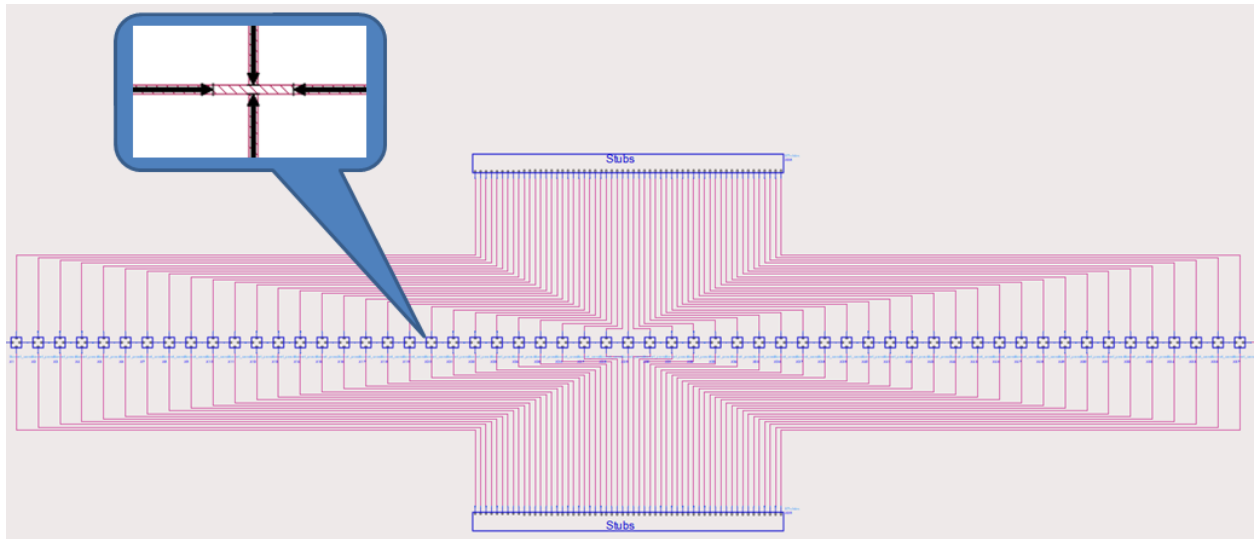


Figure 39: The full ADS circuit to test the stitching technique.

And to prove the matrix extension technique, a subset of stubs such as shown in Figure 33 was simulated and extended in Python's scikit-rf to include the full 57 stubs, then was stitched together in Python. The results are shown in Figure 40.

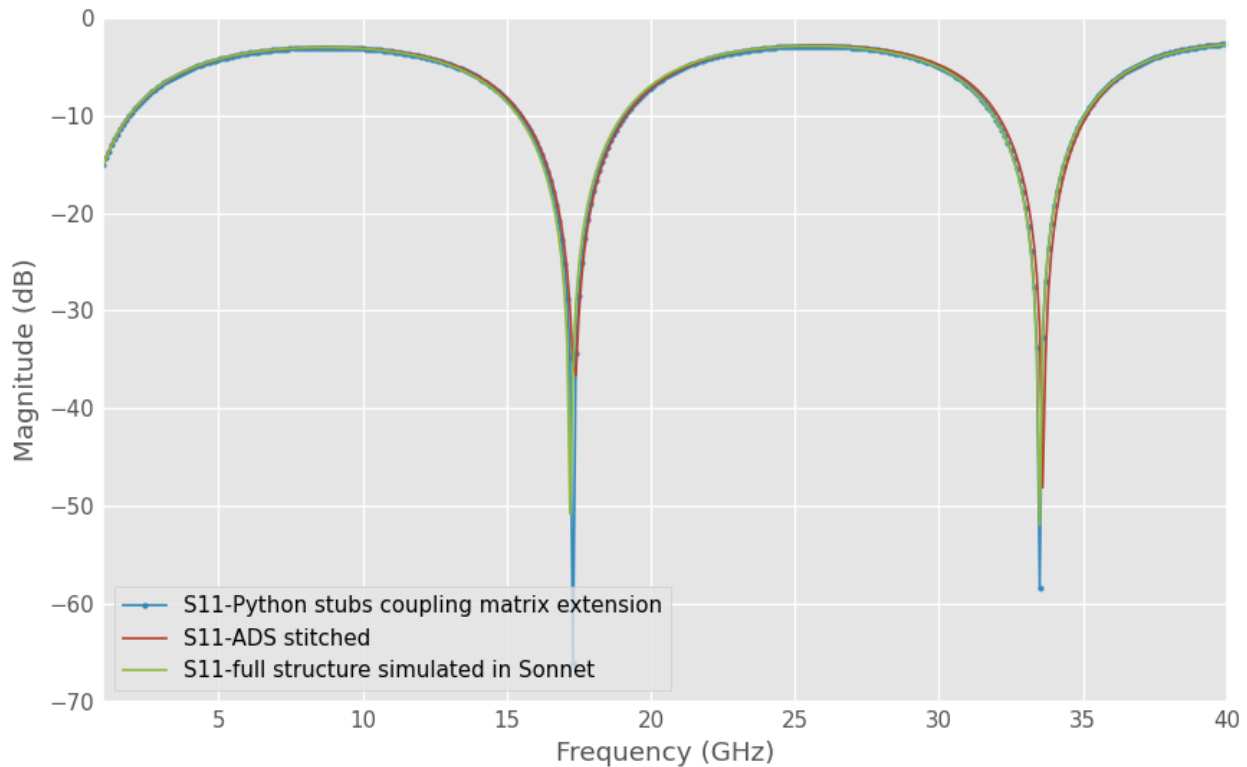


Figure 40: The ADS circuit stitching and Python scikit-rf matrix extension techniques produced the same response as the simulation of the full circuit in Sonnet.

There are minor discrepancies which do not exceed an error magnitude of 2%. This is due to the small variability inherent in Sonnet's de-embedding algorithm and is not introduced by the simplification techniques discussed here. If $1e9$ stubs were produced via matrix extension and $1e9$ stubs could be modeled in Sonnet, the static error of 1-2% would still be present. The error does not scale with the size of the simulation, and is present even in a simulation of a single stub. Therefore these simplification techniques are valid and accurate.

Proposed Designs

Different designs will now be compared. They are designed to operate with a pump frequency of approximately 10 GHz due to the available of microwave equipment in this band, but can be scaled to any desired frequency range up to the bandgap frequency as discussed in the section Kinetic Inductance.

Design 1: A stub-loaded line without coupling

This design spaces out the stubs sufficiently to minimize coupling. This is advantageous for using a simpler model that is more proven and less computationally expensive. This design uses a 20mm long line with a line width of 2um, with 2um wide stubs separated by 50um, with stub lengths varying from 240um to 280um across a period which is 10 stubs long. It provides 14.5dB of gain with a -3dB

bandwidth of about 5.5 GHz. Note that a stub-loaded line with coupling was also investigated, however it did not provide an advantage at these geometries.

Design 2: A line without stubs

In an attempt to provide a more equitable comparison, we will allow this line to be somewhat longer, since it is easily meandered (which stands in stark contrast to the near impossibility of meandering a stubbed line). Estimating that within the same wafer area this line could be meandered three times, this line is 60mm long. The nominal line width is 2um and is periodically widened abruptly to 30um. It has a peak gain of around 6.3dB and a 3dB bandwidth of around 14 GHz. It is able to be wider because with a lower gain the rolloff is slower. For an equitable comparison of bandwidth, if the line were 97mm long instead, the peak gain would be 14.6dB (similar to above) with a 3dB bandwidth of 10.1GHz. So the gain profile does tend to have more bandwidth with a stepped impedance line.

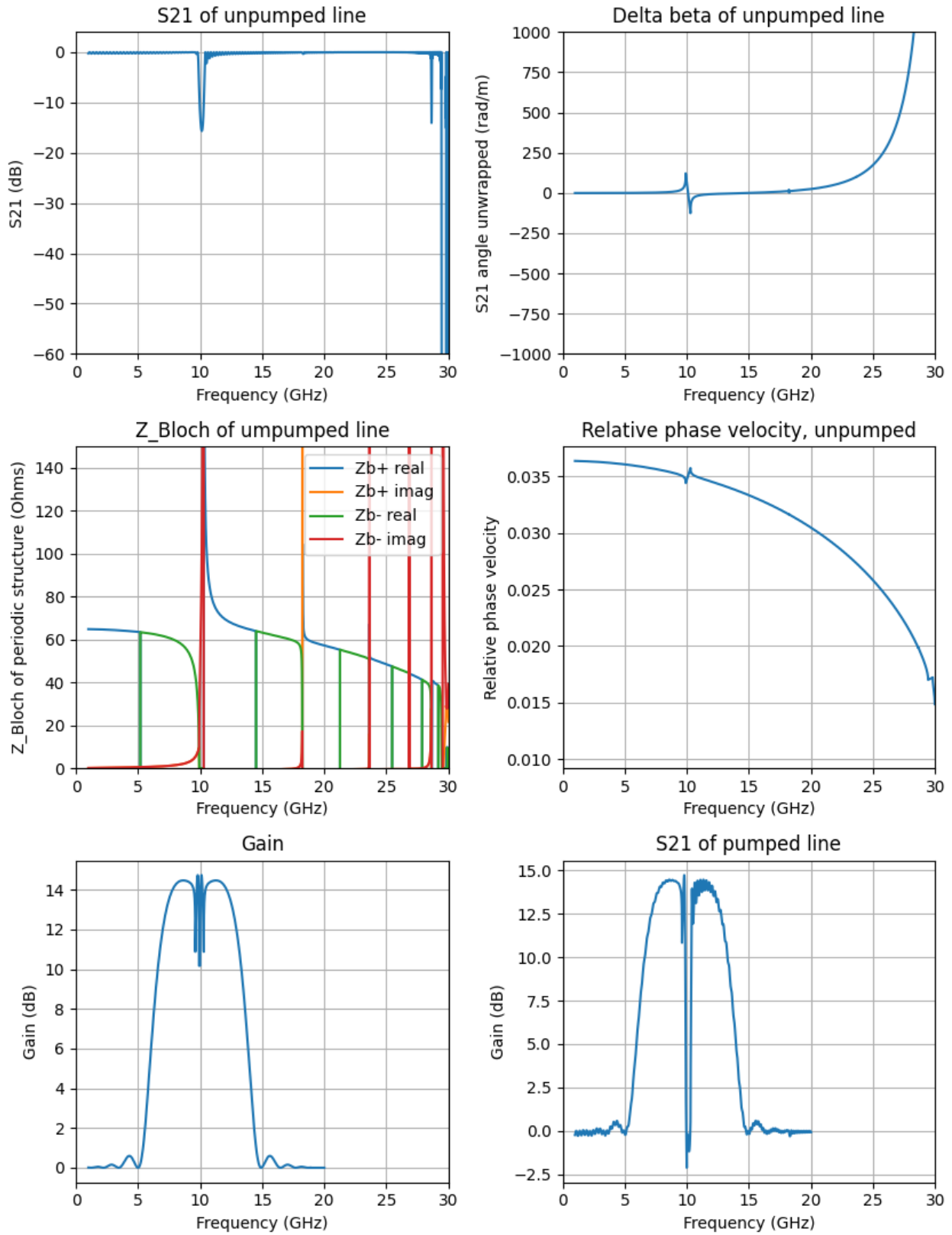


Figure 41: TKIP design using stubs, but with sufficient separation to avoid coupling

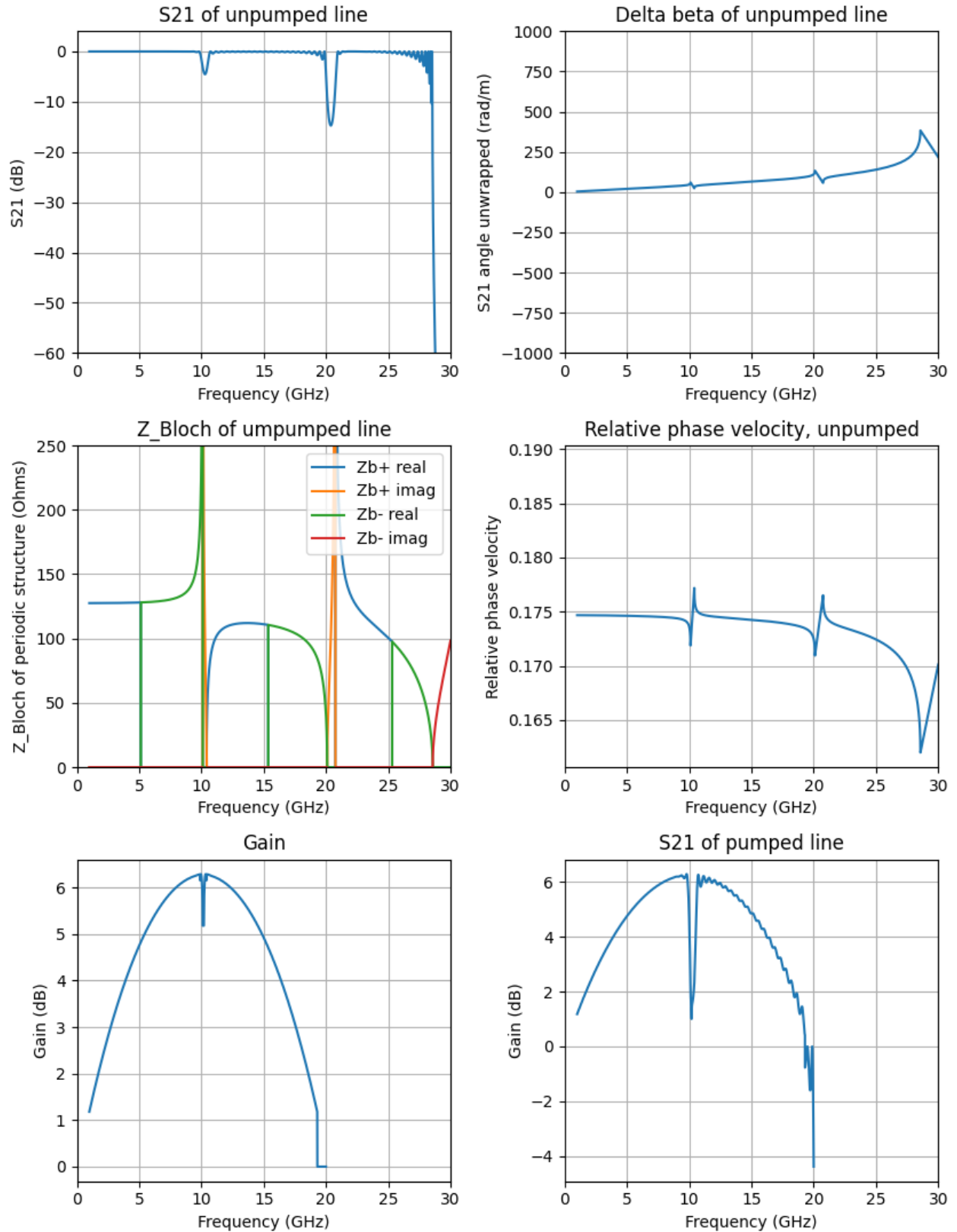


Figure 42: A TKIP design using a long, meandered line with periodic impedance perturbations.

Chapter 4: Cryogenic Systems

Superconducting circuits require the complexity and overhead of a cryogenic system. There are many considerations relating to a cryogenic system that must be understood in order to appreciate the design of a test setup.

Thermal Considerations

In a cryogenic system great attention must be given to the thermal load on the cryostat or else the system will not be able to reach its base temperature. As a first step, a vacuum pump is used to evacuate the air from the cryostat to reduce convective thermalization, which is where the air particles will transfer energy from a hotter surface to a colder one as they bounce around inside the cryostat. Also a metal connection, whether simple wires, coaxial cable, or rigid waveguide, between the cold stage and the room-temperature exterior would be a direct thermal path and would add a significant heat load to the cooling system. The impact of these connections is normally reduced with various techniques:

1. Thermal sinking. Any connection to the exterior of the cryostat (e.g. a wire) needs to have a thermal connection to every cold stage it passes. Cryostats are designed with multiple thermal stages where the warmer stages have more cooling power. This is similar to the different gears in an automobile's transmission, where the lower gears have more torque. For example, a simple cryostat might have a "first stage" which cools to ~80 Kelvin, and a "second stage" or "cold stage" which cools to ~4 Kelvin. Any connections going from the cryostat exterior to the 4K stage should be connected thermally to the 80K stage first. Note that usually this thermal connection does not include an electrical connection, except in the case when one wishes to connect a ground wire to the cryostat's electrical ground circuit. Whenever attempting to make a connection between two larger areas, e.g. bolting a plate to a cold stage, it is favorable to apply thermal grease (e.g. Apiezon N-grease). Otherwise there will be narrow voids in between the two imperfectly flat planes where no thermal conduction will take place. Thermal grease will help to fill in the voids and provide some thermal conductivity in these areas.
2. Longer wires. Using longer wires will effectively reduce that connection's thermal conductivity—i.e. reduce the thermal "current", or flow of phonons.
3. Thermal breaks. A thermal break is interposing a material or structure of lower thermal conductivity along the connection path, for example using a small section of stainless steel waveguide instead of a more typical material with higher electrical conductivity.
4. Special materials. Generally a material that has high electrical conductivity also exhibits high thermal conductivity. There are, however, atypical materials which have a significantly reduced thermal conductivity while still providing acceptable electrical conductivity. An example of this is Phosphor Bronze.

Noise Considerations

Electrical systems experience several different types of noise, described below are the most relevant to the present discussion:

1. Thermal noise or Johnson noise is due to the random motions of particles due to possessing thermal energy. Different scientific communities can treat thermal noise as either a noise

power or a noise temperature, but its reduction in a cryogenic system is the same in either case. The noise “power available” from thermal fluctuations is

$$P_{Planck} = kT \left[\frac{\frac{hf}{kT}}{\exp\left(\frac{hf}{kT}\right) - 1} \right]. \quad (69)$$

where k is Boltzmann’s constant, T is temperature, h is Planck’s constant and f is operating frequency. In typical applications, $hf \ll kT$ and thus it is common to use the Rayleigh-Jeans approximation of (69) which is

$$P_{R-J} = kTB \quad (70)$$

where B is the system bandwidth. However this approximation is not appropriate for cryogenic applications with a small T . “Power available”, while being the precise technical term, can seem odd because no net power can be collected from thermal fluctuations, or any other kind of noise.

2. Shot noise is a result of the random arrival time of discrete charge carriers to a discrete transition, for example when charge carriers cross a potential barrier, such as a PN junction. Since the present circuits do not include any discrete transitions this noise source is absent. This is the major advantage of superconducting amplifiers over even the lowest noise conventional transistor amplifiers. The root-mean-square value for the shot noise current is

$$i_n = \sqrt{2IqB} \quad (71)$$

where I is the DC current and q is the charge of an electron.

3. Flicker noise or $1/f$ noise is understood to be caused by variations in resistance in a material, which causes random fluctuations in voltage or current. This phenomenon has a larger effect at lower frequencies (see Figure 43), hence the common name of “ $1/f$ ” noise. Since this is caused by a material’s resistance, this type of noise is not present in a superconductor which does not exhibit electrical resistance.

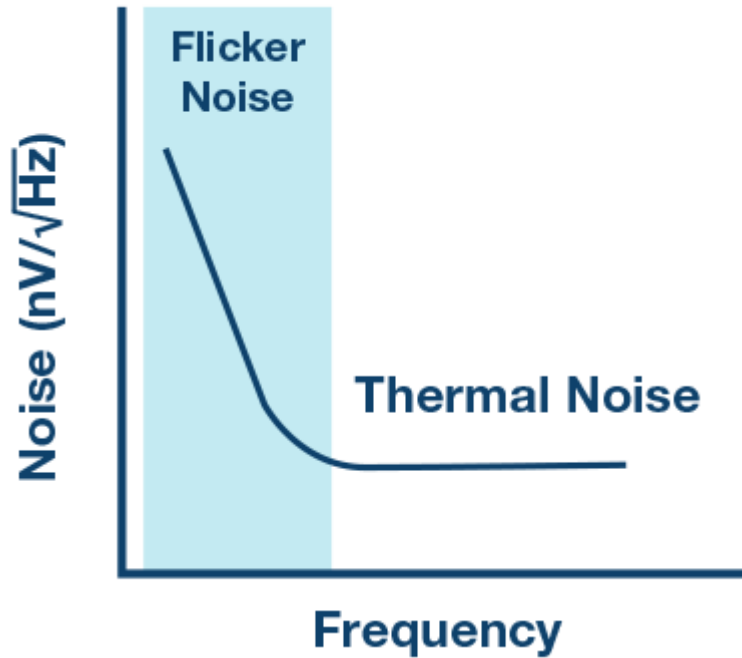


Figure 43: Graph showing the qualitative effects of flicker and thermal noise. Copied from [58].

4. Vacuum fluctuations are produced by random variations in the quantum mechanical vacuum in the creation and destruction of particles and anti-particles [59]. Their magnitude is so small that they are usually not only neglected outside of cryogenic and optics applications but not even mentioned. The power available from vacuum fluctuations is

$$P_{vac} = \frac{hf}{2} \quad (72)$$

Noise in cryogenic systems

As mentioned above, in superconducting applications most sources of noise (including several more not mentioned here) are no longer present, and the two that are typically treated are thermal noise and vacuum fluctuations. To consider them simultaneously one may use the Callen-Welton equation for noise power [60], which is simply the sum of the two sources:

$$P_{C-W} = P_{Planck} + P_{vac} \quad (73)$$

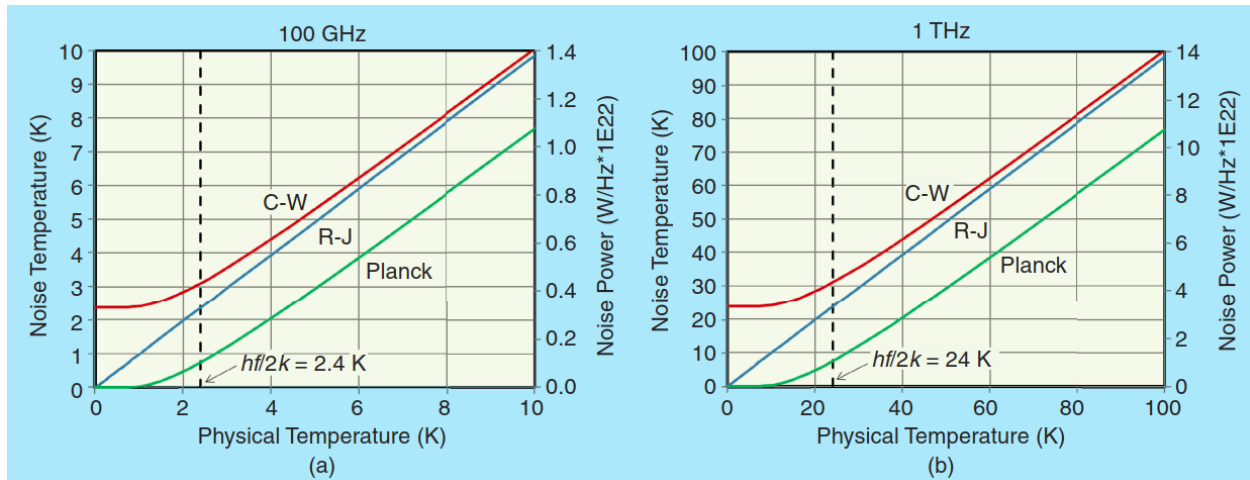


Figure 44: Graphs showing the relative levels of thermal and vacuum noise contributions and an inclination of how it scales with frequency. Planck includes only thermal noise, R-J is a simplified form of Planck, and C-W is Callen-Welton which includes thermal noise and vacuum fluctuations. Copied from [59].

It is clear then that cryogenic operation provides significant benefits in terms of the noise performance of a circuit. Regarding thermal noise (which is proportional to temperature), operating at cryogenic temperatures (e.g. 4 Kelvin) would produce 72.5 times less noise than operating at room temperature (290 Kelvin). One must be aware, though, that when sending in a signal from the outside of the cryostat, it will have room-temperature levels of noise, which alone can be of sufficient magnitude to saturate some cryogenic components like superconducting parametric amplifiers. The common solution to this problem is to generate a strong SNR outside of the cryostat then attenuate it at least one cold stage by 20+ dB to bring the signal and noise levels down to cryogenic levels. This attenuator often can also serve to thermally sink the center conductor of a coaxial waveguide medium.

Measuring Noise

Noise is commonly measured via the Y-factor method, which uses a device with a known high noise level (e.g. an avalanche diode), and the system's output power is measured with the noise source on and off, and the difference in the two system power outputs can be used to calculate the noise contributed by the system itself. Noise can be expressed in terms of noise figure, noise factor, noise temperature, and noise power. When using the Y-factor method it is most convenient to speak in terms of noise temperature. The Y-factor technique is described in part by this equation:

$$Y = \frac{T_s^{on} + T_{DUT}}{T_s^{off} + T_{DUT}} \quad (74)$$

where T_s^{on} is the noise temperature of the calibrated noise source when powered on and T_s^{off} is the physical temperature of the noise source. But if there is only one unknown (T_{DUT}), why are two measurements required? A single measurement would require precise knowledge of the gain (or loss) of the system (hidden in the Y variable above), but performing two measurements, in contrast, will yield that information. This concept can be captured intuitively in graphical form:

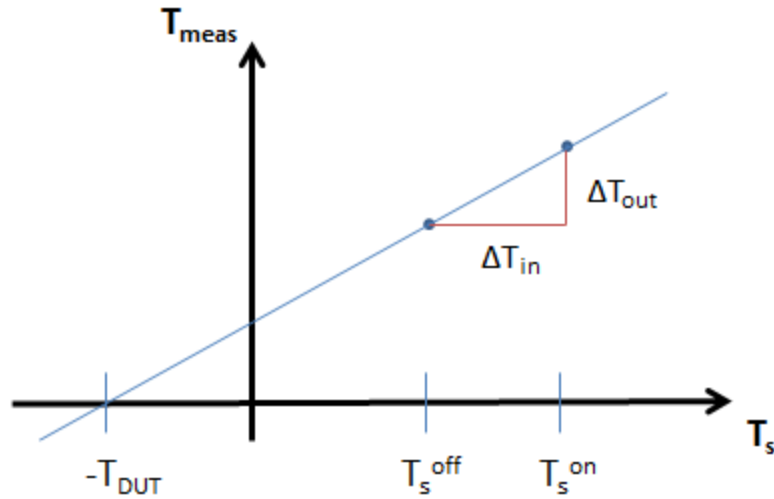


Figure 45: Graphical representation of the Y-factor measurement. The slope is the DUT gain and the x-intercept is the DUT's noise temperature.

The two measurements will yield two noise temperatures. When plotted, the two points will form a line whose x-intercept is the noise temperature of the DUT, and whose slope ($\Delta T_{out}/\Delta T_{in}$) is equal to the gain of the DUT. T_s^{on} is determined by the noise source and is provided by its manufacturer. It is expressed in terms of Excess Noise Ratio (ENR), an essential characteristic of a calibrated noise source:

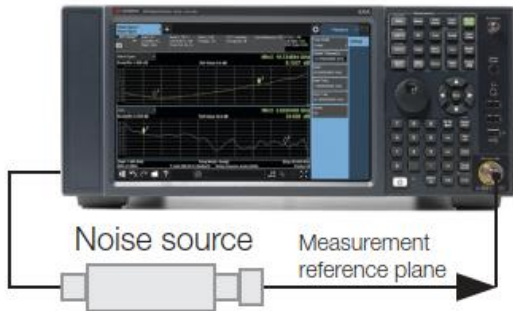
$$ENR = \frac{T_s^{on} - T_s^{off}}{T_0} \quad (75)$$

where T_0 is the reference temperature of 290 Kelvin. An accurate noise measurement will require T_s^{off} to be corrected for the actual noise source's physical temperature at the time of measurement.

For best results, a Y-factor measurement's T_s^{off} and T_s^{on} should be close to T_{DUT} . The further they are, the more one extrapolates from the data and reduces accuracy. Furthermore, T_s^{off} and T_s^{on} should not be too close together, otherwise the measurement is more vulnerable to any uncertainty or noise, which will magnify any error when extrapolating. A simple rule of thumb is for T_s^{on} to be at least ten times greater than T_s^{off} .

One additional consideration for precise noise measurements is that the measurement system must be calibrated to remove the noise and gain contributions of said system, as shown in Figure 46.

(a) calibration



(b) measurement

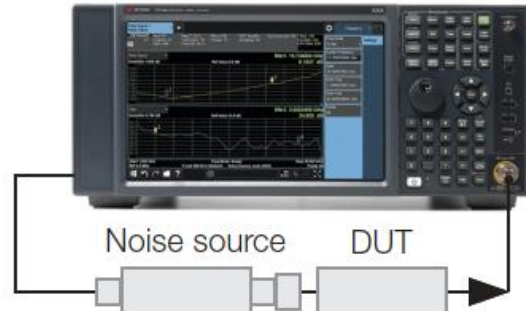


Figure 46: A noise measurement requires a calibration step first. Copied from [61].

The devices included in the calibration are called the “second stage”, even though this measurement comes first. It includes, at a minimum, the measurement device, but can include other devices, such as a preamplifier for boosting the SNR before a noisy measurement system. Performing this calibration and utilizing a preamplifier are especially important when measuring noise using a spectrum analyzer because they are designed for high dynamic range, not for low noise operation, and their noise contribution can be tens of dB in magnitude [61].

The calculation for this preliminary step is that already mentioned above in equation (40), but replacing T_{DUT} with T_{stage2} or simply T_2 :

$$Y_2 = \frac{T_s^{on} + T_2}{T_s^{off} + T_2} \quad (76)$$

The equations for calculating the de-embedded DUT noise and gain contributions then become those of a cascaded system, as shown in Figure 47 where the “first stage” is the DUT and any devices necessarily included.

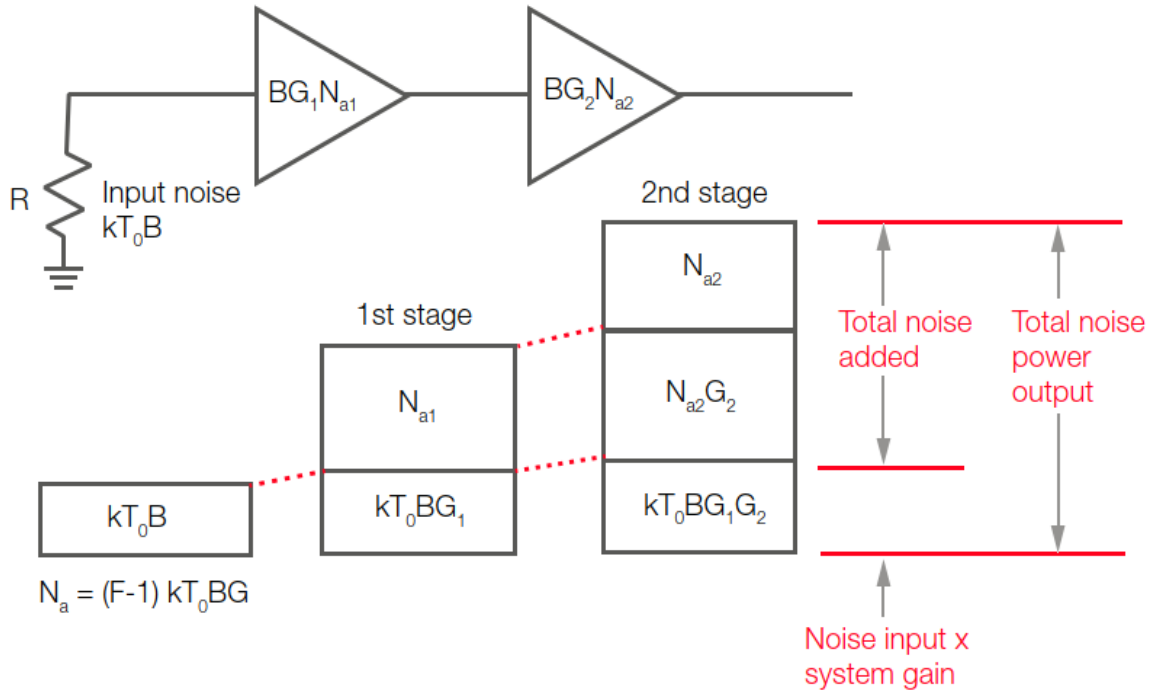


Figure 47: A diagram showing how noise behaves in a system cascade. This is the reality for even trivial use cases, where the first stage represents the DUT and the second stage represents the measurement system. Copied from [61].

$$Y_{12} = \frac{T_s^{on} + T_{12}}{T_s^{off} + T_{12}} \quad (77)$$

and thus the combined stage-1 and stage-2 noise temperature is calculated as

$$T_{12} = \frac{T_s^{on} - Y_{12}T_s^{off}}{Y_{12} - 1} \quad (78)$$

Since the measurement includes the first and the second stage together, the gain of the first stage is not measured in isolation. However it can be calculated from the four measurements thus:

$$G_1 = \frac{N_{12}^{on} - N_{12}^{off}}{N_2^{on} - N_2^{off}} \quad (79)$$

where N_{12}^{on} is the noise power measured of both the first and second stage together with the noise source on, etc. With G_1 calculated one can compute the noise temperature of the DUT:

$$T_{DUT} = T_1 = T_{12} - \frac{T_2}{G_1} \quad (80)$$

These are the formulae for performing a calibration and then calculating the noise and gain of the DUT. Realistically, modern noise measurement systems will guide a user through this process step by step, and will perform all of these calculations automatically. But it is important to understand this technique in order to develop new processes, measure systems with more components (discussed shortly), or measure novel devices that do not fit this mold, e.g. three-port devices.

Figure 47 represents the simplest case for measuring the noise of a device, but there are situations where other devices must also be included in the system cascade, for example a cryostat.

This is a sealed system where the DUT cannot be measured in isolation. Such a system would include other components such as attenuators, filters, couplers, and isolators. There are additional calculations required with having devices before, and devices after the DUT in the system chain. Concerning components before the DUT, one must compute and apply their cumulative loss L_b , which must be a linear ratio, not dB. It will modify T_{12} and G_1 in this manner:

$$T_{12} = \frac{T_{12}^{meas}}{L_b} - \frac{(L_b - 1)T_{Lb}}{L_b} \quad (81)$$

$$G_1 = G_1^{meas} L_b \quad (82)$$

where T_{Lb} is the physical temperature of the lossy components before the DUT. T_{12}^{meas} and G_1^{meas} are the noise temperature and gain, respectively, of the system that was measured, and T_{12} and G_1 are the noise temperature and gain that have been corrected for input losses. After this adjustment one can proceed with (80) as normal unless losses after the DUT must also be accounted for.

Regarding the contribution of losses from components after the DUT which cannot be calibrated out, a similar correction factor must be applied. As with L_b , L_a must be a linear ratio and not logarithmic. It will modify T_2 and G_1 in this manner:

$$T_2 = L_a T_2^{meas} + (L_a - 1)T_{La} \quad (83)$$

$$G_1 = G_1^{meas} L_a \quad (84)$$

where T_{La} is the physical temperature of the lossy components after the DUT. Similar to the previous correction described, T_2^{meas} and G_1^{meas} are the noise temperature and gain, respectively, of the system that was measured, and T_2 and G_1 are the noise temperature and gain that have been corrected for output losses. With both input and output losses, G_1 will need to be scaled in both cases. These corrections are cumulative and commutative. After this adjustment one can proceed with (80) as normal.

Ideally a system will be equipped with switches to be able to measure the system with and without the DUT in the signal chain, and in this fashion one may easily calibrate out the system cascade. But this is not always a reality.

Another detail requiring consideration is the noise power of the noise source (expressed as ENR). Typically a designer should choose the lowest ENR that will satisfy the system requirements [61]. In a cryogenic system an engineer operates in a different temperature regime and will include significant attenuation to bring incoming room-temperature noise levels down to cryogenic levels. Thus when determining which noise source to use in the measurement one must calculate what the noise level will be at the DUT and ensure it is not too far from the expected noise temperature of the device, and that the T_s^{off} and T_s^{on} span is not too narrow, as discussed above. An example of this calculation is found in the section "Noise Measurement" discussing the BlueFors measurement system below.

Measurement System Development

UVA Cryostat

UVA has a small cryostat which is used for many superconducting experiments. I created a new cryostat radiation shield for better cryogenic performance and more reliable connections, as shown in Figure 48. Since the outside walls of the cryostat are directly connected to the ambient temperatures of the room, they will not be able to reach cryogenic temperatures, so it must be properly isolated from the cold stage. This includes shielding from the blackbody radiation emitted from its inside surface. This energy is intercepted by a radiation shield which can be sunk into a higher temperature (and higher power) first cold stage. Prior to this contribution, a simple piece of bent sheet copper was used. After this addition our cryostat's minimum cold temperature was lowered from 5-8K to 3K, and it also increased the surface area of the first stage by approximately 500% which is valuable to attach parts for intermediate heat sinking.

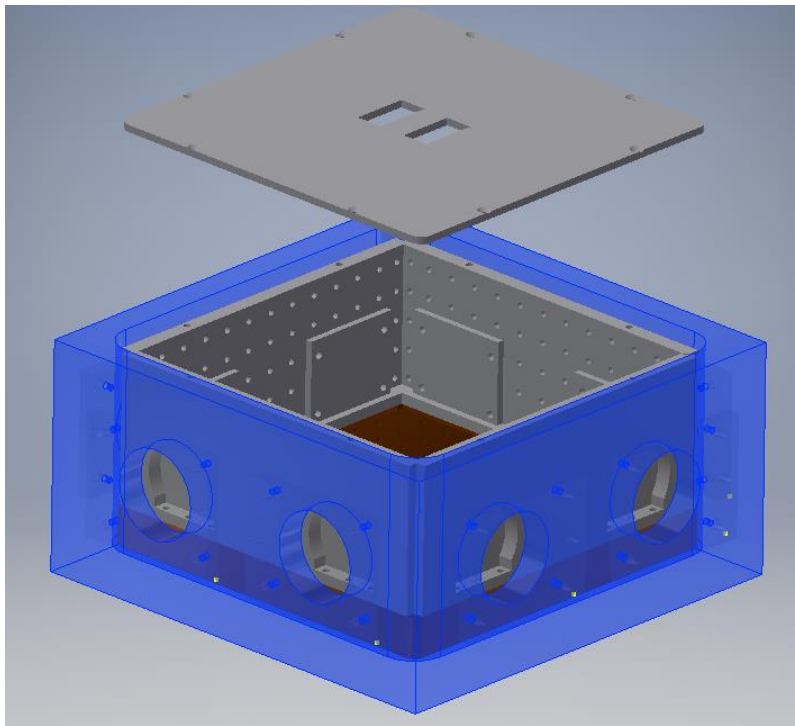


Figure 48: The new cryostat radiation shield, shown in grey. The outer wall of the cryostat is semi-transparent blue.

BlueFors MilliKelvin Dilution Refrigerator

Another task that I have contributed to is the design and implementation of a cryogenic test setup for W-band devices (75-110 GHz). This is a waveguide-based system with the intent of measuring the gain and noise of TKIPs at milliKelvin temperatures ($\sim 100\text{mK}$). The initial plan was prepared by Omid Noroozian, after which I took over the development and implementation. The signal path must connect to fixed vacuum-sealed bulkheads at the top of the cryostat and bolt to the cold stage at the bottom of the cryostat. When using rigid waveguide this means that every micrometer of the system must be planned out, including thermal sinking and even such simple details as how devices will be installed or removed.

The setup is similar to other TKIP test systems documented by other groups. Shown below in Figure 50 is the block diagram of the system when configured to measure noise. To instead measure S-parameters and gain, the noise source and spectrum analyzer would be replaced by two ports of a VNA. The spectrum analyzer could be replaced by another type of power detector if desired, however it is valuable to be able to see the power as a function of frequency.

There is a signal input path where the signal of interest (a VNA or noise source) is combined with the pump signal. In this case the pump was produced by a multiplier/amplifier which converted a 12-18 GHz signal from a common signal generator up to the 75-110 GHz W-band frequencies. The system is designed with several attenuators to reduce the incoming signal with room-temperature noise levels down to cryogenic levels, as discussed in the previous section on noise. At the bottom of the system is the DUT, after which there is a cryogenic LNA used to amplify the output signal back to near room-temperature levels. However, at this point the signal is still accompanied by the strong pump tone used to drive the amplifier, which would saturate the LNA. Therefore before reaching the LNA there is a coupler though which one injects a copy of the pump tone in anti-phase in order to cancel it. A single multiplier could not provide sufficient power to drive the system, so two multipliers were used in parallel—one to drive the TKIP and the other to cancel the signal out on the output side. A variable attenuator and phase shifter are used in order to be able to align the cancellation tone despite variations in the two paths' attenuations and electrical lengths.

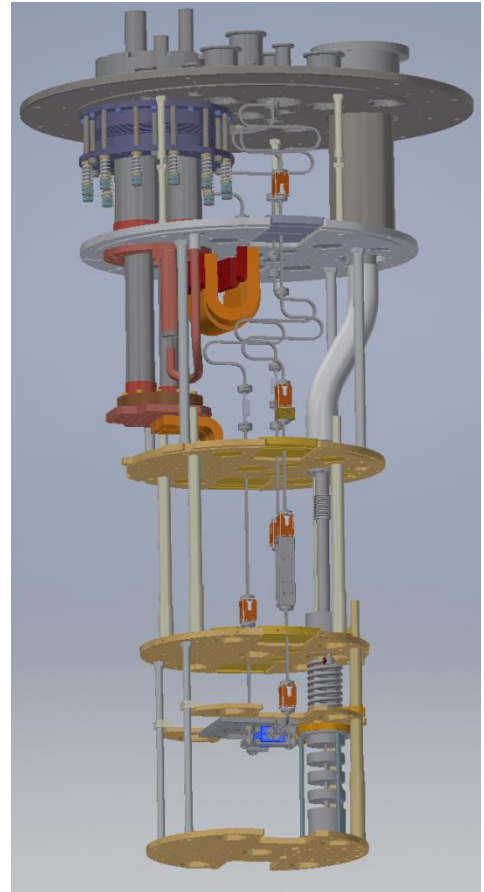


Figure 49 CAD of the mK W-band test setup. The device enclosure is highlighted in blue.

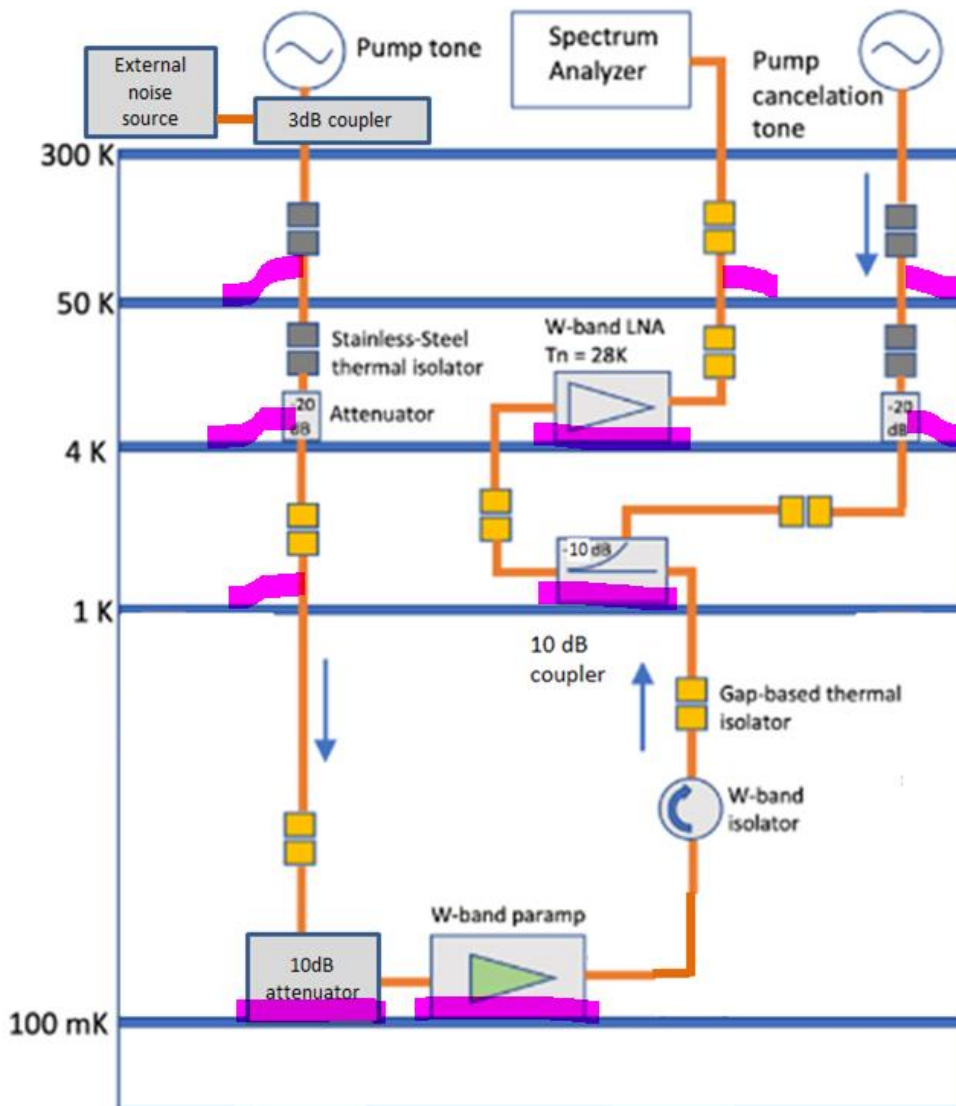


Figure 50: Block diagram of the W-band mK test system configured to measure noise. The pink marks indicate the positions of the thermal sinking, either by bolting to a cold stage or via copper braid.

Thermal Considerations

To address the large thermal load provided by the waveguide conductors two different approaches were taken. In the two input paths, thermal breaks were added between the higher temperature stages in the form of short sections of stainless steel waveguide since its thermal conductivity is much less than that of the coin silver waveguide that was used. After those thermal breaks the waveguide chain would be thermally sunk to the next cold stage using copper braids. This technique is simple, but the stainless steel contributes greater loss to the system, which is undesirable when the signal is weaker. Thus on the output line special thermal breaks were utilized instead. These were manufactured by collaborators at the University of Arizona which have a small airgap between the two sides of the waveguide channel, and are held together by G10 fiberglass laminate. At the interface there is a photonic bandgap structure to reduce signal leakage.

Since a rigid waveguide system's physical dimensions must be precise, and since the dimensions of physical materials shrink somewhat when cooled, large S-bends were added to reduce the stress on connectors as the lines shrink and expand with the temperature changes.

Noise Measurement

The system is designed to enable a measurement of the noise contributed by the DUT via the traditional Y-factor technique. Initially the plan was to use in-situ variable blackbody noise sources, but these were not available when parts were being ordered, so an external noise source was purchased instead. An in-situ noise source would have the advantage of removing the attenuation and noise of all of the system components before the DUT (see discussion in Measuring Noise section above).

The goal is to measure the noise produced by the DUT, and the range of powers T_s^{on} and T_s^{off} of the noise source should not be far from the expected T_{DUT} for good accuracy, as discussed in the aforementioned section. Therefore a cryogenic system designer must calculate what a noise source's power will be at the DUT, after all the input attenuation is accounted for. For example, when designing this system two noise sources were available, one with 12dB ENR and another with 18dB ENR. To determine which is preferred, first one must convert the ENR from a logarithmic ratio to a linear temperature, like so:

$$T_{on} = T_o 10^{\frac{ENR_{dB}}{10}} + T_{off} \quad (85)$$

where $T_o = 290 K$. Assuming that $T_{off} = T_o$, then an ENR of 12dB correlates to $T_{on} = 4886 K$. The BlueFors system has 20dB attenuation at the 4K stage and 10dB attenuation at the 100mK stage. The noise power at each attenuator is

$$T_{out} = \frac{T_{in}}{A_{lin}} + T_{phys} \quad (86)$$

where T_{in} is the noise presented to the attenuator input, A_{lin} is the attenuation of the attenuator in linear scale, and T_{phys} is the physical temperature of the attenuator. Thus with the noise source turned off the output of the 20dB attenuator the noise temperature is $290K/100 + 4K = 6.9K$, and at the output of the 10dB attenuator, $6.9K/10 + 0.1K = 0.79K$. With the 12dB noise source on there is 52.86K at the 4K stage and 5.386K at the 100mK stage. The noise levels at the DUT of $T_{on} = 5.386K$ and $T_{off} = 0.79K$ do not present a wide temperature span for an accurate gain measurement. As mentioned before, a simple rule of thumb is to have an approximate ratio greater than 10. Therefore we now consider the 18dB ENR noise source. Assuming again that $T_{off} = T_o = 290K$, then $T_{on} = 18588K$. At the 4K stage this translates to 189.88K, and at the 100mK stage this yields 19.088K. A range of $T_{on} = 19.088K$ to $T_{off} = 0.79K$ is sufficiently wide, so the 18dB ENR noise source was chosen.

Pictures of the final BlueFors system are below. Most of the objects in the cryostat are for its operation. There is not a lot of space in the cryogenic system (more space and mass means longer cooldown and warmup times), so it appears cluttered.



Figure 51: A picture of the open BlueFors cryostat with the w-band waveguide system installed.

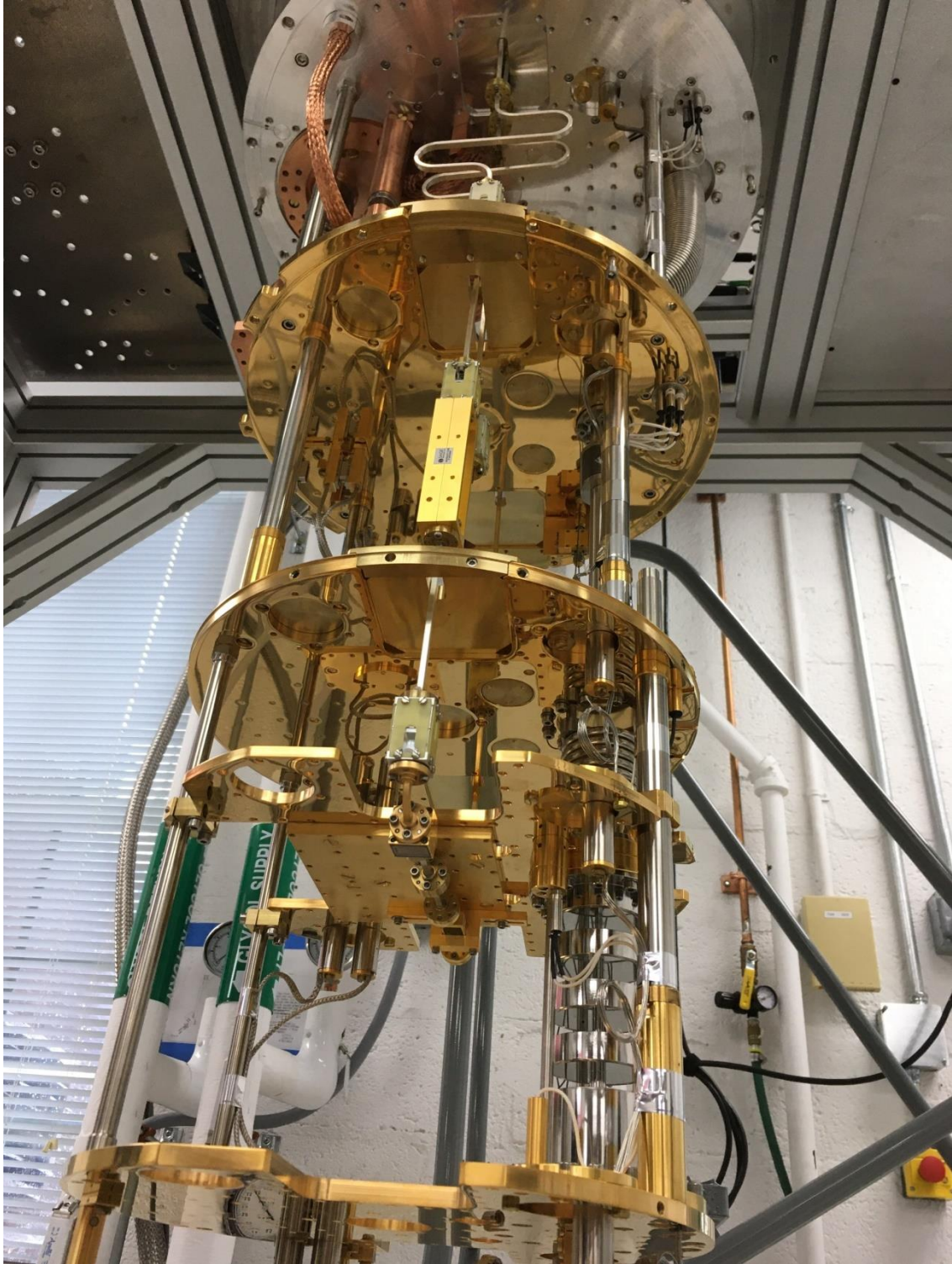


Figure 52: An image of the open BlueFors cryostat from the bottom to show the hardware under the 100mK stage.

Chapter 5: Future work

Good research usually asks more questions than it can answer, and inevitably there are always more doors to open and explore than there is time. The next most interesting steps to continue this research would be:

- Fabricate and measure a device using the final recipe. This was not possible during my tenure as the tool for depositing superconducting films went offline shortly after finalizing the recipe.
- Create a software tool that will calculate coupling parameters (C_s , C_m , L_s , L_m) for an arbitrary number of conductors from physical geometries, such as described in [52].
- Fabricate and measure a structure with periodic coupling to test the matrix extension theory.
- Borrow a known-good w-band TKIP to test in the BlueFors w-band test system.
- Test the T_c , resistivity, and penetration depth of the films with an annealing step in the fabrication recipe. Annealing NbTiN films post-deposition has been shown to increase the T_c and resistivity of the film [39], but the penetration depth of an annealed film has not been measured previously. 250degC is a fair compromise between enough energy to affect a material change while not posing a significant risk of damaging the wafer, e.g. by producing blisters in the bond.
- Take advantage of the microstrip medium and add additional structures on-wafer, such as couplers.
- Test TKIPs in a balanced amplifier setup.
- Create and test a three-wave mixing TKIP.
- Attempt to vary the thickness of the film across the TKIP to modulate its nonlinearity, similar to the work done in [14].

Bibliography

- [1] W. Shan, Y. Sekimoto, and T. Noguchi, "Parametric Amplification in a Superconducting Microstrip Transmission Line," *IEEE Transactions on Applied Superconductivity*, vol. 26, no. 6, pp. 1-9, 2016, doi: 10.1109/TASC.2016.2555914.
- [2] R. P. Erickson and D. P. Pappas, "Theory of multiwave mixing within the superconducting kinetic-inductance traveling-wave amplifier," *Phys. Rev. B*, vol. 95, no. 10, Mar, p. 27, 2017, doi: 10.1103/PhysRevB.95.104506.
- [3] M. R. Vissers *et al.*, "Low-noise kinetic inductance traveling-wave amplifier using three-wave mixing," *Applied Physics Letters*, vol. 108, no. 1, p. 012601, 2016/01/04 2016, doi: 10.1063/1.4937922.
- [4] S. Chaudhuri *et al.*, "Broadband parametric amplifiers based on nonlinear kinetic inductance artificial transmission lines," *Applied Physics Letters*, vol. 110, no. 15, p. 152601, 2017/04/10 2017, doi: 10.1063/1.4980102.
- [5] A. A. Adamyan, S. E. de Graaf, S. E. Kubatkin, and A. V. Danilov, "Superconducting microwave parametric amplifier based on a quasi-fractal slow propagation line," *Journal of Applied Physics*, vol. 119, no. 8, p. 083901, 2016/02/28 2016, doi: 10.1063/1.4942362.
- [6] D. Leisawitz *et al.*, "Far-IR/submillimeter space interferometry: scientific motivation and technology requirements," in *2001 IEEE Aerospace Conference Proceedings (Cat. No.01TH8542)*, 10-17 March 2001 2001, vol. 4, pp. 4/1995-4/2004 vol.4, doi: 10.1109/AERO.2001.931527.
- [7] R. Janssen, "Multiwavelength observations of active galactic nuclei," TU Delft, 2017.
- [8] M. Pospieszalski, A. Kerr, and J. Magnum, "On the Instantaneous SIS Receiver Bandwidth," in *ALMA Memo 601*, ed: National Radio Astronomy Observatory.
- [9] "Low-noise cryogenic HEMT amplifiers." <https://www.lownoisefactory.com/products/> (accessed).
- [10] P. Yagoubov *et al.*, "Wideband 67-116 GHz receiver development for ALMA Band 2," *Astronomy and Astrophysics*, vol. 634, 2019.
- [11] O. Noroozian, "Quantum-Limited Very-Wideband 4-Kelvin RF and IF Amplifiers for ALMA," in *Cycle 5 NRAO ALMA Development Study Proposal – Quantum-Limited Very-Wideband 4-Kelvin RF and IF Amplifiers for ALMA*, ed. 1180 Boxwood Estate Rd., Charlottesville, VA 22903: National Radio Astronomy Observatory, 2017.
- [12] M. Pospieszalski, "Extremely low-noise amplification with cryogenic FETs and HFETs: 1970-2004," *Microwave Magazine, IEEE*, vol. 6, pp. 62-75, 10/01 2005, doi: 10.1109/MMW.2005.1511915.
- [13] C. Bockstiegel *et al.*, "Development of a Broadband NbTiN Traveling Wave Parametric Amplifier for MKID Readout," *Journal of Low Temperature Physics*, vol. 176, no. 3, pp. 476-482, 2014/08/01 2014, doi: 10.1007/s10909-013-1042-z.
- [14] K. Peng, M. Naghiloo, J. Wang, G. D. Cunningham, Y. Ye, and K. P. O'Brien, "Near-Ideal Quantum Efficiency with a Floquet Mode Traveling Wave Parametric Amplifier," *ArXiv*,
- [15] B. Ho Eom, P. K. Day, H. G. LeDuc, and J. Zmuidzinas, "A wideband, low-noise superconducting amplifier with high dynamic range," *Nat Phys*, 10.1038/nphys2356 vol. 8, no. 8, pp. 623-627, 08//print 2012, doi: <http://www.nature.com/nphys/journal/v8/n8/abs/nphys2356.html#supplementary-information>.
- [16] O. Noroozian, "Technology Development of Quantum-Limited, Ultra-Wideband RF Amplifiers for ALMA: A 65-150 GHz Amplifier Test Case," in *Cycle 7 NRAO ALMA Development Study Proposal –*

- [35] S. J. Weber, K. W. Murch, D. H. Slichter, R. Vijay, and I. Siddiqi, "Single crystal silicon capacitors with low microwave loss in the single photon regime," *Applied Physics Letters*, vol. 98, no. 17, p. 172510, 2011, doi: 10.1063/1.3583449.
- [36] E. A. Tholén, A. Ergül, E. M. Doherty, F. M. Weber, F. Grégis, and D. B. Haviland, "Nonlinearities and parametric amplification in superconducting coplanar waveguide resonators," *Applied Physics Letters*, vol. 90, no. 25, p. 253509, 2007/06/18 2007, doi: 10.1063/1.2750520.
- [37] R. Bass *et al.*, "Ultra-Thin Silicon Chips for Submillimeter-Wave Applications," 01/01 2004.
- [38] W. Woods *et al.*, "Determining Interface Dielectric Losses in Superconducting Coplanar-Waveguide Resonators," *Physical Review Applied*, vol. 12, no. 1, p. 014012, 07/08/ 2019, doi: 10.1103/PhysRevApplied.12.014012.
- [39] T. Farrahi, M. E. Cyberek, M. B. Eller, and A. W. Lichtenberger, "Effect of Post Deposition Annealing on the Structural and Electrical Properties of NbTiN Thin Films Deposited by Reactive Bias Target Ion Beam Deposition Technique," *IEEE Transactions on Applied Superconductivity*, vol. 29, no. 5, pp. 1-5, 2019, doi: 10.1109/TASC.2019.2910024.
- [40] D. F. Williams and T. H. Miers, "A coplanar probe to microstrip transition," *IEEE Transactions on Microwave Theory and Techniques*, vol. 36, no. 7, pp. 1219-1223, 1988, doi: 10.1109/22.3659.
- [41] J. Bardeen, L. N. Cooper, and J. R. Schrieffer, "Theory of Superconductivity," *Physical Review*, vol. 108, no. 5, pp. 1175-1204, 12/01/ 1957, doi: 10.1103/PhysRev.108.1175.
- [42] M. Malnou *et al.*, "Three-Wave Mixing Kinetic Inductance Traveling-Wave Amplifier with Near-Quantum-Limited Noise Performance," *PRX Quantum*, vol. 2, no. 1, p. 010302, 01/05/ 2021, doi: 10.1103/PRXQuantum.2.010302.
- [43] K. O. Brien *et al.*, "Towards quantum-noise limited multiplexed microwave readout of qubits," in *2016 IEEE MTT-S International Microwave Symposium (IMS)*, 22-27 May 2016 2016, pp. 1-3, doi: 10.1109/MWSYM.2016.7540350.
- [44] D. M. Pozar, *Microwave Engineering*, 3rd ed. USA: John Wiley & Sons, 2005.
- [45] R. Collier, *Transmission Lines: Equivalent Circuits, Electromagnetic Theory, and Photons* (The Cambridge RF and Microwave Engineering Series). Cambridge: Cambridge University Press, 2013.
- [46] T. R. Arabi, T. K. Sarkar, and A. R. Djordjevic, "TIME AND FREQUENCY DOMAIN CHARACTERIZATION OF MULTICONDUCTOR TRANSMISSION LINES," *Electromagnetics*, vol. 9, no. 1, pp. 85-112, 1989/01/01 1989, doi: 10.1080/02726348908915229.
- [47] J. O. Scanlan, "Theory of microwave coupled-line networks," *Proceedings of the IEEE*, vol. 68, no. 2, pp. 209-231, 1980, doi: 10.1109/PROC.1980.11618.
- [48] S. K. Tolpygo, E. B. Golden, T. J. Weir, and V. Bolkhovsky, "Mutual and Self-Inductance in Planarized Multilayered Superconductor Integrated Circuits: Microstrips, Striplines, Bends, Meanders, Ground Plane Perforations," *IEEE Transactions on Applied Superconductivity*, vol. 32, no. 5, pp. 1-31, 2022, doi: 10.1109/TASC.2022.3162758.
- [49] J. F. Kang, R. Q. Han, G. C. Xiong, X. Y. Liu, and Y. Y. Wang, "Kinetic inductance of coupled superconducting microstrip lines," *Physica C: Superconductivity and its Applications*, vol. 282-287, pp. 2529-2530, 1997/08/01/ 1997, doi: [https://doi.org/10.1016/S0921-4534\(97\)01333-6](https://doi.org/10.1016/S0921-4534(97)01333-6).
- [50] A. R. Kerr, "Surface Impedance of Superconductors and Normal Conductors in EM Simulators," ed: MMA Memo No. 245, 1999.
- [51] W. P. Ou, "Design equations for an interdigitated directional coupler," *IEEE Transactions on Microwave Theory Techniques*, vol. 23, pp. 253-255, 1975, doi: 10.1109/TMTT.1975.1128534.
- [52] L. A. Pipes, "X. Matrix theory of multiconductor transmission lines," *The London, Edinburgh, and Dublin Philosophical Magazine and Journal of Science*, vol. 24, no. 159, pp. 97-113, 1937/07/01 1937, doi: 10.1080/14786443708561894.

- [53] M. B. Bazdar, A. R. Djordjevic, R. F. Harrington, and T. K. Sarkar, "Evaluation of quasi-static matrix parameters for multiconductor transmission lines using Galerkin's method," *IEEE Transactions on Microwave Theory and Techniques*, vol. 42, no. 7, pp. 1223-1228, 1994, doi: 10.1109/22.299760.
- [54] A. I. Grayzel, "A Useful Identity for the Analysis of a Class of Coupled Transmission-Line Structures (Letters)," *IEEE Transactions on Microwave Theory and Techniques*, vol. 22, no. 10, pp. 904-907, 1974, doi: 10.1109/TMTT.1974.1128378.
- [55] G. Mazzarella, "CAD modeling of interdigitated structures," *IEEE Transactions on Education*, vol. 42, no. 1, pp. 81-87, 1999, doi: <https://doi.org/10.1109/13.746340>.
- [56] R. C. Compton, "Perspectives in microwave circuit analysis," in *Proceedings of the 32nd Midwest Symposium on Circuits and Systems*, 14-16 Aug. 1989 1989, pp. 716-718 vol.2, doi: 10.1109/MWSCAS.1989.101955.
- [57] A. a. H. J. a. A. J. a. F. H. a. R. V. a. E. M. a. S. N. a. W. R. a. B. W. a. F. F. Arsenovic, "scikit-rf: An Open Source Python Package for Microwave Network Creation, Analysis, and Calibration Speaker's Corner," *IEEE Microwave Magazine*, vol. 23, no. 1, pp. 98-105, 2022, doi: 10.1109/MMM.2021.3117139.
- [58] M. U. Merino and G. M. Puchalt. "Integrated Capacitive PGAs in ADCs: Redefining Performance." <https://www.analog.com/en/resources/analog-dialogue/articles/integrated-capacitive-pgas-in-adcs.html> (accessed Feb 15, 2024).
- [59] A. R. Kerr and J. Randa, "Thermal Noise and Noise Measurements—A 2010 Update," *IEEE Microwave Magazine*, vol. 11, no. 6, pp. 40-52, 2010, doi: 10.1109/MMM.2010.937732.
- [60] H. B. Callen and T. A. Welton, "Irreversibility and Generalized Noise," *Phys. Rev.*, vol. 83, no. 1, pp. 34-40, July 1951 1951.
- [61] "Noise Figure Measurement Accuracy: The Y-Factor Method," ed: Keysight Technologies, 2021.